博士論文

Reactivity of Criegee intermediates in gas phase and
on gas-liquid interfaces
(気相及び気液界面におけるクリーギー中間体
の反応性)

邱　鈞霆

Contents

Chapter 1 Introduction of Criegee intermediate

1.1 Formation of Criegee intermediates in the troposphere

Criegee intermediates (CIs), carbonyl oxides formed in ozonolysis of alkenes, play key roles in the atmospheric chemistry. The concentration of CI is estimated to be on the order of 1×10^4 cm^{-3} to 1×10^5 cm^{-3},[1] which makes a non-negligible contribution to the oxidizing capacity in the troposphere.

The cycloaddition of ozone to the C=C double bond of an alkene forms a cyclic trioxolane intermediate, and the large exothermicity of this reaction leads to a rapid cleavage of the C−C bond and one O−O bond to form a carbonyl compound and a carbonyl oxide, R_1R_2COO, which is known as a CI as shown in Fig.1-1-1.

CI was named after a German chemist, Rudolph Criegee. Nevertheless, Rudolph Criegee firstly noticed the existence of CI was not in the atmosphere but in the aqueous phase.[2] Subsequently, the mechanism of ozonolysis was concluded in gas phase as well.[3]

About 50% of the CIs formed during the ozonolysis of alkenes decompose into OH radicals and other products on a timescale of 1 ns, while the other 50%, which are known as stabilized CIs (sCIs)[4], are stabilized by collisions with other gaseous molecules and have a longer lifetime. (Fig.1-1-2) The sCIs can still decompose into OH radicals and other products on a much longer timescale, about 1 s, depending on the temperature and their structures.[5]

Self-decomposition of unstable CIs is an important source of OH radical in the troposphere. Nevertheless, it has been hitherto difficult to measure OH radical yields from alkene ozonolysis through CI formation with some experimental methods.

The reported values of rate coefficients for O_3 reacting with terpenes and isoprene, which are massively released from plants, are $10^{-17} \sim 10^{-14}$ cm^3 molecule^{-1} s^{-1} [6]-[8] as listed in Table 1-1-1. Wheeler et al.[9] reported a theoretical calculation for the reaction process in the ozonolysis of ethylene as shown in Fig.A1-1. An energy barrier in the

formation of TS01 form the addition of O_3 to ethylene is calculated to be 5.3 kcal mol^{-1} in this work. It is difficult for O_3 and alkenes couple with each other, which hinders the generation of primary ozonide. As a result, alkenes express inert reactivity toward O_3. Su et al.[10] carried out a theoretical calculation for the self-reaction of CH_2OO. They found that there is no energy barrier for the formation of dimeric CH_2OO and an exceptionally large exothermicity, -92.4 kcal mol^{-1}, in this process (Fig.A1-2). A very fast rate coefficient for $CH_2OO + CH_2OO$ was reported in this work, which is 2×10^{-10} cm^3 molecule^{-1} s^{-1}, and subsequently a modified value, $(8 \pm 4) \times 10^{-11}$ cm^3 molecule^{-1} s^{-1} was provided by Ting et al.[11] In contrast with the loss of CIs due to their self-reactions as well as the reactions with some key species in the atmosphere (such as water vapor and SO_2), which will be discussed in the latter sections, the processes for their formation in the atmosphere are extremely slow, which leads to the concentration of CI is far below the detection limit of any devices.

1.2 Breakthrough in the direct observation of Criegee intermediate

Nevertheless, in 2008, the first experimental detection of a CI in the gas phase was reported by Taatjes et al.[12] The simplest CI, CH_2OO was formed in the chlorine-initiated oxidation of dimethyl sulfoxide $CH_3S(O)CH_3$ by the following reactions:

$$Cl + CH_3S(O)CH_3 \rightarrow HCl + CH_2S(O)CH_3 \tag{R1}$$
$$CH_2S(O)CH_3 + O_2 \rightarrow CH_2OO + CH_3SO \tag{R2}$$
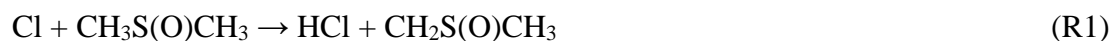
A multiplexed photoionization mass spectrometry (MPIMS) with tunable vacuum ultraviolet synchrotron radiation was applied in the detection of CH_2OO. Asatryan and Bozzelli[13] firstly predicted in their theoretical work that such a formation route facilitates the generation of CH_2OO, because the internal energy is lower compared to ozonolysis. The CH_2OO molecule was identified experimentally, which is also consistent with theoretical predictions.[14] Nevertheless, such a method is not qualified

for the reactivity studies of CH_2OO, due to the signal-to-noise ratio of CH_2OO is insufficient.

Fortunately, In the work of Eskola et al.[15], they reported some other routes for the generation of CH_2OO, which is the photolysis of CH_2I_2 in addition of O_2.

$$CH_2I_2 + hv \rightarrow CH_2I + I \qquad\qquad (R3)$$
$$CH_2I + O_2 \rightarrow CH_2OO + I \qquad\qquad (R4)$$
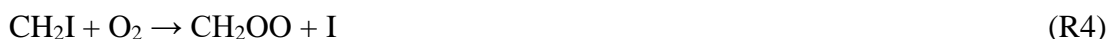
Even though, Eskola et al. did not identify the CH_2OO species, in a subsequent work carried out by Welz et al.[16], they declared the direct observation of the simplest CI, CH_2OO for the first time. MPIMS used in their work offered a mass spectrum at a mass resolution of 1600, and both the $m/z = 46.010$ amu and ionization energy agree well with those of CH_2OO.

1.3 Reactivity of stabilized Criegee intermediates

OH radical, O_3 and nitrate radical (NO_3) had been considered as the main gas-phase oxidants, of which OH is important during the daytime and NO_3 during night time.

OH radical was accepted as the major oxidant of SO_2, and its concentration determines the formation of H_2SO_4 in the atmosphere. Mauldin and his co-workers[4] presented performed their field observations in Finland combined with some theoretic calculations and laboratory experiments. According to their conclusion, there is a discrepancy between the atmospheric concentrations of H_2SO_4 that generated in the reaction of OH with SO_2 and that measured in-situ, which revealed a fact that there existed another oxidant promoting the formation of H_2SO_4 from the oxidation of SO_2, and sCIs might play such a role.

Several subsequent laboratory works[16]–[19] provided the rate coefficients for sCIs reacting with SO_2 were measured to be at least 10^{-11} cm^3 molecule^{-1} s^{-1}, by monitoring the decay of sCIs in addition of SO_2, which is a powerful evidence that sCIs are effective oxidants for SO_2.

Some other key compounds in the atmosphere show considerate reactivity toward sCIs, like NOx, CO, water, water dimer, alcohols, aldehydes and carboxylic acids, which are regarded as CI scavengers as shown in Fig.1-3-1. And the reactions of sCIs with these chemicals may contribute to the formation of secondary organic aerosol (SOA), affecting the atmospheric environment and climate.

The brilliant work carried out by Welz et al.[16] provided a feasible method for the direct observation of CH_2OO, as introduced in Chapter 1.2. Beside the characterization of CH_2OO, the reactivity of CH_2OO can also be tested by adding some other chemicals in the reaction system in the same time, such as SO_2, NO_2, water vapor, and alcohols, aldehydes and carboxylic acids.

The reaction of CI with water vapor is the most important reactions for determining the concentration of CIs in the troposphere. The concentration of water vapor in the lower troposphere was estimated to be 1.3×10^{17} to 8.3×10^{17} molecule cm^{-3} by Huang et al.[20]

The reaction of CI with water monomer starts from the hydrogen bond connection that carbon of the CI attached to the oxygen atom of H_2O and one H atom of H_2O with the terminal oxygen of the CI, based on the calculation results[21], [22]. An H atom is transferred from the water molecule to the CI, with a hydroxyl-hydroperoxide product formed, which has a significant energetic barrier, and limited rate coefficients for reactions of CIs with water. Welz et al.[16] measured an upper limit of the reaction of CH_2OO with water to be 4×10^{-15} cm^3 molecule^{-1} s^{-1}, and a smaller upper limit was given by Stone et al.[19], which is 9×10^{-17} cm^3 molecule^{-1} s^{-1}. Nevertheless, because of the large concentration of water in the troposphere, even with a relatively low rate coefficient, reaction with water may still dominate the atmospheric removal of CIs.

Contrary to water monomer, water dimer $(H_2O)_2$ shows great reactivity toward the simplest CI CH_2OO. Chao et al.[23] monitored the removal of CH_2OO in the presence of high concentrations of water by employing broadband time-resolved ultraviolet spectroscopy. They observed a clear quadratic dependence of the pseudo-first order decay of CH_2OO on relative humidity, and measured a rate coefficient for reaction of CH_2OO with water dimer as $(6.5 \pm 0.8) \times 10^{-12}$ cm^3 molecule^{-1} s^{-1}. Lewis et al.[24] also

applied time-resolved UV absorption in direct observation of CH_2OO, and calculated a value for this reaction to be $(4.0 \pm 1.2) \times 10^{-12}$ cm^3 molecule^{-1} s^{-1}. Even though these dimers make up a small percentage (<1%) of water vapor, which is in the range of 3.5×10^{13} to 1.4×10^{15} molecule cm^{-3} at 298 K,[20] the rapid reaction of CH_2OO with water dimer, which is about 10^5 times faster than CH_2OO reacting with water monomer, implies that reaction with $(H_2O)_2$ dominates removal of the smallest CI, and possibly other CIs, in the troposphere.

Some other studies also discussed the reactivity of larger CIs toward water or water dimer, and revealed that the rate coefficients for the reaction of CIs + water have a large dependence on the conformation of CIs. Anti-CIs are thought to react up to 5 orders of magnitude faster than syn-CIs. For anti-CH_3CHOO, the rate coefficient for reaction with water is about $1.0 \sim 2.4 \times 10^{-14}$ cm^3 molecule^{-1} s^{-1}[25], [26], and $(4.4 \pm 0.3) \times 10^{-11}$ cm^3 molecule^{-1} s^{-1} with water dimer reported in the work of Lin et al.[27]. For syn-CH_3CHOO, its reaction rate with water is too slow to be measured precisely in an experiment. Instead, the rate coefficients for syn-CH_3CHOO + water and water dimer were determined in a cohort of theory studies, which are $10^{-20} \sim 10^{-18}$ cm^3 molecule^{-1} s^{-1} and $10^{-15} \sim 10^{-14}$ cm^3 molecule^{-1} s^{-1}.[22], [27]–[31]

The experimental results and theory calculation in determining the rate coefficients for next larger CI, $(CH_3)_2COO$, with both water monomer and water dimer, did not match well. The rate coefficient for $(CH_3)_2COO$ reacting with water monomer was predicted to be $10^{-17} \sim 10^{-19}$ cm^3 molecule^{-1} s^{-1}[22], [28], [29], but measured to be $(2.1 \pm 0.6) \times 10^{-15}$ and 1.6×10^{-16} cm^3 molecule^{-1} s^{-1} in these two experimental works.[20], [32] For $(CH_3)_2COO$ reacting with water dimer, Ryzhkov and Ariya[22] provided a rate coefficient, $(6.5 - 10.2) \times 10^{-17}$ cm^3 molecule^{-1} s^{-1}. Otherwise, a much larger value was reported by Huang et al.[20], that is 1.3×10^{-13} cm^3 molecule^{-1} s^{-1}.

In a series of works, the reactivity of CI toward aldehyde was studied by adding aldehyde to gas-phase ozonolysis of some alkenes. The rate coefficient for reaction of CH_3CHOO with acetaldehyde to be 1×10^{-12} cm^3 molecule^{-1} s^{-1}.[33] Later in another work by Horie et al., hexafluoroacetone was found reacting 13 times more rapidly with CH_2OO than does acetaldehyde.[34]

The group of Taatjes et al., which firstly introduced the photolysis of CH_2I_2/O_2 method into the generation of the simplest CI, CH_2OO, measured the the rate coefficient for reaction of CH_2OO with hexafluoroacetone at 4 Torr directly, which is $(3.0 \pm 0.3) \times 10^{-11}$ cm^3 $molecule^{-1}$ s^{-1}[35]. Liu et al.[36] carried out a following work for the same reaction at 50 Torr, and provided an almost same value, $(3.33 \pm 0.27) \times 10^{-11}$ cm^3 $molecule^{-1}$ s^{-1}. Taatjes et al.[35] also measured rate coefficients for CH_2OO reacting with acetaldehyde, $(9.5 \pm 0.7) \times 10^{-13}$ cm^3 $molecule^{-1}$ s^{-1}, and acetone, $(2.3 \pm 0.3) \times 10^{-13}$ cm^3 $molecule^{-1}$ s^{-1}, which are significantly lower than that with hexafluoroacetone.

The process of CI reacting with ROOH, which is similar to the reaction of CI with water monomer, is just like the insertion of CI into ROO—H bond. The H atom of ROOH transferred to the terminal O of CI and the ROO part attached to the C atom. Welz et al.[37] measured rate coefficients for both CH_2OO and CH_3CHOO with acetic acid and formic acid, by monitoring the concentration of CIs directly. All the rate coefficients determined in their work are in excess of 10^{-10} cm^3 $molecule^{-1}$ s^{-1}. Compared to an O—H bond in a H_2O molecule, the O—H bond of ROOH is much more fragile and dissociate an H which transfers to the terminal O of CI facilely. The large rate coefficients for reactions of CIs with organic acids may make these reactions significant contributors to removal of organic acid in the troposphere.

1.4 Multiphase Criegee chemistry

The reactions of CIs with water vapor, or their self-decomposition determine the fate of CI in the troposphere. Some simple CI species have been hitherto synthesized and observed directly by using the photolysis of diiodoalkanes. Nevertheless, it is just a little step in understanding the Criegee chemistry. Large quantities of unsaturated organic compounds are released from vegetation, and much more complex CIs can be formed in the ozonolysis of these compounds.

In the real atmosphere, unsaturated organic compounds can condense or be absorbed by some oil-water mixed droplets to form the organic-water mixed aerosols, which are

ideal places for the multiphase Criegee reactions taking place. Surface-absorbed O_3 forms relatively strong binding to the liquid surface, and ozonation reactions proceed, which is known as Langmuir−Hinshelwood mechanism. Formation of CI upon ozonolysis of unsaturated organic compounds on gas-liquid interfaces may subsequently trigger a series of oxidation reactions, which may finally affect the atmospheric environment and human health.

Zhong et al.[38]–[40] carried out a series of theoretical calculations of the reactivity of CI on gas-liquid surface by using Born−Oppenheimer molecular dynamics simulations. In these studies, the simplest CI, CH_2OO exhibits high reactivity toward the interfacial water and hydrogen sulfide, with the reaction times being a few picoseconds, 2−3 orders of magnitude faster than that in the gas phase.

Heine et al.[41] examined heterogeneous ozonolysis of squalene, which is one of the most abundant unsaturated constituents of the human sebum. The heterogeneous reaction of ozone with squalene was carried out in an aerosol flow tube reactor, and the products were analyzed by an electrostatic classifier coupled with a butanol condensation particle counter and a vacuum ultraviolet aerosol mass spectrometer. The experimental results are supported by a kinetic modeling study, and they found that the decomposition of the primary ozonide predominantly leads to the formation of CI, which furthermore form ketones or isomerize to α-hydroxy ketones. In a following study performed by the same group[42], multiphase reaction of SO_2 with CI was discussed at different relative humidity. The oxidation of SO_2 via Criegee chemistry was found capable of competing with water vapor due to its high reactivity toward CI, contributing to an enhanced chemical erosion of the squalene aerosol, as well the formation of sulfuric acid.

Multiphase ozonolysis of unsaturated organic compounds as well as subsequent CI involved reactions have been explored in cohort studies, in which flow tube reactors were selected for these reactions taking place. Nevertheless, a molecular level reaction mechanism of interfacial ozonolysis is not fully understood, because the liquid density drops dramatically within ~ 1nm on gas-liquid interfaces, accompanied by depth-dependent ion/molecule enrichment. Enami et al.[43] reported Criegee chemistry

on gas-liquid interfaces by using a pneumatic electrospray ionization mass spectrometer, and the products in molecular-level-depth layers were detected, which will be introduced specifically in Chapter 4.

Limited approaches have been hitherto applied in exploring multiphase Criegee chemistry. The cross linking among gas phase, bulk, as well as interfacial ozonolysis mechanism and CI involved reactions remains a challenge issue to comprehend the multiphase chemistry occurring in the atmosphere.

1.5 Objectives of this study

The research purpose of this study is focused on the reactivity of CI both in gas phase and on gas-liquid interfaces. In real atmospheric circumstances, the formation of CI happens in both situations. A new spectroscopic method was introduced by combining a photolysis system of CH_2I_2/O_2 with a continuous wave quantum cascade laser in exploring the characteristics of the simplest CI, CH_2OO, which haven't been applied in the detection of CH_2OO in gas phase. This new is also available in the kinetics researches on the reactions of CH_2OO with SO_2 and NO_2.

Larger CIs (sesquiterpenes, monoterpenes initiated) generated on gas-liquid interfaces have been detected by employing a pneumatic electrospray ionization mass spectrometer. The reactivity of CI toward benzoic acid, which is abundant in the particle matter found in polluted area, as well as, the reactivity of CIs initiated from monoterpenes species with same molecular weight but different conformers have been investigated.

Based on the experimental results, some implications will be discussed, including the extending application of the quantum cascade laser in the detection of some other CIs, as well as the potential effect of Criegee chemistry on atmospheric environment and human health.

1.6 Structure of this thesis

   This thesis consists of five chapters. Chapter 1 provides an introduction of CI, objectives, layout of this work, and reviewed some previous studies of CI. In Chapter 2, some recent infrared absorption spectroscopic studies of CI are introduced and a new spectroscopic method by using a continuous-wave quantum cascade laser as a light source in recording the spectra of CH_2OO is described. Chapter 3 shows some kinetics researches on CIs in gas phase, including the experimental results acquired in this work. Chapter 4 gives a detailed explanation on the method of detecting CI on gas-liquid interfaces, and reactivity of CIs generated on gas-liquid interfaces is discussed in this chapter. Chapter 5 draws some conclusions of this thesis and future works for Criegee chemistry.
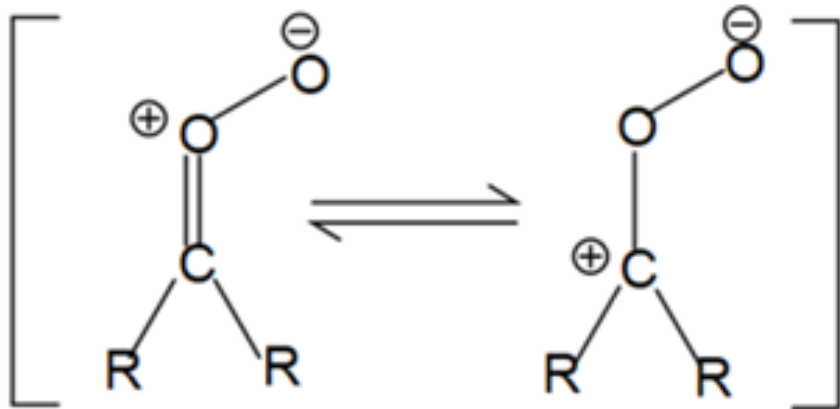
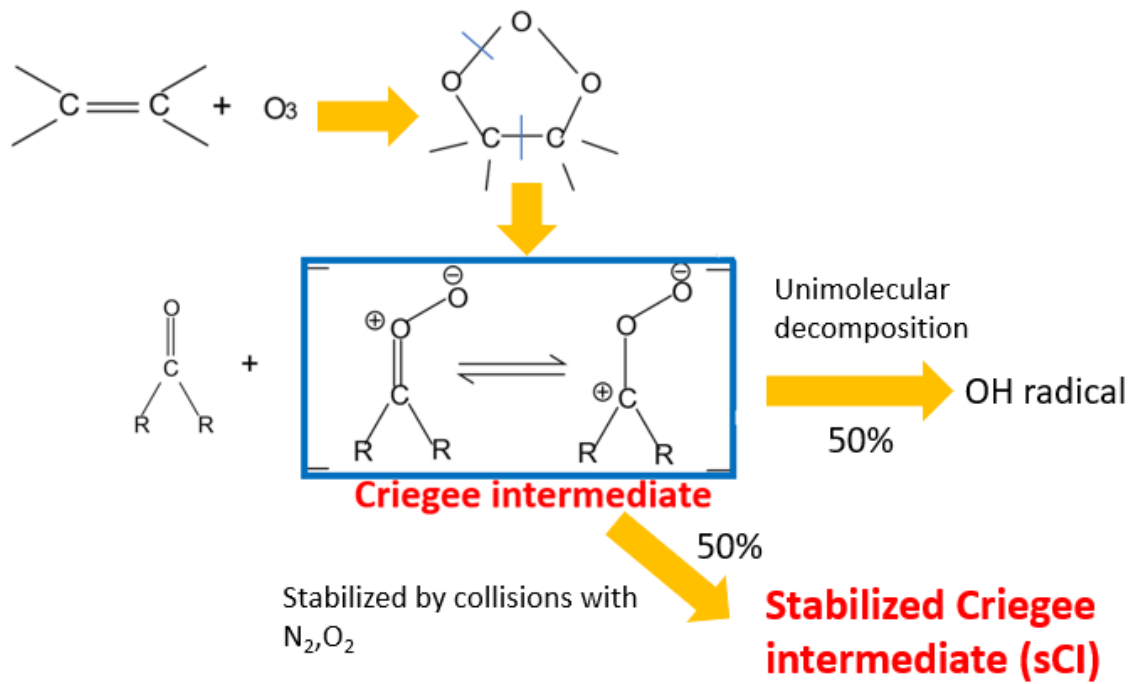Fig.1-1-1 Molecular structure of Criegee intermediate.

Fig.1-1-2 Formation of Criegee intermediate from the reaction of alkene with ozone.
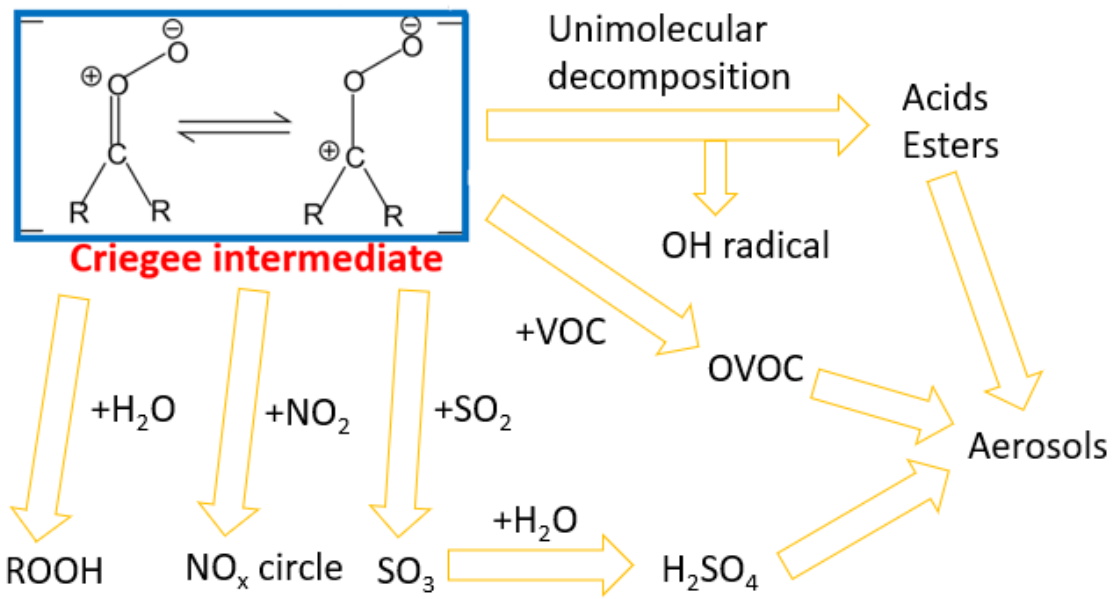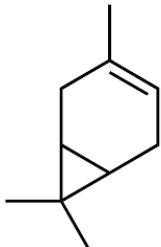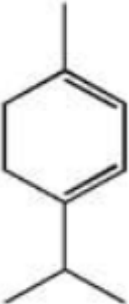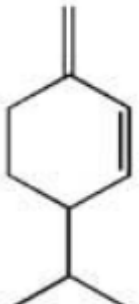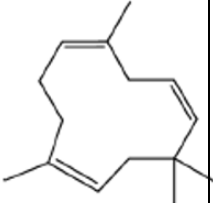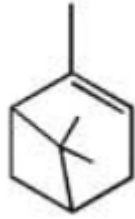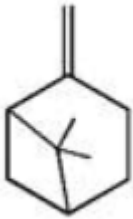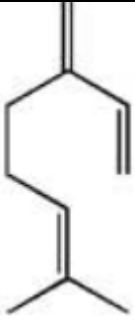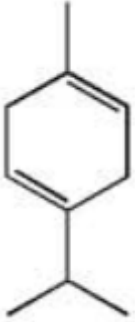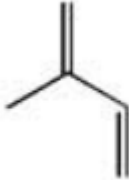
Fig.1-3-1 Reactivity of Criegee intermediate in the troposphere.

Table 1-1-1 Some organic compounds released from plants and their reaction rates (k) toward ozone.[6]-[8]

Compounds	Molecular structure	Formula	Molecular weight	k(ozone)/ cm^3 molecule^{-1} s^{-1}
3-carene		$C_{10}H_{16}$	136	3.7×10^{-17}
α-terpene		$C_{10}H_{16}$	136	2.1×10^{-14}
β-caryophyllene		$C_{15}H_{24}$	204	1.2×10^{-14}
α-humulene		$C_{15}H_{24}$	204	1.2×10^{-14}

α-pinene		$C_{10}H_{16}$	136	8.4×10^{-17}
Terpinolene		$C_{10}H_{16}$	136	1.9×10^{-15}
β-pinene		$C_{10}H_{16}$	136	1.5×10^{-17}
Myrcene		$C_{10}H_{16}$	136	4.7×10^{-16}
γ-terpene		$C_{10}H_{16}$	136	1×10^{-16}

D-limonene		$C_{10}H_{16}$	136	2.1×10^{-16}
Isoprene		C_5H_8	68	1×10^{-17}

Chapter 2 Infrared absorption spectroscopy of Criegee intermediate

2.1 Introduction

Absorption spectroscopy is an important method for the characterization of some free radicals including CI. Absorption spectroscopic researches on CI have been discussed in cohort studies, except for applying a continuous wave quantum cascade laser in the detection of CI, which has high wavelength and time resolution. Based on previous studies, this new method will be in this Chapter.

Absorption spectroscopy refers to techniques that measure the absorption of radiation, which is a useful tool to identify and study chemicals. Different kinds of chemicals choose to absorb light of different wavelengths. The intensity of their absorption varies as a function of frequency or wavelength, and this variation is called absorption spectrum.

Infrared (IR) absorption spectroscopy is the absorption spectroscopy that deals with the infrared region, which covers the range of the electromagnetic spectrum between 0.8 and 1000 μm. Generally, units of frequency used in IR spectra are wavenumbers, the reciprocal of wavelength, with the symbol cm^{-1}.

Furthermore, the infrared region of the electromagnetic spectrum could be divided into three regions; the near-infrared, mid-infrared and far-infrared, according to their relation to visible spectrum. The near-IR, approximately 14000–4000 cm^{-1} (0.8–2.5 μm, wavelength), which has relatively higher energy, can excite overtone or harmonic vibrations. The mid-infrared, approximately 4000–400 cm^{-1} (2.5–25 μm), may be used to study the fundamental vibrations and associated rotational-vibrational structure. The far-infrared, approximately 400–10 cm^{-1} (25–1000 μm), has low energy and may be used for rotational spectroscopy.

In this part, some infrared absorption spectroscopic researches will be introduced, including the detection of the simplest CI, CH_2OO, by using a high-resolution infrared absorption spectroscopic method carried out in our laboratory.

The first gas phase experimental infrared spectrum of a carbonyl oxide was reported

by Su et al.[44] using time-resolved Fourier transform infrared absorption spectroscopy from 800 to 1500 cm^{-1}, at a resolution of 1 cm^{-1}. CH$_2$OO was produced by using well-established (R3) and (R4) processes at 340 K and pressure of 94 Torr in a multi-pass flow cell. In this work, they distinguished the simplest CI, CH$_2$OO from its possible isomers by comparing their absorption spectra contours as listed in Fig.A2-1, and supported the conclusions of the previous study carried out by Welz et al.[16] They also characterized other transient species formed upon photolysis of a flowing mixture of CH$_2$I$_2$ in N$_2$/O$_2$ through the comparison of simulated, using theoretically predicted data, and recorded spectra. The authors assigned five vibrational absorption bands to CH$_2$OO. One *c*-type band was observed at 848 cm^{-1}, and assigned to the CH$_2$ wagging mode of A″ symmetry. The remaining four bands are *a*/*b*-type bands of A′ symmetry at 908 cm^{-1} (O–O stretch), 1241 cm^{-1} (CH$_2$ rock), 1286 cm^{-1} (CO stretch/CH$_2$ scissors), and 1435 cm^{-1} (CH$_2$ scissors/CO stretch).

Subsequently, in another study from the same group, Huang et al.[45] recorded a new absorption spectrum of CH$_2$OO at a better resolution of 0.25 cm^{-1}. The detection of CH$_2$OO with a FTIR spectrometer requires a relatively high concentration of CH$_2$OO. To reach such concentration, the temperature was set to 343 K in the two aforementioned experiments. The enhanced vapor pressure of CH$_2$I$_2$ at 343 K leads to a higher concentration of CH$_2$I$_2$ while being bubbled into the reaction system, therefore a higher concentration of CH$_2$OO can be achieved. However, as these experimental conditions do not mimic those in the atmosphere, FTIR spectroscopy is inappropriate to study CH$_2$OO reactions and measure the corresponding rate coefficients.

More recently, Chang et al.[46] employed a transient absorption spectrometer with a pulsed quantum cascade laser in the detection of CH$_2$OO. In their study, the absorption spectrum of CH$_2$OO at a better resolution of < 0.004 cm^{-1} was recorded. The temperature in this experiment was kept at 298 K, and detailed absorption features and intense absorption lines were observed, which shows the appropriateness of the quantum cascade laser (QCL) used in that kinetic study of CH$_2$OO. The time profile of CH$_2$OO was obtained from the difference absorption spectra of CH$_2$OO by repeatedly scanning through the Q branch in the ν_4 absorption band around 1285.9 cm^{-1}.

2.2 Generation and detection of CH_2OO using a continuous wave quantum cascade laser coupled with laser flash photolysis technique.

The mid-infrared absorption spectra of the ν_4 band of CH_2OO were measured using laser flash photolysis/cw direct absorption spectroscopy. The experimental setup used in this study combines a pulse photolysis system with a mid-infrared absorption spectrometer, which is arranged from the original one reported in the work of Miyano et al.[47], as presented in Fig.2-2-1.

At a room temperature, CH_2I_2 is in liquid phase, which is contained inside a tube used for bubbling. By passing O_2 gas throughout the liquid-phase CH_2I_2, a mixture of CH_2I_2/O_2 in gas phase can be obtained. The ratio of CH_2I_2/O_2 is roughly estimated based on $N_1/N_2 = P_1/P_2$, where N_1 and N_2 are the amounts of CH_2I_2 and O_2, P_1 is the saturated vapor pressure of CH_2I_2, which is about 1.2 torr at 25 °C, and P_2 is the pressure of O_2 gas derived from the oxygen gas cylinder.

Before the mixture of CH_2I_2/O_2 is injected into a reaction cell, it is merged with N_2 gas, in order to dilute the reactants. This reaction cell is a Pyrex cell with 21 mm inner diameter and 90 cm length. As shown in Fig.2-2-2, perforated quartz windows were held on each side of the cell. Because the probe laser beam cannot penetrate the quartz windows, anti-reflection (AR) coated ZnSe windows of a diameter of 1/2 inch were placed on the perforated quartz windows to pass the probe beam. The probe beam was focused in the center of the cell by an AR coated ZnSe lens with a focal length of 415 mm. Two N_2 gas flows, which are parallel to the quartz windows, are used to protect the windows from erosion by reactants.

Gas flows were regulated by calibrated mass flow controllers (Kofloc 3660 and 3550). The total pressure was monitored by a capacitance manometer (MKS, Baratron). The gases used in this experiment were obtained from Nippon Sanso ($O_2 > 99.99995\%$; $N_2 > 99.99995\%$), and diiodomethane is made by Wako (CH_2I_2, > 95%).

The mixed $CH_2I_2/O_2/N_2$ gases are pumped throughout the reaction cell, while CH_2I_2 is decomposed into CH_2I and I radicals by employing a Nd:YAG laser (Continuum

Surelite III). The strong power supply of the Nd:YAG laser generate laser beams of 1064 nm, and those high-intensity laser beams may be efficiently frequency doubled to generate laser light at 532 nm, or higher harmonics at 355 and 266, by using some optical crystals. CH_2I_2 was photolyzed with the fourth harmonics of a Nd:YAG laser at 266 nm in this study. The photolysis laser beam was expanded to a beam diameter of 10 mm through a beam expander. The photolysis pulse energy was ~35 mJ pulse^{-1} cm^{-2}.

After the decomposition of CH_2I_2 into CH_2I and I radicals, CH_2I radical readily react with O_2 intermediately, with the production of CH_2OO which can be detected by mid-infrared probe beams at around 1274 cm^{-1} provided by a continuous wave thermoelectrically-cooled distributed feedback quantum cascade laser (QCL, LC0069, Hamamatsu Photonics K.K., Hamamatsu, Japan). The center laser wavelength can be selected by changing the device temperature with a Peltier driver (C10638-01, Hamamatsu Photonics K.K.). A laser driver (ILX, 3232) was used to operate the QCL. The laser provides a maximum output power of approximately 30 mW. A schematic representation of the QCL is shown in Fig.2-2-3. The QCL was driven in the conditions of device temperatures 30, 40, 50 °C, as well as the electronic current operated from 400 mA to 650 mA. N_2O gas was selected in the wavenumber-current calibration experiment. The details were presented in Table A2-1.

The alignment of the optics is aided by a He-Ne laser beam at 632.8 nm introduced with a beam combiner, which is coaxial with the QCL beam, with the support of an IR imaging camera (Electrophysics Corporation, model: PV320-L2Z). The beams of QCL and YAG laser cross in an angle of 1.5°, therefore, the length of the overlap region between the photolysis and the probe beams was 40 cm.

An off-axis parabolic mirror (25.4 mm diameter, 50.7 mm focal length) was used to collect the probe beam exiting the cell, which was focused through an interference filter (center wavelength 7730 nm, FWHM 250 nm) on a liquid nitrogen cooled HgCdTe detector (Kolmar Technologies, KLD-1-J1/DC/11). The detected photocurrent signal was averaged with a digital oscilloscope (Tektronix, TDS 520C) and transferred to a personal computer by a general-purpose interface bus (USB-GPIB, National Instruments).

The number of the laser pulse for the Nd:YAG laser can be varied from 1 to 10 per second. The oscilloscope is triggered along with the pulsed beam passing though the reaction cell, which represents a start signal for the photolysis of CH_2I_2 and subsequent reactions. The time gap between two adjacent photolysis laser shots must be controlled no less than the retention time of the gas flow. A specialized description of the photolysis/detection mechanism is presented in Fig.2-2-4. For each time the Nd:YAG laser flashes, the absorption intensity of CH_2OO is recorded once. After this process repeated 20 times, the QCL is commanded to emit laser beams of different wavelengths automatically, which means each plot in an absorption spectrum of CH_2OO was an averaged value after 20 times measurements.

The infrared absorption spectrum of CH_2OO in the ν_4 band with a band origin of 1285.9 cm^{-1} is recorded once completely in this experiment after the QCL finished the scanning from 1273.0 to 1277.5 cm^{-1}. The result presented in Fig.2-2-5(a) is an averaged one of 5 complete absorption spectra of CH_2OO recorded in the same region at a resolution of <0.01 cm^{-1}. The experimental result is in contrast with a simulated spectrum in Fig.2-2-5(b), which will be discussed in the following part.

2.3 Simulation of a ν_4 CH_2OO absorption spectum by using Pgopher

Pgopher[48] is a widely used program developed by the Bristol laser group for the simulation of rotational, vibrational and electronic spectra of molecules. In the past decades, the version of Pgopher has been improved multiple times. Linear molecules, as well as symmetric and asymmetric tops, can be the targets of Pgopher. Pgopher is qualified in handling a series of transitions including Raman, multiphoton and forbidden transitions. In this work, the Pgopher program has been applied in the simulation of a mid-infrared absorption spectrum with the consideration of rotational constants as well as the centrifugal distortion constants.

The rotational energy for a molecule is quantized, which can take only fixed values. For any molecule, in the absence of electric and magnetic fields, and without the

consideration of centrifugal distortion its rotational energy levels can be described with rotational constants A, B, and C, and other quantum numbers. Rotational constants A, B, and C are conventionally written as

$$A = \frac{h}{8\pi^2 c I_A} \qquad B = \frac{h}{8\pi^2 c I_B} \qquad C = \frac{h}{8\pi^2 c I_C} \tag{E1}$$

where h is the Planck constant, c is the velocity of light, the three orthogonal moments of inertia: I_A, I_B, and I_C are

$$I_A = \sum_{i=1}^{n} M_A d_{Ai}^2 \qquad I_B = \sum_{i=1}^{n} M_B d_{Bi}^2 \qquad I_C = \sum_{i=1}^{n} M_C d_{Ci}^2 \tag{E2}$$

where M_i is the mass of atom i, whose distance from axes A, B, and C are d_{Ai}, d_{Bi}, and d_{Ci}, respectively.

As mentioned in Chapter 2.1, Chang et al.[46] has recently recorded a high-resolution absorption spectrum of CH_2OO from 1273 to 1290 cm^{-1} using a pulsed QCL and provided modified values for the rotational constants A', B', and C' at the excited state $\nu_4 = 1$. Also, the rotational constants A'', B'', and C'' at the ground state ($\nu = 0$) have been studied by Nakajima and Endo[49], McCarthy et al.[50], and Daly et al.[51] using microwave spectroscopy.

A series of pairs of energy levels were determined by rotational constants A, B, and C at both ground state and excited state, and absorption lines appear at the places where transitions took place. Each line is infinitely sharp, and simply represents a transition between a pair of energy levels. Actually, all transitions are spread over a finite range of wavenumber with a maximum intensity at line center, and obviously distinct from an absorption spectrum is not able to be taken in experiments. Therefore, absorption linewidth and its associated shape must be taken into consideration. Broadening caused by two mechanisms, the random thermal motion of absorption molecules relative to the

analyzing and receiving device, and collisions between molecules, affect absorption lineshape mostly, which are described by Gaussian (Doppler) profile and Lorentz profile.

The Gaussian distribution half-width is related to the molecular weight M and temperature T (K).

$$\gamma_D = 3.581 \times 10^{-7} \nu_0 \sqrt{\frac{T}{M}} \tag{E3}$$

Here, $T = 298$ K, $M = 46$, so $\gamma_D = 0.0017$ cm^{-1}. And the Lorentz distribution halfwidth γ_L = 0.01 cm^{-1}, determined based on our experimental conditions.

Considering the weight of CH_2OO molecule is relatively small, centrifugal distortion may cause a change in the structure of a CH_2OO molecule, and furthermore in its absorption line shapes.

CH_2OO is an asymmetric molecule, and the rotation Hamiltonian for an asymmetric top ($I_A < I_B < I_C$) without considering the reduction of the molecule, can be written as

$$H = \frac{\hat{J}_A^2}{2I_A} + \frac{\hat{J}_B^2}{2I_B} + \frac{\hat{J}_C^2}{2I_C} \tag{E4}$$

If molecular reduction is taken into consideration, the rotation Hamiltonian for an asymmetric top ($I_A < I_B < I_C$) is given by Watson[52]

$$H = H_2 + H_4 + H_6 + H_8 \tag{E5}$$

H_2 is the rigid part independent of molecular deduction, and H_4 is

$$H_4 = - \Delta_J \hat{J}^4 \; - \; \Delta_{JK} \hat{J}^2 \hat{J}_A^2 \; - \; \Delta_K \hat{J}_A^4 \; + (\hat{J}_B^2 \; - \; \hat{J}_C^2)(- \delta_J \hat{J}^2 \; - \; \delta_K \hat{J}_A^2)$$

$$+ (- \delta_J \hat{J}^2 \; - \; \delta_K \hat{J}_A^2) (\hat{J}_B^2 \; - \; \hat{J}_C^2) \cdot$$

(E6)

where, the quartic distortion constants Δ_J, Δ_{JK}, Δ_{JK}, δ_J and δ_K are combinations of A, B, C and other factors. H_6 and H_8 are far more complex than H_4, and since their effects on the absorption line shape of a spectrum are trivial, they will not be discussed here. In the work of Chang et al.[46], they also provided precise values for centrifugal distortion constants for CH_2OO, and all the parameters necessary to carry out a simulation by applying the Pgopher program are listed in Table 2-3-1.

As a result, simulated absorption spectrum of CH_2OO from 1265 to 1300 cm^{-1} is presented in Fig.2-3-1, and the region circled by red dots is the wavenumber our QCL covered.

2.4 Comparison of experimental result and simulation

Absorption lines which are supposed to be the same ones in both Fig.2-2-5(a) and Fig. 2-2-5(b) are listed in the Table 2-4-1. The wavenumber difference for absorption line positions in (a) and (b) is less than 0.053 cm^{-1}, which means that the absorption spectrum of CH_2OO recorded in this work (a) is in good agreement with the simulated one (b). Because the length of the overlap region between the photolysis and the probe beams is only 40 cm in this study, CH_2I_2 was kept at a high concentration in order to guarantee sufficient CH_2OO ($\sim 10^{14}$ molecule cm^{-3}) in recording the absorption spectrum of CH_2OO. Non-zero base signals show up in this absorption spectrum, which might be caused by the absorption of some byproducts generated from the photolysis of CH_2I_2 and subsequent reactions. The kinetics experiments of CH_2OO were performed at relatively lower concentrations of CH_2I_2, when the disturbances of byproducts had been reduced to a large extent. The time profiles of CH_2OO are gained by subtracting the base signals from the raw ones in the kinetics experiments.

A new absorption spectroscopic method by using a thermoelectrically cooled continuous wave mid-infrared distributed feedback QCL in detection of the simplest CI, CH_2OO, is introduced in this Chapter. The recorded absorption spectrum is in good agreement with the simulation result by using Pgopher, in which absorption peaks appear at almost same places. The QCL shows its advantage in high wavelength resolution detection. Separated and intense absorption peaks of CH_2OO are obtained in this experiment, which demonstrates the possibility that this QCL can be applied in monitoring the temporal change of CH_2OO explicitly. The analysis of time profiles of CH_2OO is connected to some kinetics characteristics of CH_2OO which will be discussed in the following chapter.
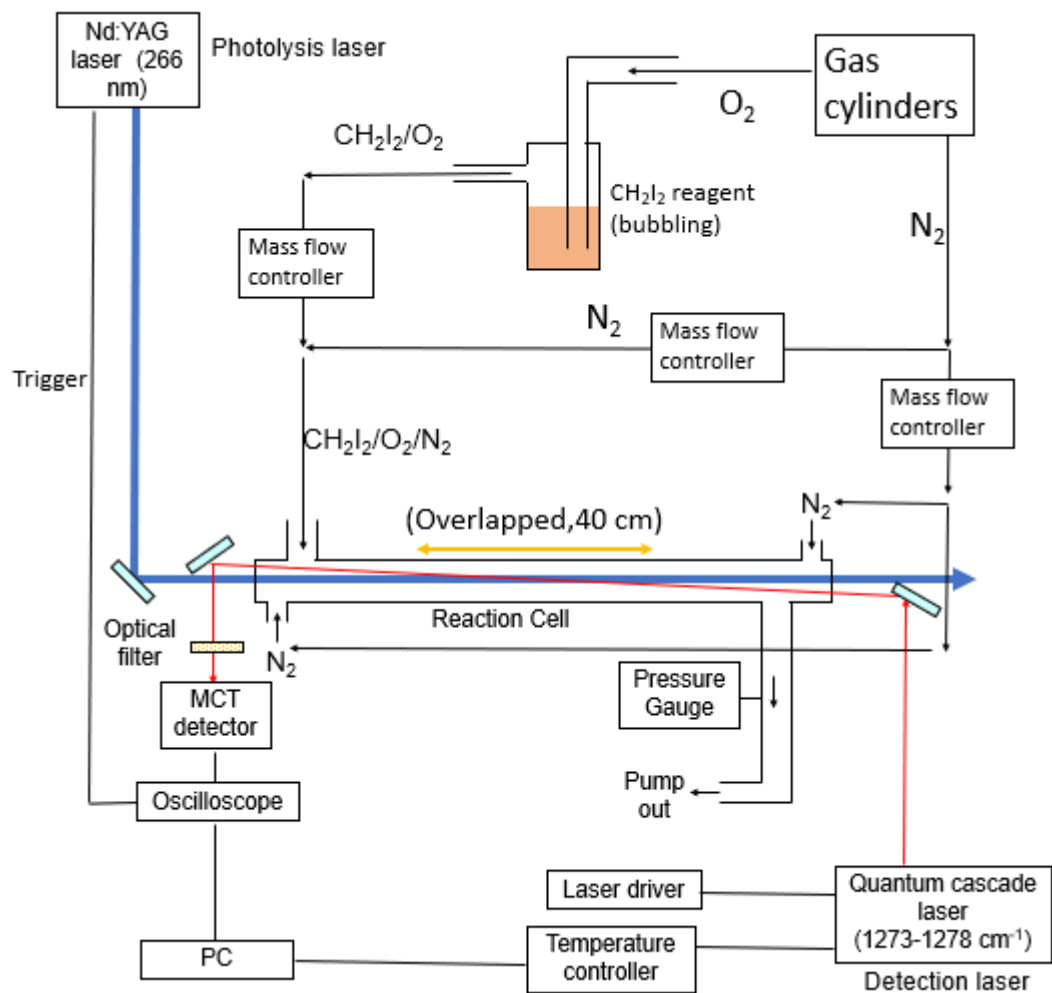
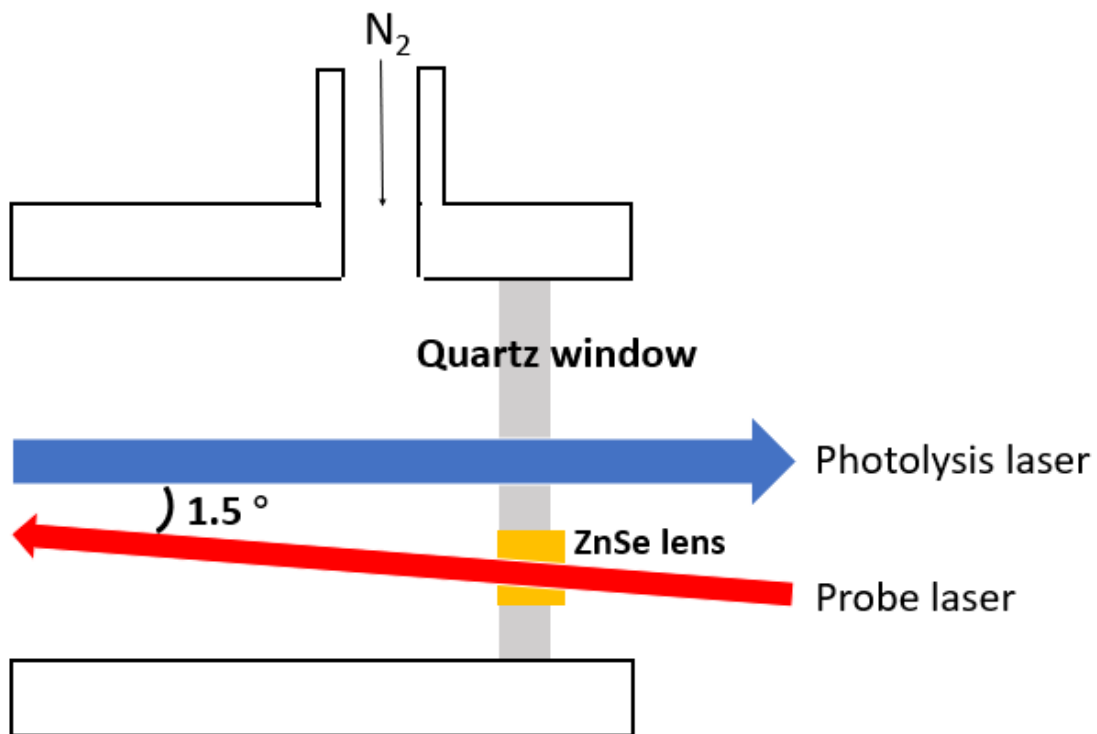Fig.2-2-1 Experimental setup for photolysis system of CH_2I_2/O_2 combined with a QCL laser as a probe laser.

Fig.2-2-2 Schematic description of how photolysis laser as well as probe laser pass though the reaction cell.
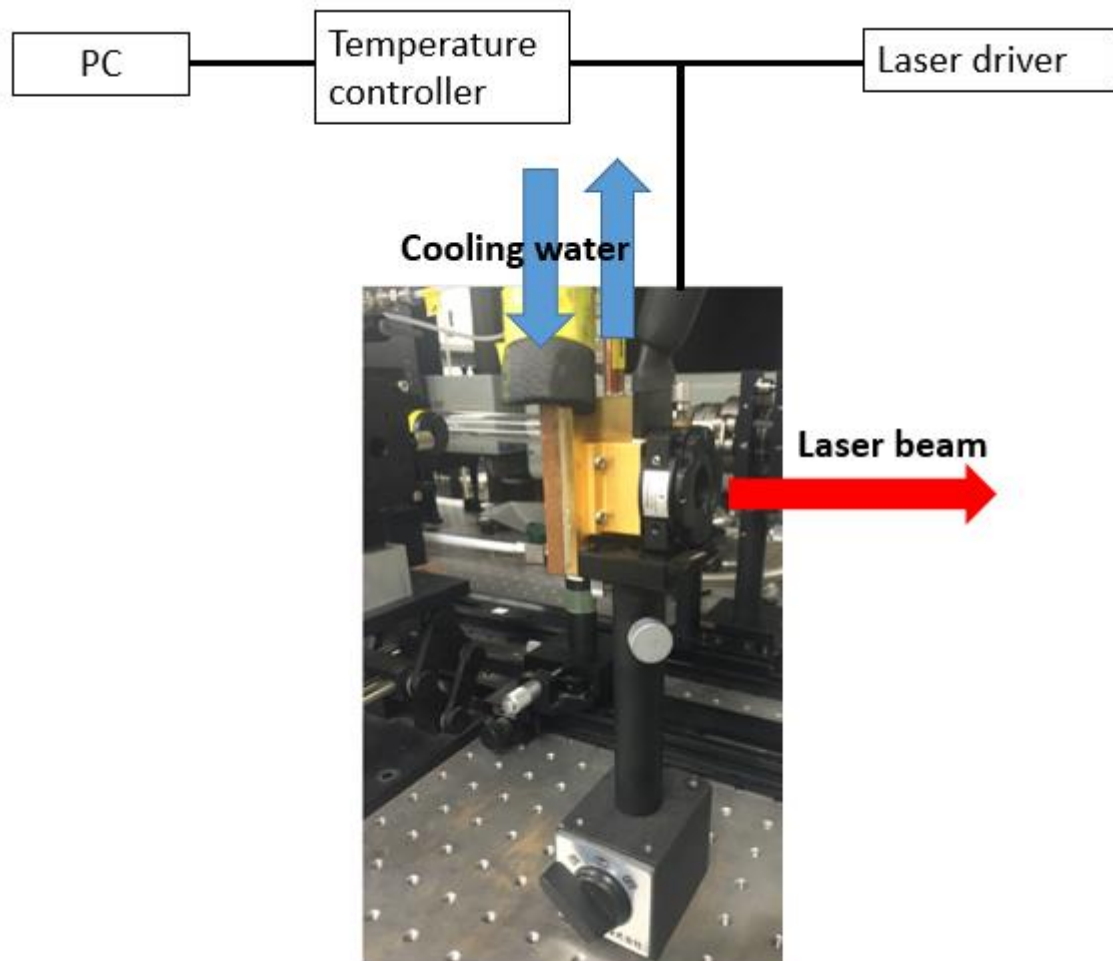
Fig.2-2-3 Continuous wave thermoelectrically-cooled DFB QCL (LC0069, Hamamatsu Photonics K.K., Hamamatsu, Japan) applied in this study.
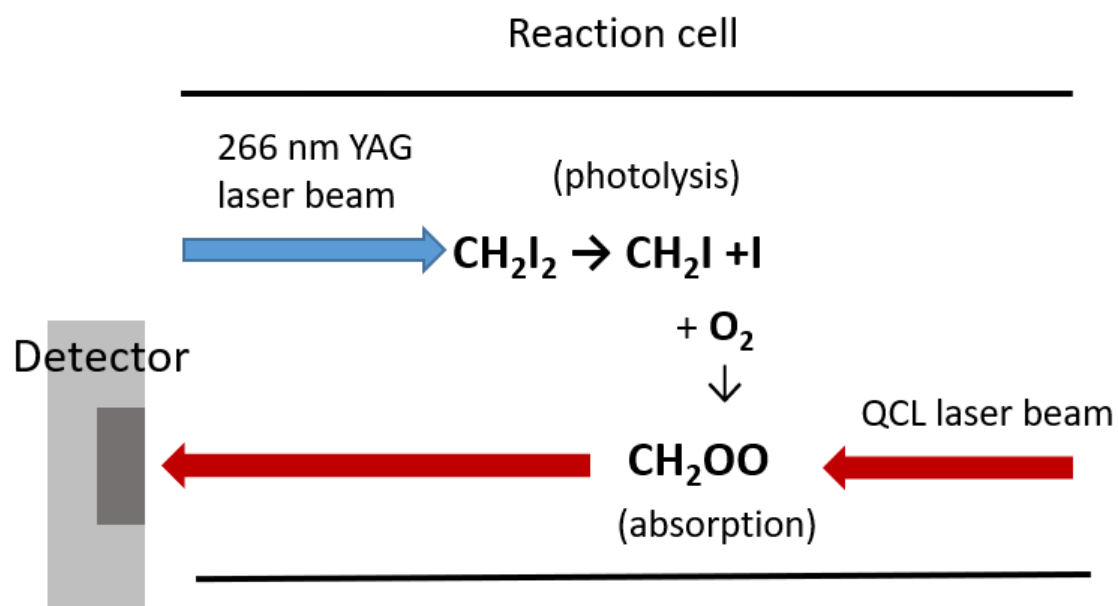
Fig.2-2-4 Schematic representation of generation and detection of CH_2OO in the photolysis laser and probe laser overlapped region.
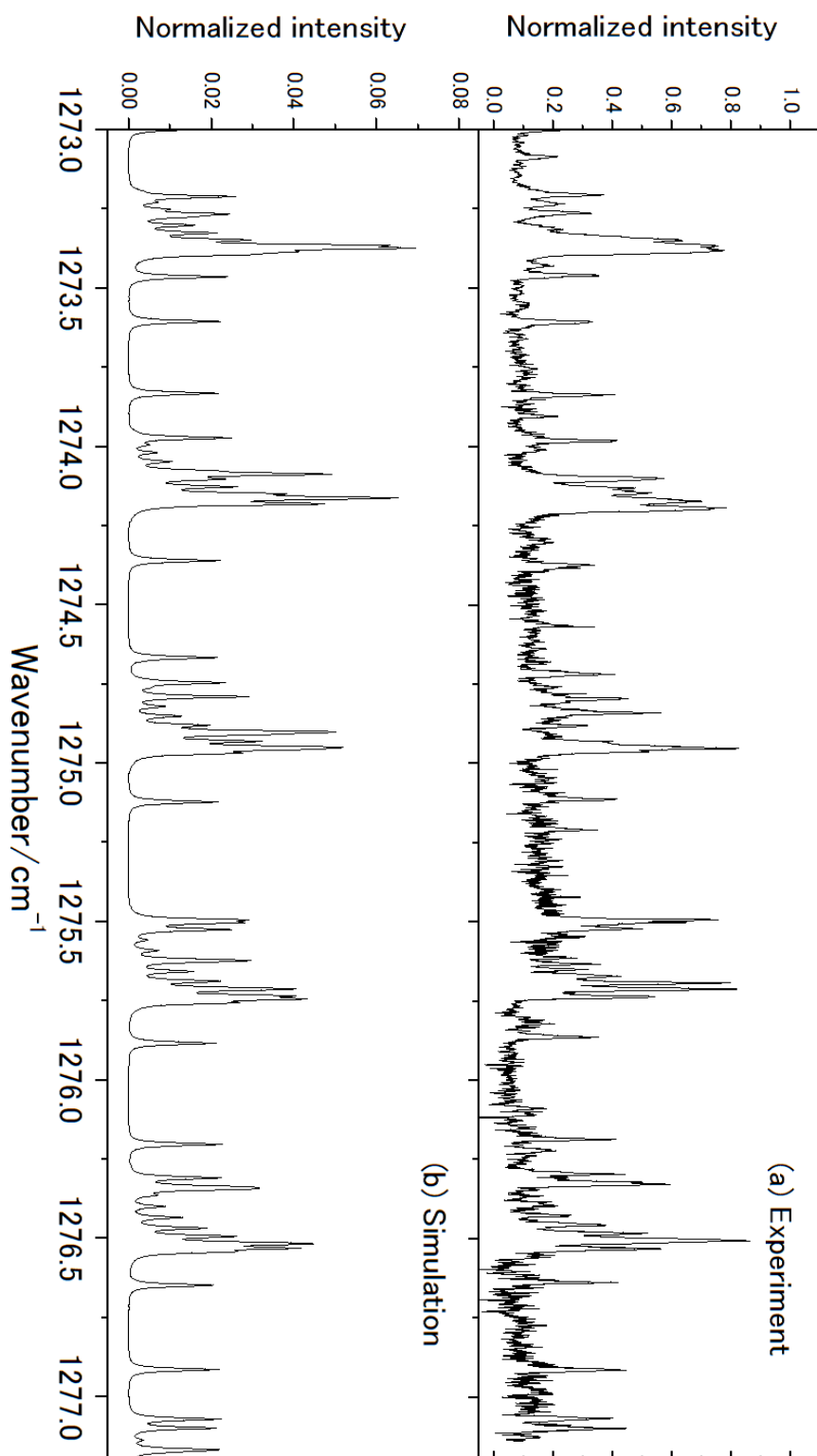
Fig.2-2-5 Comparison of (a) observed and (b) simulated spectra of CH₂OO. The absorption intensity units in both (a) and (b) are normalized, whereas, (b) is based on the most intensive region in the Fig.2-3-1, which is the Q-branch.[53]
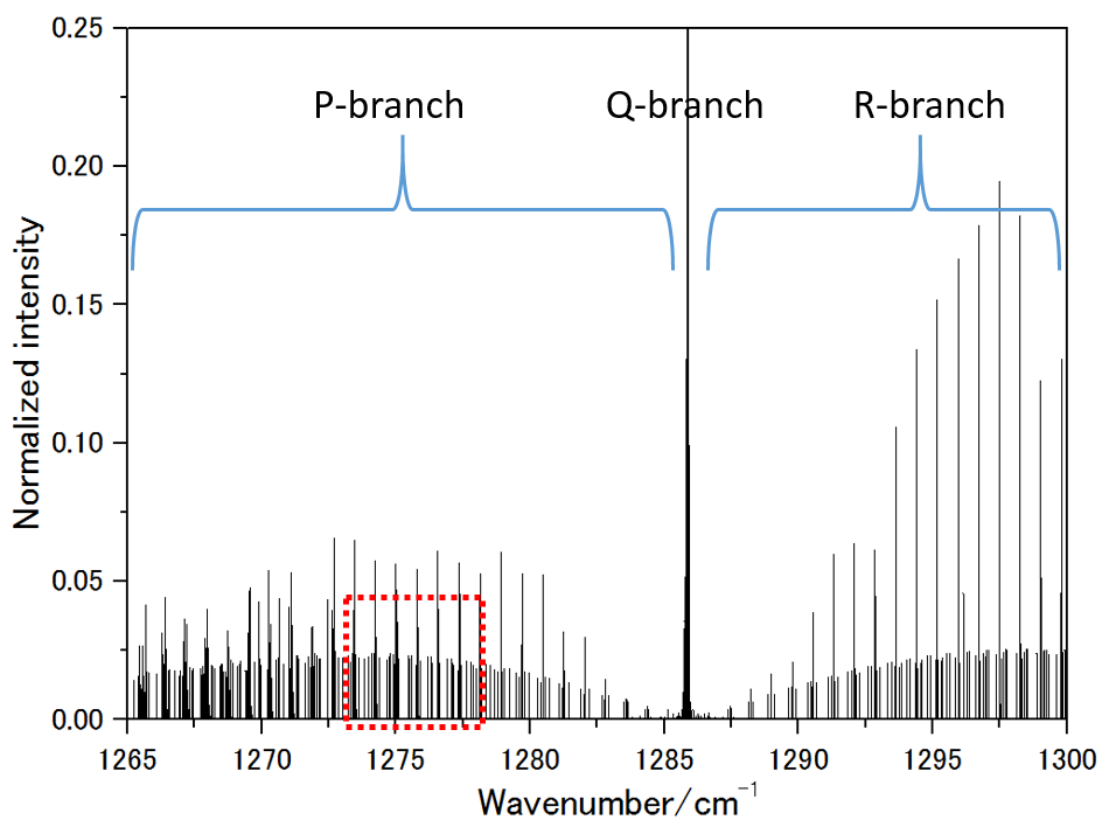
Fig.2-3-1 Simulated absorption spectrum of CH_2OO with a Pgopher program from 1265 to 1300 cm^{-1}. The region enclosed by red dots is covered by the QCL employed in this study, where is the (b) in Fig.2-2-5.

Table 2-3-1 Rotational constants as well as centrifugal distortion constants used in the Pgopher simulation. (unit: cm^{-1})

Constants	$v = 0$ [51]	$v_4 = 1$ [46]
Band Origin	0	1285.92797
A	2.59342579	2.5897027
B	0.41579342	0.4147254
C	0.35762622	0.3579765
$\Delta_J \times 10^6$	0.3889	0.4229
$\Delta_{JK} \times 10^5$	-0.2146	-0.6848
$\Delta_K \times 10^4$	0.886914	0.8395
$\delta_J \times 10^7$	0.780	0.728
$\delta_K \times 10^5$	0.23068	0.23068

Table 2-4-1 Positions of the same absorption lines in Fig.2-2-5 (a) and (b). (unit: wavenumber cm^{-1})

This work (ν_{exp})	Simulation (ν_{sim})	$\Delta\nu$ (= ν_{exp} - ν_{sim})	This work (ν_{exp})	Simulation (ν_{sim})	$\Delta\nu$ (= ν_{exp} - ν_{sim})
1273.085	—	—	1274.841	1274.789	0.052
1273.207	1273.211	-0.004	1275.111	1275.121	-0.010
1273.236	—	—	1275.23	—	—
1273.263	1273.268	-0.005	1275.493	1275.496	-0.003
1273.432	—	—	1275.521	1275.524	-0.003
1273.461	1273.464	-0.003	1275.865	1275.883	-0.018
1273.608	1273.605	0.003	1276.186	1276.204	-0.018
1273.836	1273.843	-0.007	1276.297	1276.31	-0.013
1273.906	—	—	1276.327	1276.343	-0.016
1273.983	1273.975	0.008	1276.393	1276.4	-0.007
1274.1	1274.087	0.013	1276.429	1276.436	-0.007
1274.303	—	—	1276.455	1276.468	-0.013
1274.373	1274.36	0.013	1276.483	1276.495	-0.012
1274.569	—	—	1276.637	1276.647	-0.010
1274.719	1274.666	0.053	1276.913	1276.913	0
1274.757	—	—	1277.068	1277.069	-0.001
1274.796	1274.745	0.051	1275.111	1275.121	-0.010

Chapter 3 Kinetic studies of Criegee intermediate in gas phase

3.1 Introduction

As mentioned in Chapter 1, OH radical was considered as the initiator for the oxidation of SO_2, and oxidation of SO_2 by sCIs was believed to be of little tropospheric importance until recently Mauldin et al.[4] reported the oxidation of SO_2 by some chemicals other than OH radical, which are subsequently referred as CIs. Especially in the boreal areas, where low concentration of water vapor facilitates the survival of sCI. The CH_2I_2/O_2 photolysis method introduced by Welz et al. provided a feasible way for both the characterization and kinetics researches about simplest CI, CH_2OO. The rate coefficient for the reaction of CH_2OO with SO_2 to be $(3.9 \pm 0.7) \times 10^{-11}$ cm^3 molecule^{-1} s^{-1} was measured in the aforementioned work at low pressure (4 Torr) and room temperature. Afterwards, new measurements[17]–[19] of this rate coefficient were performed using different approaches by monitoring the decay of CH_2OO or the generation of HCHO, and the results obtained were slightly dependent on pressure. The values of the rate coefficient for CH_2OO reacting with SO_2 is in good agreement with that reported in work of Welz et al.[16]

Welz et al.[16] also made their measurement of the rate coefficient for the reaction of CH_2OO with NO_2 in to be 7×10^{-12} cm^3 molecule^{-1} s^{-1} at a total pressure of 4 Torr. Ouyang et al.[54] confirmed the formation of NO_3 upon NO_2 addition to the same flowing mixture ($CH_2I_2/O_2/N_2$), under ambient atmospheric boundary layer conditions (760 Torr and 297 K). Distinct from the research on CH_2OO reacting with SO_2, few articles have discussed the reaction of CH_2OO with NO_2, and the rate coefficient for $CH_2OO + NO_2$ reported in these studies are listed in Table 3-1-1. Stone et al.[19] carried out a pressure dependence study of the rate coefficient for $CH_2OO + NO_2$, with laser-induced fluorescence spectroscopy, by monitoring the production of HCHO; HCHO is generated in this reaction from CH_2OO, which acts as an oxidant and loses one of its O atoms. They investigated the rate coefficients for $CH_2OO + NO_2$ at pressures between 25 Torr and 300 Torr and found no pressure dependence in the rate

coefficient for this reaction; they reported an average value of $(1.5 \pm 0.5) \times 10^{-12}$ cm^3 molecule^{-1} s^{-1}.

In all the kinetics studies of CH$_2$OO, by using a mid-infrared spectroscopic light source in detection of CH$_2$OO has not been discussed. A new method by combining a cw QCL as the spectroscopic light source with the CH$_2$I$_2$/O$_2$ photolysis system has been employed in the detection of CH$_2$OO, which is introduced in Chapter 2. This Chapter aims at specialized discussion on its extended usage in the researches on the reactivity of CH$_2$OO toward SO$_2$ and NO$_2$.

3.2 Experimental section for kinetic studies of CH$_2$OO

The absorption spectrum of CH$_2$OO recorded in our research has a strong absorption peak at 1273.356 cm^{-1}, where the QCL is operated at conditions: 50°C and near 620 mA. In contrast with other places where CH$_2$OO shows same absorption ability, the operation of the QCL at such conditions is stabilized, and a better signal to noise ratio (S/N) can be achieved. The decay signals of CH$_2$OO around this place were monitored explicitly as shown in Fig.3-2-1. The total pressure inside the reaction cell was kept at 10.4 Torr and the temperature is $(295 \pm 3 \text{ K})$. A slow flow of N$_2$ was introduced in the optical parts to protect the mirrors and the photolysis beam entrance windows from the deposition of reaction products.

The ratio of the CH$_2$I$_2$/N$_2$/O$_2$ mixture was roughly estimated to be 1:750:750. The initial concentration of CH$_2$I produced by the photolysis of CH$_2$I$_2$ at 266 nm was briefly calculated from the absorbed photolysis laser photon number:

$$[CH_2I]_0 = N_p[CH_2I_2]_0 \, \sigma(CH_2I_2)\Phi \qquad\qquad\qquad (E7)$$

where N_P is the laser photon number per pulse, calculated from the laser pulse energy $(4.6 \times 10^{16}$ photon cm^{-2}), $\sigma(CH_2I_2)$ is the absorption cross section of CH$_2$I$_2$ at 266 nm $(1.3 \times 10^{-18}$ cm^2 molecule^{-1})[55], and Φ is the quantum yield, 1[56], which represents

34

the probability that the absorption of a photon will cause the production of CH_2I in the photolysis of CH_2I_2. Based on the parameters listed above, the initial concentration of CH_2I_2 was calculated to be 2.3×10^{14} molecule cm^{-3}. $[CH_2I]_0$, formed by the photolysis of CH_2I_2, was 1.4×10^{13} molecule cm^{-3}.

Nevertheless, the concentrations of CH_2I radical and CH_2OO calculated by using such a method are lack of accuracy, because the amount of CH_2I_2 bubbled into the reaction cell by passing throughout O_2 gas was simply estimated based on the vapor pressure of CH_2I_2 and the pressure of O_2 gas, which failed in meeting up with the actual situation. Instead, a ChemkinII program[57] was employed in this study to simulate the time profile of CH_2OO in the CH_2I_2/O_2 photolysis system, for the reason that the rate coefficients for the reactions that compose the kinetic model describing the CH_2I_2/O_2 photolysis system, have been established by Ting et al.[11], which are listed in Table 3-2-1. Fig.3-2-1(A) shows the observed time profile of CH_2OO as well as the Chemkin fitted decay curves, the initial concentration of CH_2I, $[CH_2I]_0$ was adjusted to be about 2.1×10^{13} molecule cm^{-3}, and in such a condition, the contour of time profile of CH_2OO matched with its Chemkin fitted decay curve fairly well. $[CH_2OO]_{max}$ is around 1.6×10^{13} molecule cm^{-3}. A sensitivity analysis of temporal changes in the CH_2OO concentration is presented in Fig.3-2-1(B). At the start point ($t = 0$), where same amount of CH_2I and I are in this reaction system initiated by the photolysis of CH_2I_2. Rapid reaction of CH_2I with sufficient O_2 (at least a 10^4 times higher concentration) leads to the formation of CH_2OO and I radical. While the self-reaction of CH_2OO is mainly responsible for the decay of CH_2OO along with the generation of H_2CO. Around $t = 20$ μs, CH_2OO reaches its peak concentration. Some minor products generate in the subsequent reactions, and detailed information is listed in Table 3-2-1.

The detection limit (S/N = 2) for CH_2OO in the kinetic study was roughly estimated to be 2×10^{12} molecule cm^{-3}. The experimental setup employed in the work of Chang et al.[46], which has a better detection limit (less than 10^{12} molecule cm^{-3}). Nevertheless, concave mirrors were applied for multi-reflection of laser beams in their experiment, and a long overlap path up to 3.9 m was achieved. Instead, no optical reflective devices was used in this study, which simplified the experimental setup.

In the experiments of CH_2OO reacting with SO_2 or NO_2, SO_2 (Taiyo Nissan, SO_2 1%, N_2 99%)/NO_2 (Taiyo Nissan, NO_2 3%, N_2 97%) was injected into the reaction cell along with dilute gas N_2. The total concentration of the gases inside the reaction was calculated based on the ideal gas equation: $PV = nRT$, where P is the pressure, V is the volume, T is the absolute temperature, n is the number of moles of gas, and R is the ideal gas constant. The concentrations of SO_2 and NO_2 were derived from the total concentration according to their mixing ratios.

3.3 Kinetic research on CH_2OO reacting with SO_2

In the experiment of CH_2OO reacting with SO_2, SO_2 gas was added to a reaction cell containing $CH_2I_2/O_2/N_2$. The inside total pressure was 7.7 Torr. The $[CH_2OO]_{max}$ was estimated to be around 1.4×10^{13} molecule cm^{-3} without the addition of SO_2, and the concentration of SO_2 was varied from 4.2×10^{13} up to 4.2×10^{14} molecule cm^{-3}. In addition of SO_2, the decay rate of CH_2OO became obviously faster as presented in Fig.3-3-1.

The unimolecular decomposition of simplest Criegee intermediate, CH_2OO is negligible compared to its bimolecular self-reaction. And the bimolecular self-reaction of $[CH_2OO]$ is at least 10 times faster than CH_2OO reacting with other chemicals in the photolysis system of $CH_2I_2/O_2/N_2$, in the absence of SO_2. The rate coefficient of bimolecular self-reaction of $[CH_2OO]$ is reported about 3 times of that CH_2OO reacting with SO_2. Given the condition that the concentration of SO_2 has the dominant concentration among all the reactant, the reaction of CH_2OO with SO_2 and the bimolecular self-reaction of CH_2OO are mainly responsible for the decay of CH_2OO in addition of SO_2:

$CH_2OO+CH_2OO \rightarrow 2H_2CO+O_2$ (R5)

$CH_2OO+SO_2 \rightarrow H_2CO+SO_3$ (R6)
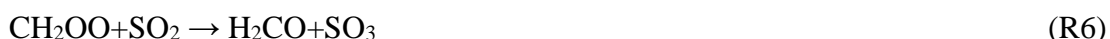
The equation describing the decay of CH_2OO can be written as:

$$\frac{d[\text{CH}_2\text{OO}]}{dt} = -2k_{self}[\text{CH}_2\text{OO}]^2 - k_1[\text{CH}_2\text{OO}][\text{SO}_2] \tag{E8}$$

The solution for this equation can be written as:

$$y = \frac{k_1{}'}{A\,exp(k_1{}'t) - 2bk_{self}} \tag{E9}$$

where y is signal intensity of CH_2OO which is proportional to the concentration of CH_2OO, $[\text{CH}_2\text{OO}] = by$. Based on the values of $[\text{CH}_2\text{OO}]_{max}$ and y_{max}, b is a constant. k_{self} for the self-reaction of CH_2OO was reported in the work of Ting et al.,[11] which is $(8 \pm 4) \times 10^{-11}$ cm^3 molecule^{-1} s^{-1}. k_1' is the pseudo-first-order rate constant and k_1' = $k_1[\text{SO}_2]$, which can be fitted from each decay curve of CH_2OO in addition of different concentrations of SO_2 by using the equation listed above. A can be written as

$$A = \frac{k_1{}'}{y_{max}\,exp(k_1{}'t_0)} + \frac{2bk_{self}}{exp(k_1{}'t_0)} \tag{E10}$$

when $t = t_0$, y reaches its max value, $y = y_{max}$. Combining the two equations above, gives

$$y = \frac{k_1{}'}{\left(\frac{k_1{}'}{y_{max}} + 2bk_{self}\right)exp(k_1't - k_1{}'t_0) - 2bk_{self}} \tag{E11}$$

Each decay curve used to determine a pseudo-first order rate coefficient, k_1', was gained after 200 laser shots and repeated 5 times, and an example of fitted curves is shown in Fig.3-3-1. The slope of the red line in Fig.3-3-2 is the rate coefficient k_1 for CH_2OO + SO_2, which was calculated to be $(3.6 \pm 0.1) \times 10^{-11}$ cm^3 molecule^{-1} s^{-1}. The error bars in

Figs.3-3-2 and 3-3-3 represent one standard deviation. Chemkin simulations were carried out for the first three plots in Fig.3-2-2, where the concentrations of SO_2 are 3, 6 and 12 times of CH_2OO, and the results in Fig.3-3-4 show that the decreases in $[SO_2]$ are less than 10% in 0 ~ 400 s. Fig. 3-3-5(B) is a sensitivity analysis of the temporal change in CH_2OO concentration in addition of $[SO_2] = 8.4 \times 10^{13}$ molecule cm^{-3}. The rise of CH_2OO is caused by rapid reaction of CH_2I with O_2 which is same to that in Fig.3-2-1(B), nevertheless, in the presence of SO_2, the self-reaction of CH_2OO and the reaction of CH_2OO with SO_2 determined the fate of CH_2OO. The rate coefficient for CH_2OO reacting with SO_2 gained in this work is in good agreement with the previous values of 3.1×10^{-11} ~ 4.2×10^{-11} cm^3 molecule^{-1} s^{-1} from direct measurements[14], [17], [18], which demonstrates that this new method is a powerful and convenient tool to investigate CH_2OO kinetics.

3.4 Kinetic research on CH_2OO reacting with NO_2

In this research, under a total pressure of 10.6 Torr, the concentration of NO_2 was changed from 2.2×10^{14} to 2.7×10^{15} molecule cm^{-3}. The rate coefficient for the reaction of CH_2I radicals with O_2, has been determined previously to be about 1.4×10^{-12} cm^3 molecule^{-1} s^{-1}[15] and the rate coefficient for $CH_2I + NO_2$ was reported to be 2.5 ~ 5×10^{-11} cm^3 molecule^{-1} s^{-1}[19]. The concentration of O_2 was kept 2~3 orders larger than NO_2 in this work to ensure enough generation of CH_2OO. The rate coefficient for the reaction of CH_2OO with NO_2 was measured, from the slope of the line in Fig.3-3-3, to be $(4.4 \pm 0.2) \times 10^{-12}$ cm^3 molecule^{-1} s^{-1}.

This value is slightly lower than 7×10^{-12} cm^3 molecule^{-1} s^{-1}, which was reported in the work of Welz et al.[16] and is in great agreement with the result calculated by Vereeken and Nguyen[58], that is 4.4×10^{-12} cm^3 molecule^{-1} s^{-1}.

The result obtained in this experiment can be valuable, since only Welz et al.[16] reported the value of coefficient for the reaction of CH_2OO with NO_2 by monitoring the decay of CH_2OO directly. As shown in Fig.3-4-1, the peak concentrations of CH_2OO

changed obviously in addition of different concentration of NO_2 because of rapid reaction of CH_2I with NO_2, in contrast to the work of Welz et al. (Fig.A3-1), in which they seem to fit all the time profiles of CH_2OO at a same peak concentration in spite of increasing concentration of NO_2. We carried out a sensitivity analysis as shown in Fig.3-4-2 (B). The result is similar with that reported in the work of $CH_2OO +SO_2$, in which the bimolecular self-reaction of CH_2OO, and the reaction of CH_2OO with NO_2 determined the fate of CH_2OO. The rapid rise in $CH_2I + NO_2$ curve is worth noting, indicating that the decay of CH_2OO is affected by this reaction at an early stage, which is caused by the decease in the concentration of CH_2I radical.

The application of this cw-QCL in the kinetic research of CH_2OO reacting with SO_2 has proved the feasibility of this new method. In a subsequent experiment, the rate coefficient for CH_2OO reacting with NO_2 has been measured. A few of previous studies have discussed the experimental measurement of rate coefficient for CH_2OO reacting with NO_2, since the amount of CI scavenged by NO_2 is negligible in contrast with water vapor in the atmosphere. Nevertheless, considering the oxidizing effect of CI, it may still play an important role in the oxidation of NO_2. In this study, a value of $(4.4 \pm 0.2) \times 10^{-12}$ cm^3 molecule^{-1} s^{-1} for the rate coefficient of CH_2OO reacting with NO_2 was provided, which is about 1/3 smaller than that previously reported by Welz et al.[16] that is used in the evaluation of oxidizing effect of CI upon NO_2. As a result, predicted oxidation of NO_2 initiated by CI can be reduced to some extent.

The experimental setup applied in this work still has the potential to be enhanced in detection limit and precision by employing some multi-reflective devices. The laser beam emitted by the QCL led directly into the detector, and the intense beam was cut down right before the detector by an IR filter to avoid overloading the detector. In other words, if the reflection time of the laser beam was increased in the experiments, a better optical length would have been achieved, and both the detection limit and the precision would have been modified. The QCL used in this research did not cover the strongest absorption region in the v_4 band of CH_2OO, but still provided explicit kinetics profiles because of its high time resolution as well as powerful light source. And it has the chance to be performed better in the kinetics experiments of some other larger CIs. As

shown in Fig.A3-2, the next larger CI, CH$_3$CHOO, which has an intense absorption band around 1280 cm^{-1}, which is extremely close to the region covered by our QCL, 1273-1278 cm^{-1}.
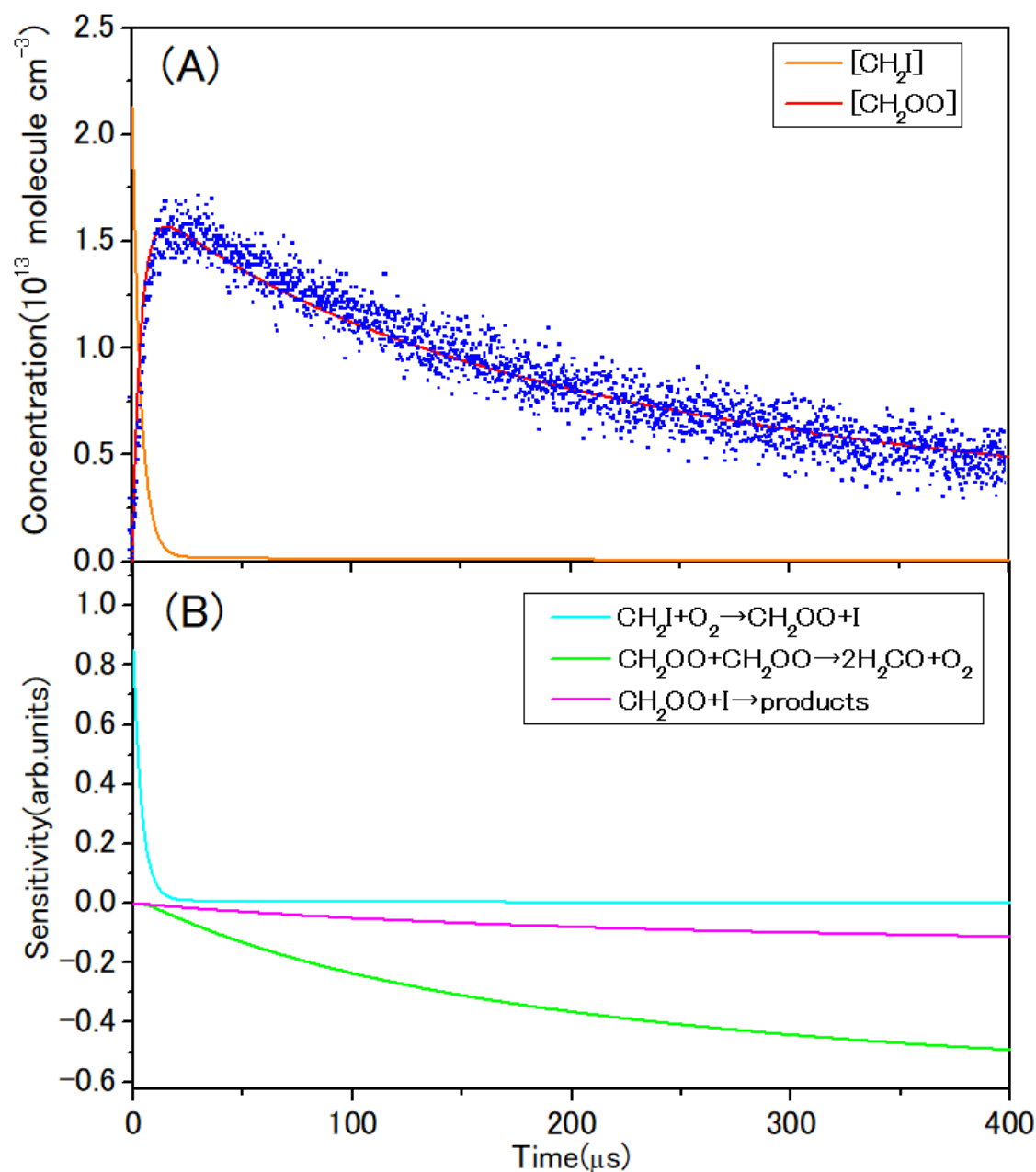
Fig.3-2-1 (A) Time profile of CH_2OO without addition of NO_2/SO_2 to the reaction cell. The red and orange curves are the Chemkin fitting results. The concentration of CH_2OO is given based on the results obtained in Chemkin simulation. (B) Sensitivity analysis of the temporal changes in the CH_2OO concentration performed with Chemkin. This analysis suggests that the rise part of CH_2OO is governed by the $CH_2I + O_2$ reaction, while the decay part is due to (1) Major: the rapid self-reaction of CH_2OO, with the production of H_2CO; (2) Minor: the reaction of $CH_2OO + I$. Details for these reactions are listed in Table 3-2-1.
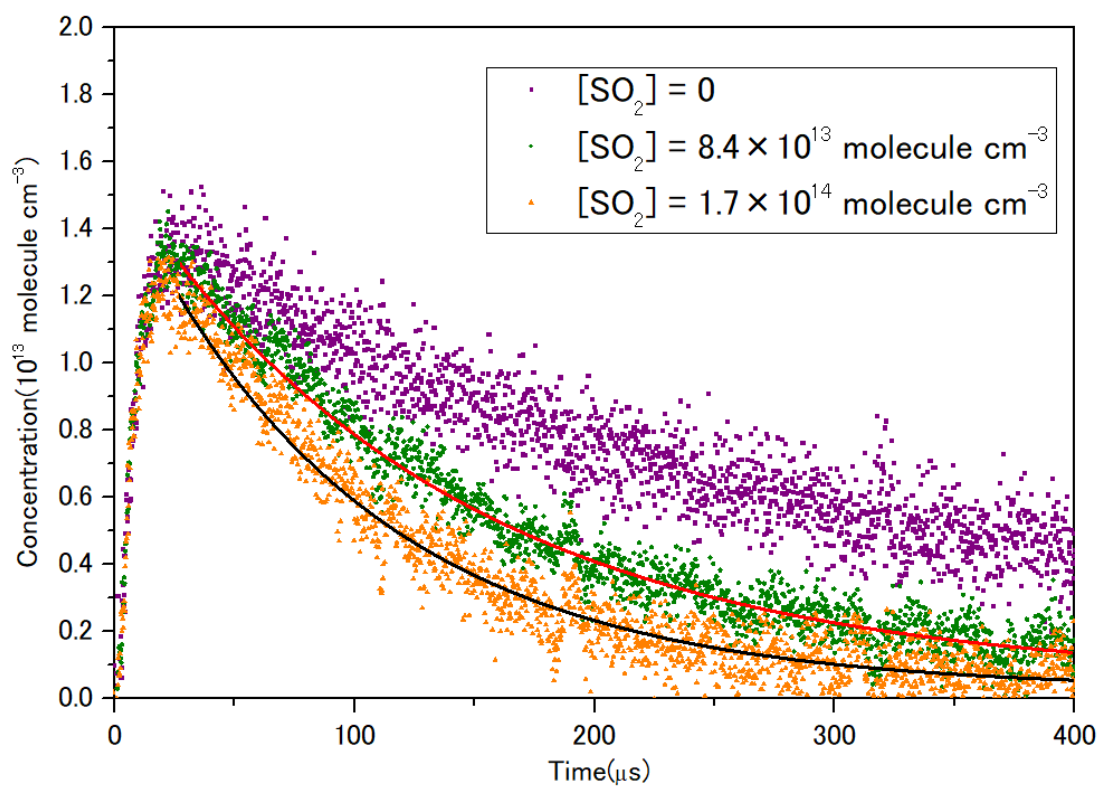
Fig.3-3-1 Time profiles of CH_2OO in addition of different concentrations of SO_2, and their fitted curves derived from (E11). (red and black lines).
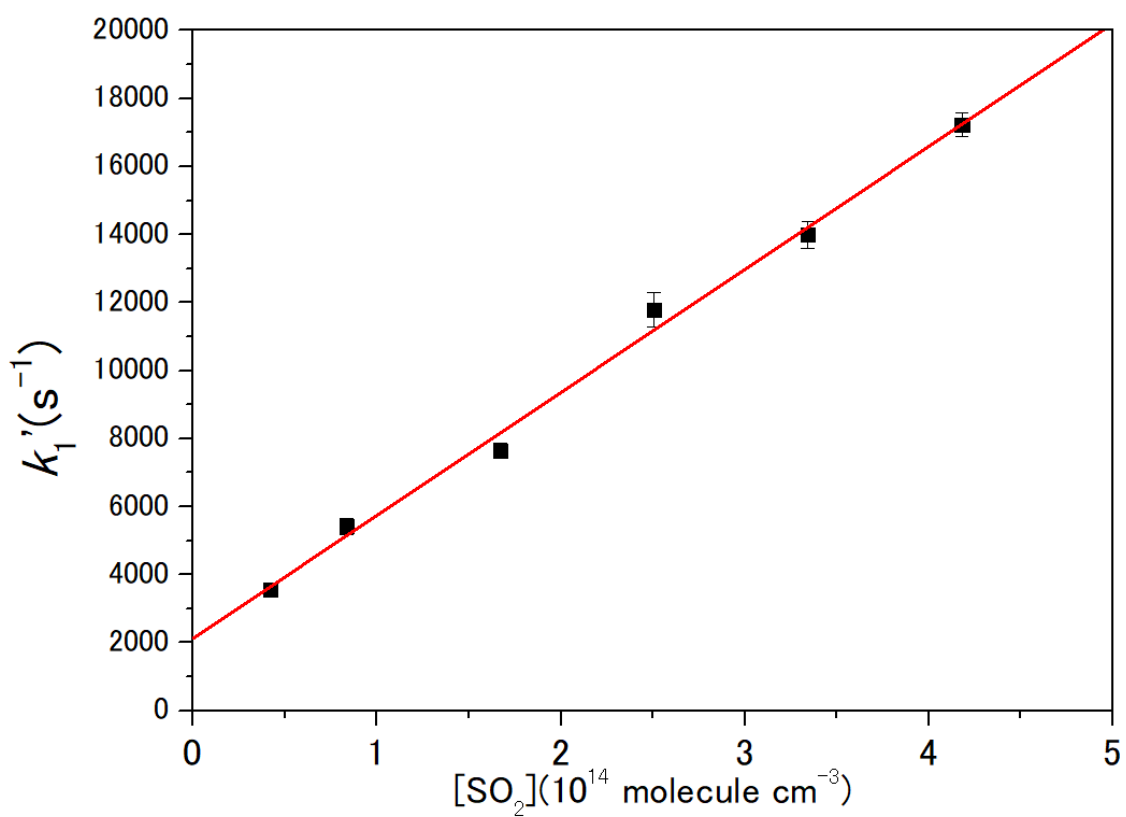
Fig.3-3-2 Plots of the pseudo-first-order rate coefficients, k_1', for the decay of CH_2OO in the presence of SO_2. The concentration of SO_2 changed inside the reaction cell at a total pressure of 7.7 Torr and a temperature of 295 ± 3 K. The slope of the fitted red line is the rate coefficient for the reaction $CH_2OO + SO_2$.[53]
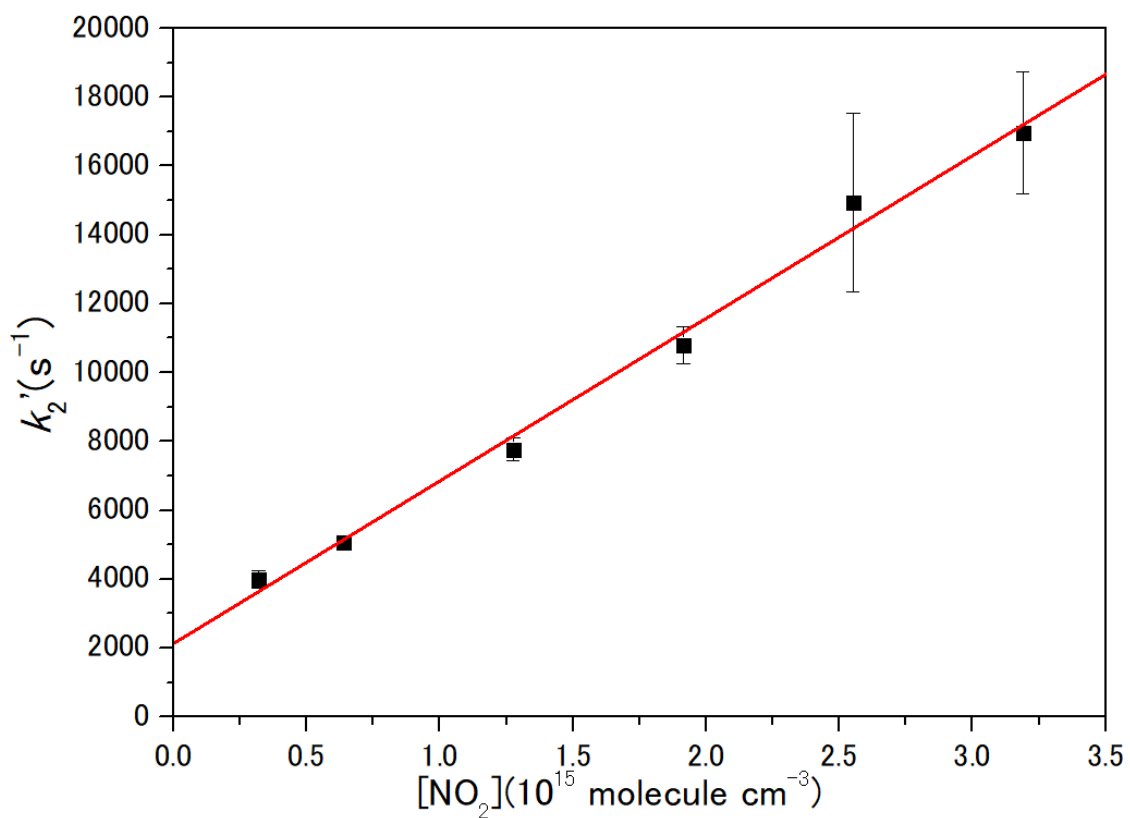
Fig.3-3-3 Plots of pseudo-first-order rate coefficients, k_2', for the decay of CH_2OO in the presence of NO_2. The total pressure is 10.6 Torr inside the reaction cell and the temperature was kept at 295 ± 3 K. The fitted red line gives the value of the rate coefficient for $CH_2OO + NO_2$.[53]
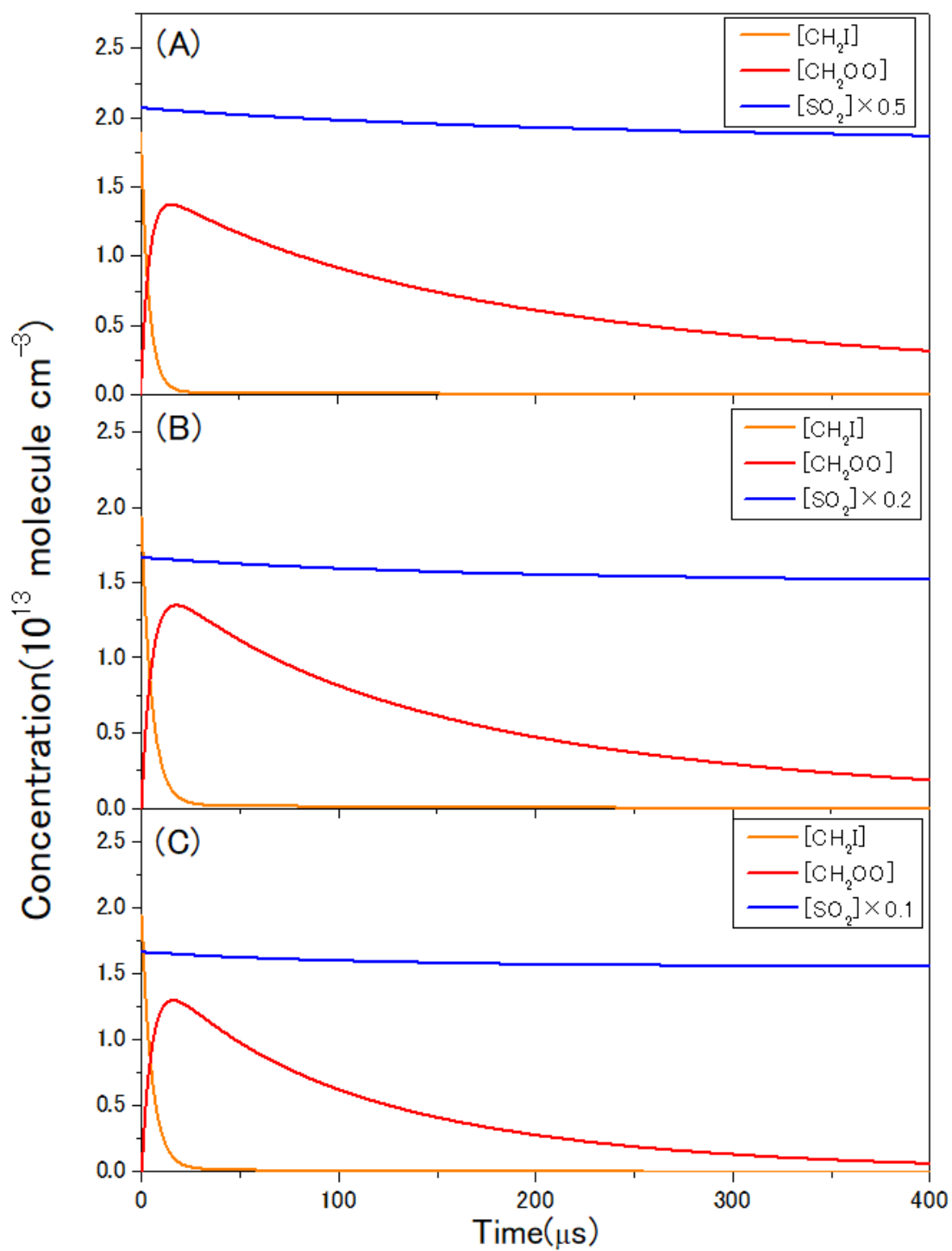
Fig.3-3-4 Chemkin simulation for CH₂OO reacting with SO₂ in addition of (A) [SO₂] = 4.2×10^{13} molecule cm⁻³, (B) [SO₂] = 8.4×10^{13} molecule cm⁻³, (C) [SO₂] = 1.7×10^{14} molecule cm⁻³.
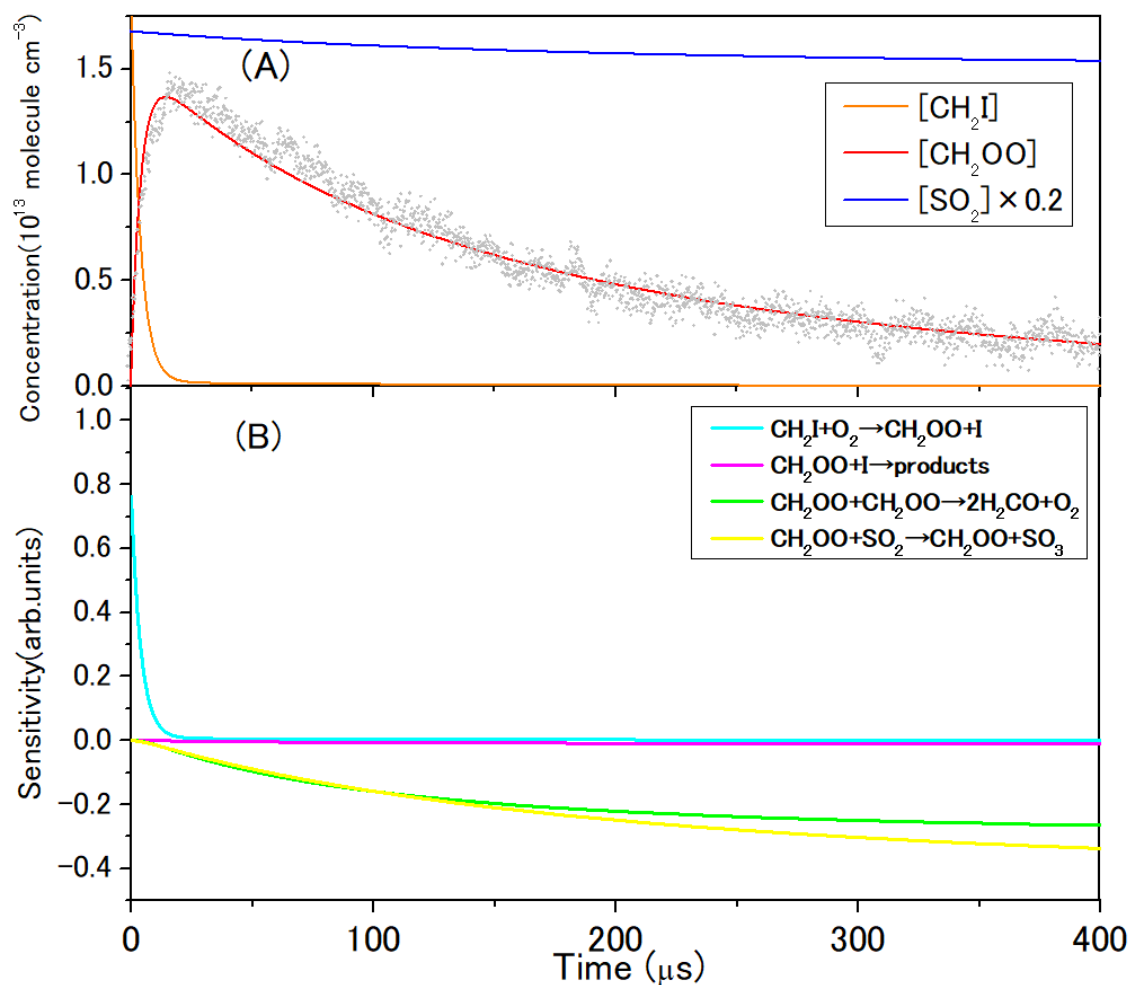
Fig.3-3-5 (A) Time profile of CH_2OO in addition of $[SO_2] = 8.4 \times 10^{13}$ molecule cm^{-3} to the reaction cell. The red, orange and blue curves are the Chemkin fitting results. (B)Sensitivity analysis of the temporal changes in the CH_2OO concentration performed with Chemkin. This analysis suggests that CH_2OO rises from the $CH_2I + O_2$ reaction, while the decay of CH_2OO is due to the rapid self-reaction of CH_2OO as well as its reaction with SO_2, with the production of H_2CO and SO_3. And the reaction of $CH_2OO +$ I contributed a negligible effect on the temporal concentration change of CH_2OO. Details for these reactions are listed in Table 3-2-1.
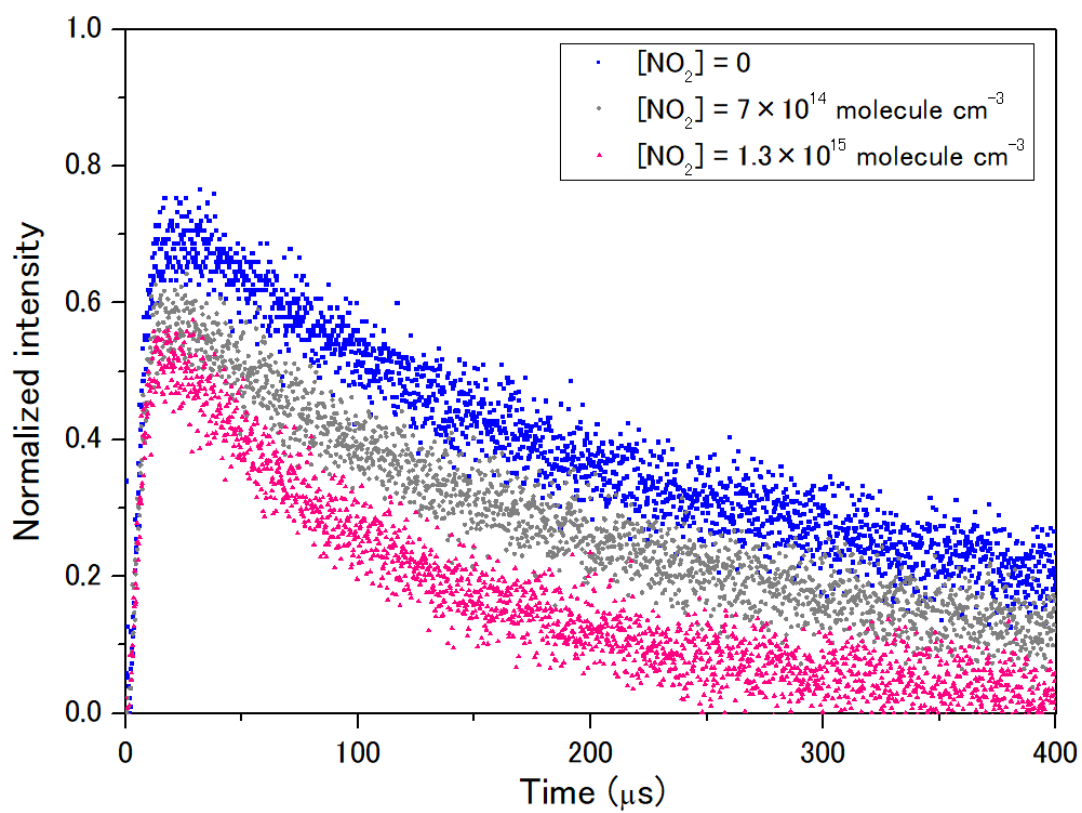
Fig.3-4-1 Time profiles of CH$_2$OO in addition of different concentrations of NO$_2$
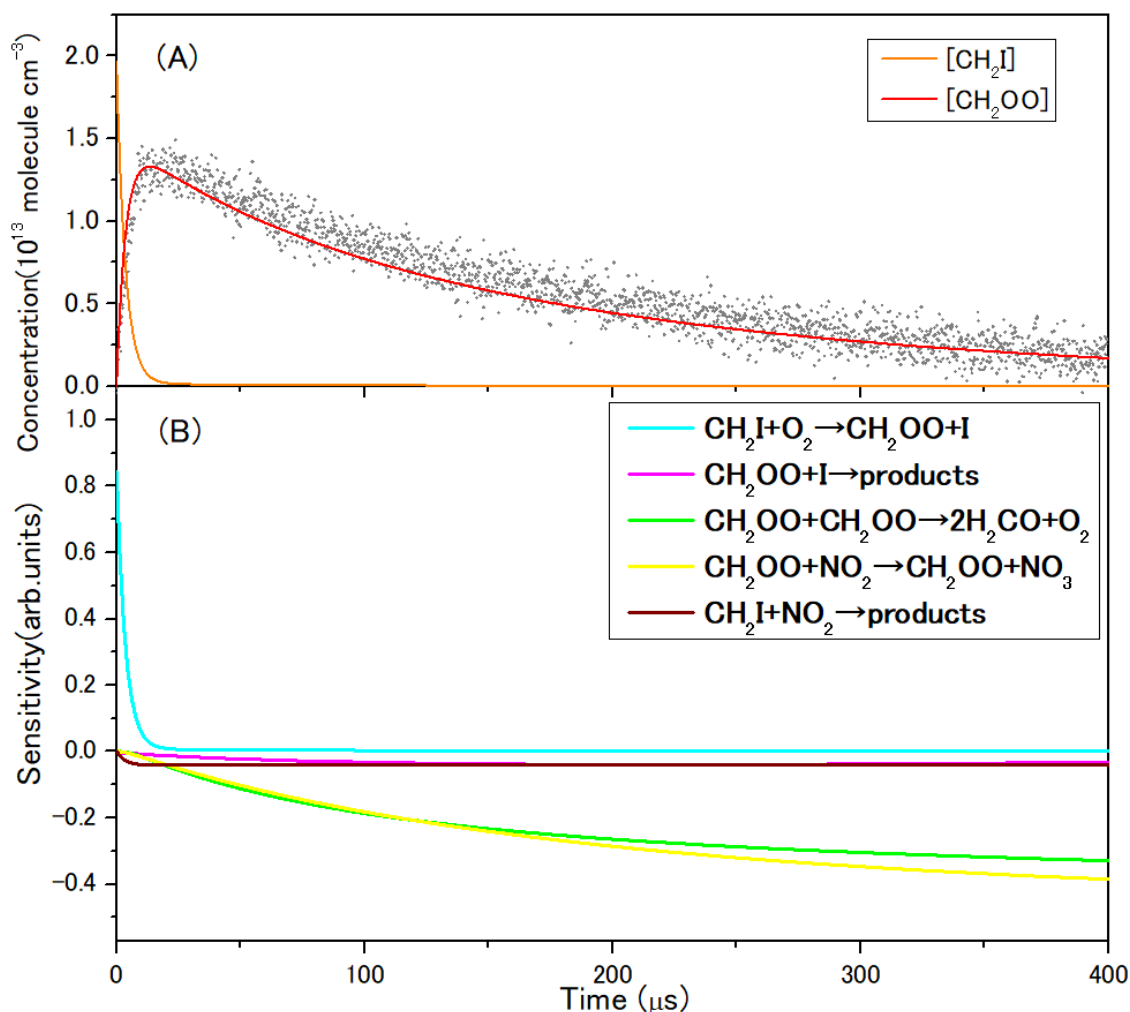
Fig.3-4-2 (A) Time profile of CH_2OO in addition of $[NO_2] = 7 \times 10^{14}$ molecule cm^{-3} to the reaction cell. The red, orange and blue curves are the Chemkin fitting results. (B)Sensitivity analysis of the temporal changes in the CH_2OO concentration performed with Chemkin. This analysis is similar with that presented in the work of $CH_2OO + SO_2$. CH_2OO rises from the $CH_2I + O_2$ reaction, while the decay of CH_2OO is almost determined by the rapid self-reaction of CH_2OO as well as its reaction with NO_2. The reactions $CH_2OO + I$ and CH_2I+NO_2 contribute minor effect on the decay of CH_2OO. The sharp rise in CH_2I+NO_2 curve indicates that this rapid reaction indirectly affects the concentration of CH_2OO at an early stage, which is due to the decease in the concentration of the precursor, CH_2I radical. Details for these reactions are listed in Table 3-2-1.

Table 3-1-1 Rate coefficient for $CH_2OO + NO_2$ reported in previous studies and obtained in this work.

$k(CH_2OO + NO_2)/$ cm^3 molecule^{-1} s^{-1}	Descriptions	References
7×10^{-12}	Direct observation of CH_2OO, using multiplexed photoionization mass spectrometry	Welz et al.[16]
$(1.5 \pm 0.5) \times 10^{-12}$	Monitoring the production of HCHO generated in self-reaction of CH_2OO by using laser-induced fluorescence spectroscopy.	Stone et al.[19]
4.4×10^{-12}	Theoretical calculation	Vereeken and Nguyen[58]
$(4.4 \pm 0.2) \times 10^{-12}$	Direct observation of CH_2OO, using a cw-QCL	This work

Table 3-2-1 Rate coefficients adopted in Chemkin simulation.
(units: s^{-1} for 10, and cm^3 molecule^{-1} s^{-1} for others)

Reactions		Rate coefficients
1	$CH_2I+O_2 =>CH_2OO+I$	1.2×10^{-12}
2	$CH_2I+O_2 =>ICH_2OO$	6.0×10^{-14}
3	$CH_2I+O_2 =>$ products other than CH_2OO or ICH_2OO	2.4×10^{-13}
4	$CH_2OO+CH_2OO =>2H_2CO+O_2$	1.2×10^{-10}
5	$CH_2OO+I =>CH_2I+O_2$	7.9×10^{-11}
6	$CH_2OO+I =>ICH_2OO$	3.3×10^{-12}
7	$CH_2OO+I =>H_2CO+IO$	9.0×10^{-12}
8	$ICH_2OO+ICH_2OO =>2ICH_2O+O_2$	9.0×10^{-11}
9	$ICH_2OO+I =>ICH_2O+IO$	3.5×10^{-11}
10	$ICH_2O =>H_2CO+I$	1.0×10^{5}
11	$IO+IO =>$products	9.9×10^{-11}
12	$CH_2OO+SO_2 =>H_2CO+SO_3$	3.6×10^{-11}
13	$CH_2OO+NO_2 =>H_2CO+NO_3$	4.4×10^{-12}
14	$CH_2I+NO_2 =>$products	2.5×10^{-11}

Chapter 4 Reactions of Criegee intermediates on gas-liquid interfaces

4.1 Introduction

As introduced in Chapter 1, Enami et al.[43] reported a research of Criegee chemistry on gas-liquid interfaces by combining a pneumatic electrospray ionization technique with a quadrupole mass analyzer.

In this experiment, α-humulene (α-H, molecular structure in Table 1-1-1) was mixed into an acetonitrile/water (W/AN) mixture with some NaCl added in. The solution was injected into a spraying chamber as shown in Fig.A4-1. At the nozzle of a nebulizer, the droplets pushed into the chamber by a syringe get crushed by nebulizer gas N_2, and form even smaller droplets. Large organic molecules, such as α-H, prefer to stay at the outermost layers of these droplets because of their hydrophobicity, and get exposed to O_3 come from an orthogonal direction. The attachment of Cl^- on neutral products generated in the ozonolysis provides a negative charge, which can be detected by a mass analyzer in negative mode. Acetonitrile and water are mixed at a ratio of 4/1, and the composition of its interfacial layers was well characterized.[34], [35], [59]–[62]

Fig.A4-2 shows mass spectra of the anions produced in the ozonolysis of α-H and subsequent reactions on the surface of droplets while 1.0 mM α-H + 0.2 mM NaCl in W/AN (1:4 = vol:vol) solutions are injected into the chamber. Signals rose up significantly at places where m/z = 305/307, which were assigned to be the Cl- adducted products of α-H initiated CI reacting with H_2O (204 + 48 + 18 + 35/37 = 305/307). The ratio of m/z = 305 and 307 was 3 to 1, corresponding to nature ratio of ^{35}Cl and ^{37}Cl, which was 3 to 1 as well.

Subsequent studies[55]–[58] carried out by the same group, including the researches on reactivity of CI toward hexanoic acid, levoglucosan, and cis-pinonic acid, elucidated some characteristics of Criegee chemistry on air-liquid interface.

Similar experiments were tested by using another sesquiterpene, β-caryophellene (β-C, molecular structure in Table 1-1-1) additionally. 100 mM hexanoic acid (MW = 116) was added in the solution injected into the chamber. The results are presented in

Fig.A4-3. Not surprisingly, the products of β-C initiated CI reacting with water was detected as shown in Fig.A4-3 (B). Simultaneously, new peaks rise at m/z = 403/405, which are assigned to be the products of CI reacting with hexanoic acid (204 + 48 + 116 + 35/37 =403/405), indicating that 100 mM hexanoic acid compete with H_2O for CI on the surface of W/AN mixtures that macroscopically are ~11 M water. These reaction processes are listed in Fig.A4-4. As introduced in Chapter 1.3, in gas phase organic acids show great reactivity toward CIs, because R_nCOOH gives out an H atom easily, which facilitates the insertion reaction of CI into an organic acid between R_nCOO group and H.

Followed by another work[64], in which, levoglucosan (Levo), a major component of aerosols produced from biomass burning, was selected to react with CI at the gas-liquid interface. 1 mM β-C + 0.2 mM NaCl + 100 mM Levo were mixed in W/AN (1:4 =vol:vol) solution and injected into the chamber, in the absence and presence of O_3(g). Levo is surface-active, therefore, in the absence of O_3, intense signals appear at m/z = 197/199 at a signal ratio of 3/1, which are assigned to the products of Cl^- ($^{35}Cl/^{37}Cl$ = 3/1) adducted on Levo. In addition of O_3, signals 197/199 decreased obviously with new peaks rise up, to which are contributed by the reactions of CI generated in the ozonolysis of β-C with Levo. Signals 449/451 are assigned to the products of CI reacting with Levo (204 + 48 + 162 + 35/37 = 449/451). As shown in Fig.A4-5, signals 449/451 are almost 3 times of 305/307 which have been determined as the products of CI reacting with water. This surprising result implies that Levo is an effective scavenger for CI at gas-liquid surface, because of the surface-activity of Levo as well as its reactivity toward CI.

Cis-pinonic acid (CPA, MW 184, Fig.A4-6) is a main product of the atmospheric oxidation of biogenic α-pinene emissions and a major component of secondary organic aerosol. CPA has been proved as anther effective scavenger for CI at gas-liquid surface.[65] As presented in Fig.A4-8, intense peaks appear at both m/z = 305/307 and 471/473 (204 + 48 + 184 + 35/37 = 471/473), which are assigned to the products of CI reacting with water and CPA correspondingly, with only 10 mM CPA added in the solution compared with overwhelmingly higher concentration of water, 11 M. The peaks

appearing at m/z = 431/433 (204 + 48 + 144 + 35/37 = 431/433) is caused by an addition of 10 mM octanoic acid (OA, MW 144, Fig.A4-7) in the solution. OA is a surface-active carboxylic acid commonly observed in ambient particles. Relatively inertly reactive toward CI, which OA is, compared to CPA, the yield of m/z 431 is only 1/4 of m/z 471. CPA likely lies flat on the surface exposing its hydrophobic cyclobutane-ring to air, and keeping the hydrophilic carbonyl –C(O)– and the reactive carboxylic –C(O)OH groups lying immediately below,[68] in contrast with OA, whose –C(O)OH is likely buried deeper in bulk water. The steric effect plays an important role in Criegee chemistry on the gas-liquid interface.

In this chapter, the experimental set up developed by Enami et al., which is used specialized for the detection of the products generated on gas-liquid interfaces, is applied in the researches on investigating the structure dependent reactivity of CI on gas-liquid interfaces.

4.2 Experimental techniques

4.2.1 Electrospray ionization mass spectrometry

Electrospray ionization is a so-called "soft" technique used in the detection of ions contained in aerosols, because the ions can be softy attached on the analytes of interest instead of crashing them into fragment. The aerosols are generated from dispersion of liquid solutions by electrospray, which is specifically described in Fig.A4-9. In a positive mode for an electrospray ionization mass spectrometer, the power supply connects the spraying nozzle to the outlet, where electrons are kept transporting. As a result, the accumulated like charges would be repelled by the capillary of the same polarity, and then they would move towards the liquid surface at the capillary outlet, where a cone which is called a Taylor cone[69] (named after the scientist Taylor who contributed theoretically description to such a situation). Then, analyte solution droplets drift into the chamber area, and this process repeats frequently due continuous work of the power supply and the vacuum pump.

The high voltage applied between the spraying nozzle and the outlet is not only responsible for the transportation of electrons. Such a potential difference can heat up the capillary, which accelerates the solvent evaporation from the droplets. As well, high-speed nebulizer gas (inert gas is usually used, such as N_2) has the ability of crashing the droplets into smaller ones.(Fig.A4-10)

There are two forces in determining the shape of a charged droplet. One is surface tension, which is pointing to the center of a droplet, and tries to retain its spherical shape. The other is Coulomb force, which exists among like charges in the droplet. The Coulomb force plays an opposite effect to the surface tension, which tries to break down the spherical shape of the charged droplet. Continuous solvent evaporation from a droplet leads to the Rayleigh limit[70] of this droplet. At this point, the Coulomb force overcomes the surface tension of a droplet, and the droplet starts exploring to form smaller offspring droplets, which is known as Coulomb fission. The new droplets undergo evaporation as well as subsequently further Coulomb fissions, and finally compounds dissolved inside get into gas phase.

Two major theories have been postulated in explaining the final step of the production of gas-phase ions, which are the charge residue model (CRM) and the ion evaporation model (IEM). CRM was firstly hypothesized by Dole et al.,[71] and subsequently revised by Schmelzeisen-Redeker et al.,[72] which suggests that after repeated evaporation and Coulomb fission, all the analyte molecules are separated into different small charged droplets, which means one droplet contains only one analyte molecule. The size of these extremely small droplets are $R \approx 1$, and subsequent desolvation leads to the charges attached on the analyte. While, the IEM[73]–[75] suggests that a limit of the size of the charged droplets can be achieved, after a serious of evaporation and Coulomb fission, when direct emission of the charged analytes are available because the interaction of the electric field and charges is strong enough.

The addition of a proton or some other cation like sodium onto the analyte, $[M + H]^+$ or $[M + Na]^+$, are often observed. Multiply charged ions such as $[M + nH]^{n+}$ can be detected as well. In a negative mode, the analyte can be detected as the formations of the removal of a hydrogen nucleus, $[M - H]^-$, or the adduct of some anions such as

chloride ion, [M + Cl]$^-$.

4.2.2 Quadrupole mass analyzer

As the name implies, a quadrupole mass analyzer consists of four parallel cylindrical rods, which is presented in Fig.A4-11. The direct as well as alternating voltages are applied between two of four rods. With a settled mode, the trajectory of moving ions throughout the rods are determined by their mass-to-charge ratio (m/z).

A direct and alternating voltage is applied between the rods in order to affect the movement of the ions. In the case of the positive mode, a rod with positive potential repels the ions while a rod with negative potential attracts the ions and traps them. If an alternating voltage is applied, then the chance for the ion hitting the metal rod depends on the charge and mass of the ion and also on the strength of the field and the frequency of the oscillation. If a positive ion has a small mass, then it can be easily affected and will quickly be accelerated towards the rod with negative potential. However, heavier ions are not so much affected. The strength of the field and frequency of the oscillation can be tuned by the operator and used to manipulate with the ions. For example, if the frequency is too high, then the ion simply has no time to react and nothing happens. However, if the frequency is too low, then the ion is pulled into a rod before the potential flips.

If the DC fields and AC fields are combined, then the positive ions are forced in the middle the two positive rods (Fig.4-2-1), while the AC field destabilizes them. If the ions possess of high mass or low charge then they are hardly affected by the AC field and their trajectory is mostly determined by the DC field. The trajectory of the ions with too small mass-to-charge ratio however is strongly destabilized by the AC field and causes them to crash into a rod.

Electrodes with negative DC voltage attract positive ions. The only way to prevent the positive ions from hitting the rods is to apply a suitable AC voltage, which keeps

them between the rods (Fig.4-2-2). However, only ions with a smaller mass are affected by the AC field and ions with too high mass-to-charge ratio will crash into the rods.

In the quadrupole, there are four rods however where two rods have a negative DC voltage and two have a positive DC voltage. The opposing positive rods let through only high mass-to-charge ratio ions while the opposing negative rods let through only ions with smaller mass-to-charge ratio. If the voltages are correctly selected, then in a narrow mass-to-charge ratio range, ions can pass through the rods and interact with the detector. In a real system this narrow mass-to-charge ratio range is scanned from very small to large values, by playing with the electrical parameters in order to detect ions with different mass-to-charge ratio.

4.3 Experimental method and instruments[66]

The experimental method is almost same to that reported in the previous works by Enami et al.[43], [63]–[65] A mixture of [β-C + NaCl + benzoic acid] or [monoterpenes + NaCl] in W/AN (1:4 = vol:vol) microjets is introduced into the spraying chamber of an electrospray mass spectrometer (ES-MS, Agilent 6130 Quadrupole LC/MS Electrospray System at NIES, Japan, Fig.4-3-1). Microjets are exposed to orthogonal gas-phase O_3/O_2 beams. W/AN solutions containing β-C, NaCl, and BA were pumped (100 μL min^{-1}) into the reaction chamber through a grounded stainless steel needle (100 μm bore) with a sheath flowing nebulizer $N_2(g)$ at a high gas velocity.

The ESI technique developed by Enami is distinct from a traditional one. As shown in Fig.A4-12, the nozzle, which solutions are injected throughout, is not connected to the outlet electrically. The liquid solution was smashed into small droplets (d = 1 mm) with $N_2(g)$ at 1 atm, 298 K, then pumped into the spraying chamber.

The observed mass spectrum represents species generated by heterogeneous processes in the interfacial layers (≤ 1 nm) of the liquid microjets. And this mechanism can be described as below in Fig.A4-13. The droplets (d = 1 mm) of liquid solution is injected into spraying chamber, and these initial droplets are flattened by the high-speed

nebulizer N_2 gas. As mentioned before, large organic compounds (species A in Fig.A4-13) have the affinity to the surfaces instead of staying in water bulks, so the thin-film on the bottom of a water bag has a relatively higher concentration of species A. In the same time, the anions concentrate on the surface of droplets as well, which are Cl^- in this experiment, since the negative mode of the electrospray ionization mass spectrometer was set, for the purpose of detecting the Cl^- adducted products. These rimmed water bags are dynamically unstable and break up into smaller secondary droplets ($d \leq 1$ μm). The initial droplets are uncharged, carrying equal positive and negative ions, because the nozzle is not linked to the outlet electrically. Whereas, the distributions of positive and negative ions are not even. The negative ions prefer to stay at outer layers of an initial droplet, which means that after the breakup of the initial droplets into smaller secondary droplets, the secondary droplets can be charged. Part of the kinetic energy of the moving nebulizer gas is converted into surface and electrostatic energy of the secondary droplets. The chamber is full of drying nitrogen gas at a temperature of 340 °C and the secondary droplets rapidly shrink via solvent evaporation by drying gas, eventually result in forming gas phase ions detected by the mass analyzer.

Ozone was produced by injecting $O_2(g)$ (>99.999%) through a commercial ozonizer (KSQ-050, Kotohira, Japan) and quantified via online UV−vis absorption spectrophotometry prior to entering the reaction chamber. The exposure values (E =[$O_3(g)$] × time) in the text are derived by considering [$O_3(g)$] measured by a UV−vis spectrometer (Agilent 8453) and a dilution factor by drying nitrogen gas.

Chemicals: β-caryophyllene (≥98.5%, Sigma-Aldrich), benzoic acid (≥99.5%, Sigma-Aldrich), α-terpinene (>90.0%, Tokyo Chemical Industry), γ-terpinene (>95.0%, Tokyo Chemical Industry), terpinolene (>85.0%, Tokyo Chemical Industry), (+)-limonene (>99.0%, Tokyo Chemical Industry), (−)-α-pinene (≥95%, Wako), cis-pinonic acid (≥98%, Sigma-Aldrich), octanoic acid (>97.0%, Wako), acetonitrile (≥99.8%, Wako), D_2O (>99.9 atom % D, Sigma-Aldrich), $H_2^{18}O$ (97%, Santa Cruz Biotechnologies), and NaCl (≥99.999%, Sigma-Aldrich) were used in the following works. All solutions were prepared in purified water (resistivity ≥18.2 MΩ cm at 298 K) from a Millipore Milli-Q

water purification system and used within a couple of days.

4.4 Criegee intermediate reacting with benzoic acid on gas-liquid interfaces[66]

Benzoic acid (BA, MW 122, Fig.4-4-1) is a dominant anthropogenic acid found in the particulate matter (PM) over polluted urban areas. For example, a recent field measurement study showed that BA concentrations in PM2.5 sampled over Beijing are extremely high, 1496 ng m^{-3} (average) in Pekin University and 1278 ng m^{-3} in Yufa.[76] These values exceed the concentrations of total diacids (~1010 ng m^{-3}) collected in the same campaign. The photochemical degradation of anthropogenic aromatic compounds and direct emission from traffic produce BA,[77] which is taken up into the liquid phase because of the hydrophilic C(O)OH moiety, followed by reactions with oxidants.

Since BA is amphiphilic[78] and relatively inert toward O$_3$ (in bulk water, k = 1.2 M^{-1} s^{-1}),[79] not only the oxidation of BA(aq) by OH radical(g)[80] but also CIs produced at the gas/liquid interface may control its fate. Previous molecular dynamics calculations, surface tension measurements, and surface-specific mass spectrometry revealed a moderate affinity of BA for aqueous surfaces.[81],[82] Thus, the identification of products from the reaction of CIs with BA at the gas-liquid interface has emerged as an important issue in the atmospheric chemistry of polluted urban air.[83],[84]

Fig.4-4-2 shows a negative ion mass spectrum of 1 mM β-C + 0.2 mM NaCl + 10 mM BA in W/AN (1:4 = vol/vol) solution microjets in the absence and presence of O$_3$(g). In the presence of O$_3$(g), distinguished peaks appear at m/z 305/307 and 409/411 (204 + 48 + 122 + 35/37 = 409/411), which are correspondingly Cl$^-$ adducted products of CI reacting with water and BA. Note that this observation means that 10 mM BA is able to compete with ~11 M bulk water for the CIs at aqueous organic surfaces. The present results imply that sesquiterpene initiated CIs generated in situ could potentially react with BA on the surface of aqueous organic particles found in a polluted area. Not only CIs from β-C but also those from other precursors (e.g., monoterpenes) may also react with BA, while the reactivity will depend on the structures[85],[38] and the

58

orientation of these reactants at the gas/liquid interface. Importantly, since these products contain a reactive hydroperoxide group, −OOH, they will trigger polymerization processes or decompose to form radical species.[86]–[90] Such a process may be linked to adverse health effects caused by inhalation of PM containing these species, inducing unexpected production of radical species in the lung epithelial lining fluid.[91], [92]

Fig.4-4-3 shows a negative ion mass spectrum of 1 mM β-C + 0.2 mM NaCl + 10 mM BA in D_2O/AN (1:4 = vol/vol) solution microjets in the presence of $O_3(g)$. The observation that the m/z = 305/307 product signals shift by +2 mass units into 307,309 signals in D_2O/AN is in accordance with the formation of hydroxy-hydroperoxides. The m/z = 409/411 product signals shift by +1 mass units into 410,412 signals in D_2O/AN, consistent with the formation of α-acyloxy-hydroperoxides having one exchangeable peroxide −OOH group.

Next, the relative reactivity of BA toward CIs at the gas/liquid interface was evaluated by comparison with other competitive reactants. Fig.4-4-4 shows the negative ion mass spectra of 1 mM β-C + 0.2 mM NaCl + 10 mM BA + 10 mM octanoic acid (OA) in W/AN (1:4 = vol/vol) solution microjets in the absence or presence of $O_3(g)$. The mass spectrum represents the competition between water vs BA vs OA toward CIs at the gas-liquid interface, and their reaction schemes are listed in Fig.4-4-5.

The peaks at m/z 431/433 correspond to the products of OA addition to CIs. The observation that signal intensities of m/z 431/433 are ~2 times larger than those of m/z 409/411 at [BA] = [OA] = 10 mM indicates that BA is less reactive toward CIs or less surface available. The reported $\Delta G_{acidity,BA}$ is 1394 kJ/mol, which is smaller (more acidic) than that of heptanoic acid (1418 kJ/mol),[93] suggesting that the BA + CIs reaction should have been more favorable. This unexpectedly small reactivity of BA toward CIs at the gas-liquid interface is correlated with the surface orientation of BA. A previous study revealed that the interfacial availability of benzoate (not benzoic acid, though) is smaller than heptanoate (by ~3.5 times at 1 mM).[82] Since π-electrons of the benzene ring of BA can interact with H atoms of water molecules,[94] the reactive C(O)OH group of BA will be located at deeper layers of the air-water interface than OA where

CIs are generated.

The ratio of the signal intensity of m/z 431 (from CIs + OA) to the signal intensity of m/z 409 (from CIs + BA) does not depend on the pH of the solution acidified by HCl in the range of $2.1 \leq pH \leq 3.4$ (Fig.4-4-6). This result implies that the extent of acid dissociation into carboxylate anions (pKa = 4.2 for BA vs 4.8 for OA in bulk water) at the gas-liquid interface of W/AN mixtures does not contribute to the preferable formation of the m/z 431 product over the m/z 409 product. Note that because of the lack of active −(O)OH, benzoate (BA$^-$) does not react with CIs, as suggested by the absence of signals at m/z 373, which would have arisen from 373 = 204 (β-C) + 48 (O$_3$) + 121 (BA$^-$), consistent with the cases of alkyl carboxylate and cis-pinonate.[43], [65]

Fig.4-4-7 shows mass spectral signals acquired from 1 mM β-C + 0.2 mM NaCl + 20 mM BA + 20 mM OA in W/AN (1:4 = vol/vol) microjets under the exposure of gaseous O$_3$/O$_2$ mixtures as functions of E(O$_3$).

All signals show nonzero initial slopes, implying that these species are indeed primary rather than secondary products generated within a few μs. CIs react comparably quickly with BA, OA, and interfacial (H$_2$O)$_n$, instead of diverse bulk concentration ratios: [BA]/[H$_2$O] = [OA]/[H$_2$O] = 20 mM/11 M $\approx$ 2 × 10^{-3} M at W/AN (1:4 = vol/vol). This observation will stem from (1) the low water density of aqueous organic surfaces, (2) the enrichment of amphiphilic BA and OA therein, and (3) the lower reactivity of sesquiterpene initiated CIs toward water molecules. A recent quantum mechanics/molecular mechanics (QM/MM) study showed that α-humulene CIs preferentially react with n-alkanoic acids as opposed to water at the air−W/AN interface because of the smaller energetic barriers.[95] These results demonstrate that sesquiterpene initiated CIs may bypass the reaction with water molecules and react with amphiphilic acids to form the larger-mass and lower-volatility products that potentially contribute to the growth of atmospheric particles.

Previous MD simulations showed a preferential orientation of benzoate at the air/water interface with the carboxylate moiety −C(O)O− projecting into the liquid phase and the aromatic ring being partly exposed toward the gas phase, and found that the decrease of surface tension by adding benzoate is moderate, indicating that this

carboxylate has a considerably smaller surface affinity than typical surfactants.[81] Another study revealed that the relative interfacial affinity follows the order: octanoate > n-heptanoate > cyclohexanecarboxylate > benzoate at the air/water interface.[82] The smallest availability of benzoate at the air/water interface among the C7 carboxylates is responsible for favorable π- electron···H atom bonding between the aromatic ring and water molecules.[94] The implication is that BA similarly stands up nearly perpendicularly to the surface, by pointing the hydrophilic −C(O)OH group into the liquid phase with full hydration, where it is hard for CIs to reach the moiety. It is generally assumed that carboxylic acids exist in the molecular form R−C(O)OH at the air/water interface, more than expected from bulk pKa values.[96]

The distribution and orientation of reactants determined their reactivity toward CI on gas-liquid interfaces, which has been discussed in this section. In the following part, reactivity of CIs in a same molecular weight but different conformers will be investigated.

4.5 Reactivity of monoterpenes initiated Criegee intermediates on gas-liquid surfaces[67]

The steric effect plays a significant role in Criegee chemistry on gas-liquid interfaces as discussed in the former section, which may lead to completely different reaction mechanisms compared to Criegee chemistry in gas phase.

In this study, several kinds of monoterpenes listed in Fig.4-5-1 are selected to explore the structure dependent Criegee chemistry on gas-liquid interfaces, since monoterpenes released from biogenic sources are major sources of CIs in the troposphere. Especially in the Sierra Nevada region of United States, about 80% of the CI source derives from monoterpenes and related compounds.

By employing the same setup used in the experiments described above, a mixture of [monoterpene + NaCl] in W/AN (1:4 = vol:vol) microjets is exposed to orthogonal gas-phase O_3/O_2 streams in the reaction chamber of a mass spectrometer flushed with $N_2(g)$ at 1 atm, 298 K.

Fig.4-5-2 shows negative ion mass spectra of (1 mM α-T + 0.2 mM NaCl) in W/AN (1:4 = vol:vol) solution microjets in the absence and presence of $O_3(g)$.

Intense peaks appear at m/z 237/239, which are assigned to the chloride-adduct of the hydroxy-hydroperoxide (HH) formed in the reaction of CIs with interfacial water (136 + 48 + 18 + 35/37). Note that HH signal intensities are > 40 times larger than those of other products, thereby implying that interfacial water is the dominant reactant for the CIs derived from α-terpinene under present conditions. The m/z 183 and 199 products are functional carboxylates detected as such, while the m/z 223/225 and 253/255 products are chloride-adducted of neutral species. (the reaction schemes are listed in Fig.4-5-3 to 4-5-5)

Isotopic labeling studies provided confirmation of the functional assignments. Fig.4-5-6 and Fig.4-5-7 show negative ion mass spectra of 1 mM α-T + 0.2 mM NaCl in D_2O/AN (1:4 = vol:vol) and in $H_2^{18}O$/AN (1:4) solution microjets, respectively, in the presence of $O_3(g)$.

The observation that the m/z 237/239 product signals shift by +2 mass units into 239/241 signals in D_2O/AN and $H_2^{18}O$/AN is in agreement with the involvement of water in HH formation from α-T CIs. These experiments show that labile HH from monoterpenes can be detected by mass spectrometry as chloride-adducts, as it was in the case of sesquiterpenes. These findings are made more remarkable by the fact that mass-spectrometric detection of neutral organic hydroperoxides has been experimentally challenging until now. Importantly, since HH contain thermally and photochemically reactive hydroperoxide groups -OOH, they may trigger further polymerization processes by decomposing to form radical species under ambient conditions (i.e., at much longer time scales than our experiments).[86], [89], [90] The reactivity of hydroxy hydroperoxides also implies that the inhalation of particulate matter containing such species could trigger the generation of reactive oxygen species (ROS) in the lung epithelial lining fluid.[92]

The m/z 183 product signal does not shift in D_2O/AN (Fig.4-5-6), but it does in $H_2^{18}O$/AN leading to the formation of a m/z 185 product (Fig.4-5-7). This is strong evidence that the m/z 183 is a functional carboxylate (FC) containing a keto-group ,

which can exchange O-atoms with the solvent via: $-C(=O)O- + H_2^{18}O \leftrightarrow -C(=^{18}O)O-$ $+ H_2O$.[97] It is well known that the gas-phase ozonolysis of α-P produces cis-pinonic acid (MW 184) as a major product,[98] suggesting that a similar mechanism could operate both in the gas-phase and at the air/liquid interface. The interfacial ozonolysis of β-caryophyllene and α-humulene produce FCs containing keto-groups at m/z = M + 48 - 1, suggesting that the isomerization of CIs into corresponding FC is a common process in the interfacial ozonolysis of terpenes. The fact that, similarly to the case of the m/z 183 product, the m/z 199 (= 183 + 16) product does not shift by D_2O/AN but does it in $H_2^{18}O$/AN solvent (Figs.4-5-6 and 4-5-7) suggests it is a FC containing an additional O-atom.

In contrast with the m/z 183 and 199 product species, the m/z 223/225 product shifts by +2 Da both in D_2O/AN and $H_2^{18}O$/AN solvents. The m/z 253/255 product shifts by +3 and +2 Da in D_2O/AN and $H_2^{18}O$/AN solvents, respectively. The fact that both products appear at larger O_3-exposures (see below), strongly suggests that these are secondary products generated by more extensive ozonolysis. The m/z 223/225 product could be assigned to a chloride-adduct of C9 ester hydroperoxides, generated from 1,6-H-atom migration in the participating CI,[99] followed by further ozonolysis and hydration. The proposed structure, which contains two exchangeable H(D)-atoms and incorporates one ^{18}O-atom, is consistent with the observed mass spectra in D_2O/AN and $H_2^{18}O$/AN solvents (Fig.4-5-6 and 4-5-7). The m/z 253/255 product could be formed by further oxidation of HH, that was tentatively assigned to the chloride-adduct of a (HH + O) species (m/z 237/239 + 16), most likely containing an aldehydic-group and an epoxide-group.[100]

Fig.4-5-8 shows negative ion mass spectra of 1 mM γ-T, TL, D-L, or α-P + 0.2 mM NaCl in W/AN (1:4 = vol:vol) solution microjets in the absence and presence of O_3(g). And relative HH signal intensities for the different monoterpenes under the same experimental conditions are shown in Fig.4-5-9.

The observed relative yields of HH production are in the order of: α -T (1.00) >> D-L (0.18) > γ-T (0.11) ~ TL (0.10) >> α-P (0.01). Note that HH production involves at least two factors: (1) the rate of monoterpene ozonolysis, and (2) the relative reaction rates of

CIs isomerization/decomposition vs. reaction with water, at the gas-liquid interface. By comparison, the reported gas-phase rate constants of ozonolysis are: $k(\alpha\text{-}T+O_3) \approx 2.1 \times 10^{-14}$, $k(\gamma\text{-}T+O_3) \approx 1 \times 10^{-16}$, $k(TL+O_3) \approx 1.9 \times 10^{-15}$, $k(D\text{-}L+O_3) \approx 2 \times 10^{-16}$, $k(\alpha\text{-}P+O_3) \approx 8.4 \times 10^{-16}$ cm^3 molecule^{-1} s^{-1} as listed in Table 1-1-1.[6] A caveat is in order at this point. The largest yield of HH in the case of α-T correlates with its large rate constant for gas-phase ozonolysis, a correlation that does not extend to the other monoterpenes. The unexpectedly large yield of HH for D-L is worth noting, given that D-L is one of the most abundant monoterpenes in the atmosphere, whereas the HH yield for T-L is far below anticipation, since the rate constant of T-L reacting with O_3 is about 10 times of that for D-L.

The orientations of these 5 kinds of monoterpenes may lead to this disagreement, which regulate their reactivity toward O_3 on gas-liquid interfaces. The monoterpenes prefer to stay at outermost layers, because of their hydrophobicity, and the interactions of π-electrons on C_6 rings with H_2O molecules may determine their orientations on gas-liquid interfaces. Possible orientations of 5 monoterpenes on the gas-liquid interface are presented in Fig.4-5-10, based on the experimental results. In the gas phase, the reactivity of the endo-cyclic double bond is higher than the exo-cyclic one for D-L, while for T-L, the exo-cyclic double bond is thought to be more reactive than the endo-cyclic one. As shown in Fig.4-5-10, the reactive exo-cyclic double bond of T-L could be buried in the liquid side, which prohibited the reactivity of T-L toward O_3 on gas-liquid interfaces. Molecular dynamics calculations may help to understand the distributions and orientations of monoterpenes and provide a more specific comprehension of how these characteristics affect Criegee chemistry on gas-liquid interfaces. As shown below, the dependence of reactivity on the structure of monoterpene CIs is manifested not only toward water molecules but also toward organic acids.

Cis-pinonic acid (CPA) is a major product of the atmospheric oxidation of monoterpenes, which has been introduced in former chapters as an efficient scavenger for CI on gas-liquid interfaces. Fig.4-5-11 shows negative ion mass spectra of 1 mM α-T vs. 1 mM γ-T + 0.2 mM NaCl + 1 mM cis-pinonic acid (CPA) in W/AN (1:4 =

vol:vol) solution microjets in the absence and presence of $O_3(g)$. The signals at m/z 183, 219/221 and 389 appearing in the absence of $O_3(g)$ are assigned to CPA^-, $(CPA)Cl^-$ and $Na(CPA)_2^-$, respectively. In Fig.4-5-11(A), new mass signals at m/z 403/405 in addition to those at m/z 237/239 appear during the interfacial ozonolysis of α-T in the presence of CPA. The m/z 403/405 product is assigned to chloride-adduct of acyloxy-hydroperoxides (C_{20} ester hydroperoxides) generated by CPA addition to α-T CIs at the gas-liquid interface: m/z = 136 (α-T) + 48 (O_3) + CPA (184) + Cl^- (35/37) = 403/405.

Remarkably, the ozonolysis of γ-T with CPA under the same conditions does not give rise to m/z 403/405 signals (Fig.4-5-11(B)). The same observation applies to the ozonolysis of TL, D-L and α-P with 1 mM CPA (Fig.4-5-12). The results showed that only α-T CIs are scavenged by CPA on aqueous surfaces, indicating the fact that the reactivity of CIs is critically influence by the structures and, possibly, by the orientations of CIs at the gas-liquid interface.[38]

The reaction of monoterpene CIs with octanoic acid (OA), a surface-active *n*-alkanoic acid, was also investigated. Negative ion mass spectra of 1 mM α-T + 0.2 mM NaCl + 5 mM OA in W/AN (1:4 = vol:vol) solution microjets in the absence or presence of $O_3(g)$ (Fig.4-5-13) shows the formation of the m/z 363/365 product, C_{18} ester hydroperoxides from CIs + OA, in contrast with the absence of the corresponding product for other monoterpenes (Fig.4-5-14). Again, only α-T CIs react with OA on aqueous surfaces, while other monoterpene CIs are inert toward OA.

These results imply the reactions of γ-T, TL, D-L and α-P monoterpene CIs with these acids are much slower than those with water molecules and/or their unimolecular isomerizations/decompositions under the present condition. Another possibility to explain structure dependent reactivity of CIs may lie in the conjugated double bonds of α-T, which is an exclusive structure among the selected 5 kinds of monoterpenes. As mentioned before, the process of CI reacting with an organic acid starts at the transition of H atom, from -COOH to terminal O of CI, then -COO attaches to the C atom next to -OO, as illustrated in Fig.4-5-15. A comparison of CIs with or without conjugated double bonds is depicted in Fig.4-5-16, in which α-T initiated CI has such a structure

that is more reactive, because the delocalized π-electrons on the conjugated double bonds may facilitate the addition of an organic acid.

Although structural effects on the reactivity of small ($C_{\leq 3}$) CIs in the gas-phase are well documented,[85], [101], [102] there is little experimental information on the reactivity of the larger, more atmospherically relevant CIs generated from monoterpenes. This study experimentally demonstrates the critical effects of subtle structural and orientational differences on the reactivity of large CIs at the gas-liquid interface.

In this chapter, researches on the reactivity of benzoic acid toward CI, and the molecular structure dependent reactivity of CIs on gas-liquid interfaces are performed by using an electrospray ionization technique combined with a quadrupole mass analyzer. The reactivity of CI towards benzoic acid and the reactivity of different monoterpenes towards O_3 on gas-liquid interfaces indicate that the orientation of organic compounds on gas-liquid interfaces plays a significant role in Criegee chemistry. Different monoterpenes initiated CIs show distinguished reactivity towards CPA/OA on gas-liquid interfaces, which imply that reactivity of CIs is highly structure dependent.

Smaller m/z ions get affected by AC fields easily
and trapped on positive rods

\+

A bunch of ions

Larger m/z ions pass
through and get detected,
since they can hardly be
affected by AC fields

\+
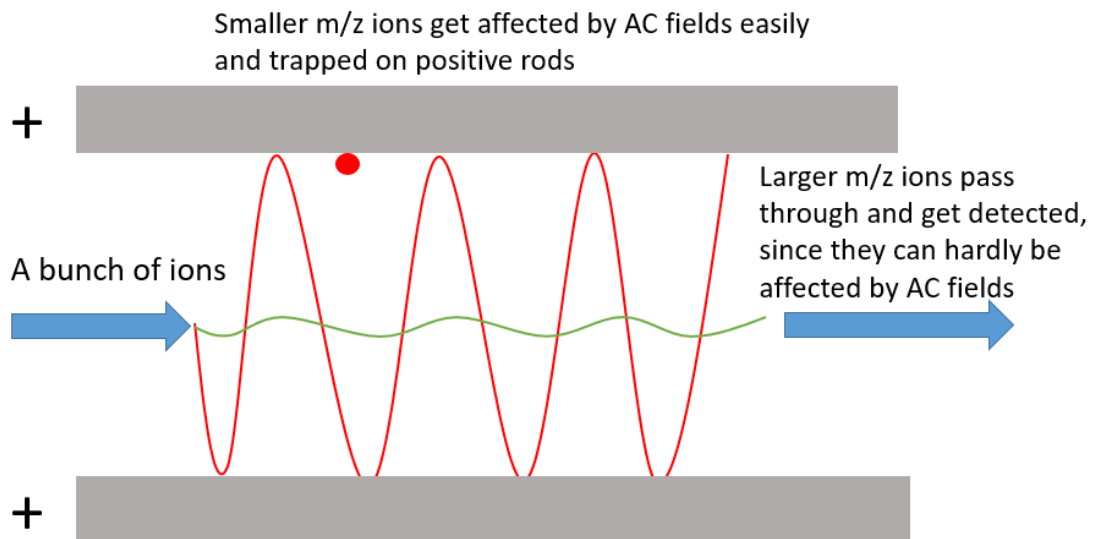
Fig.4-2-1 Schematic representation of movement of positive ions controlled by positive rods. (red line: trajectory of smaller m/z ions, green line: trajectory of larger m/z ions)
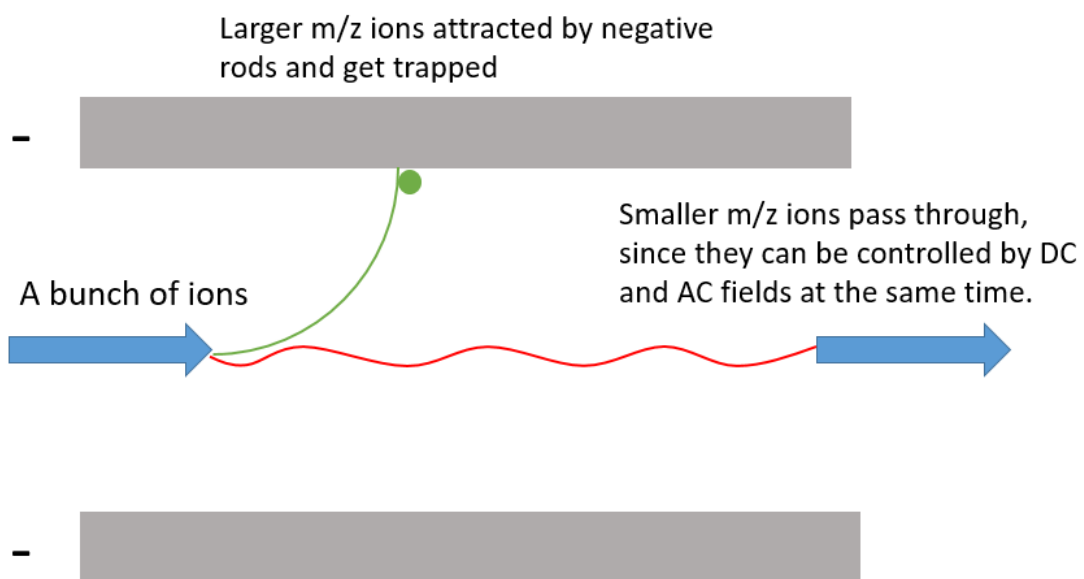
Fig.4-2-2 Schematic representation of movement of positive ions controlled by negative rods. (red line: trajectory of smaller m/z ions, green line: trajectory of larger m/z ions)
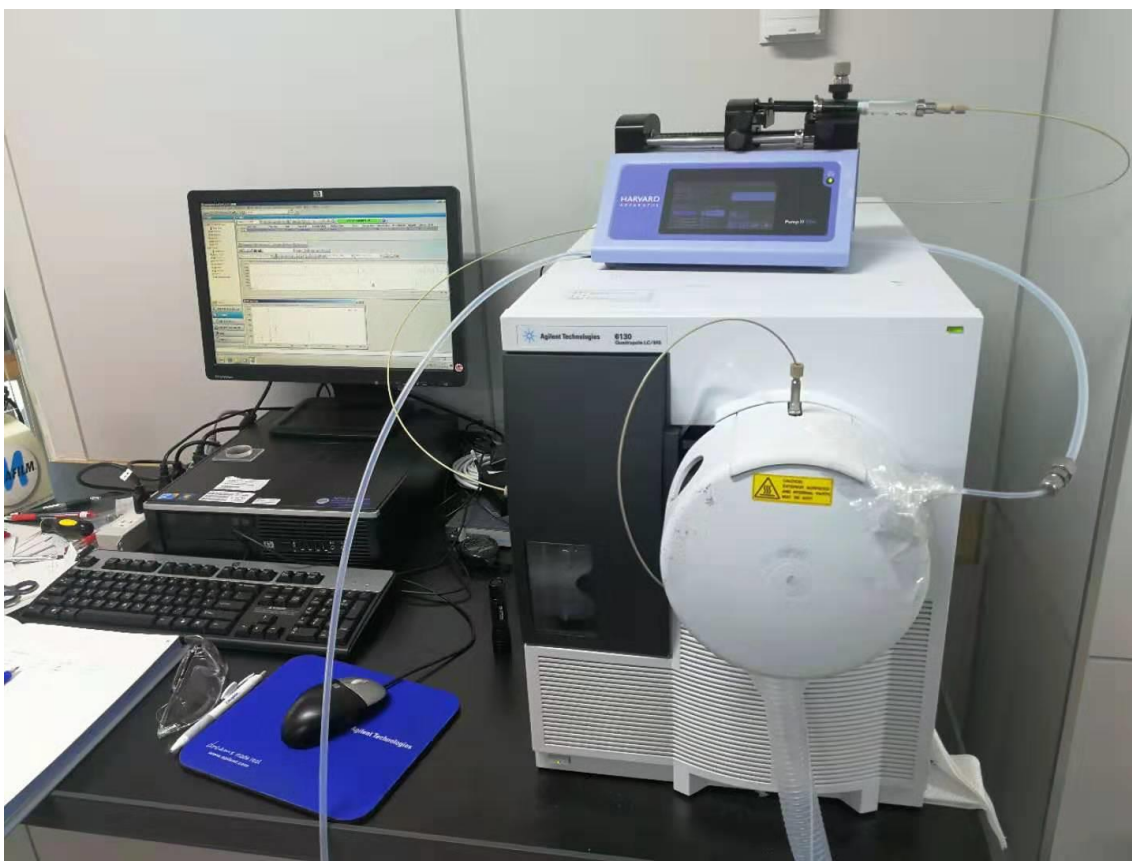
Fig.4-3-1 Picture of the electrospray mass spectrometer applied in the research on the reactivity of CI on gas-liquid interfaces (Agilent 6130).
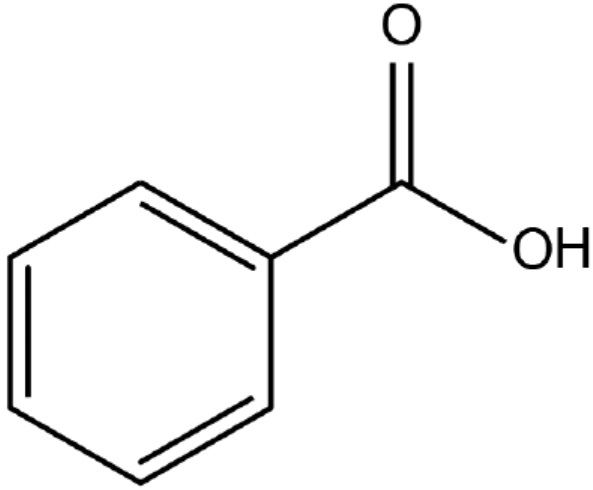
Fig.4-4-1 Molecular structure of benzoic acid (BA).
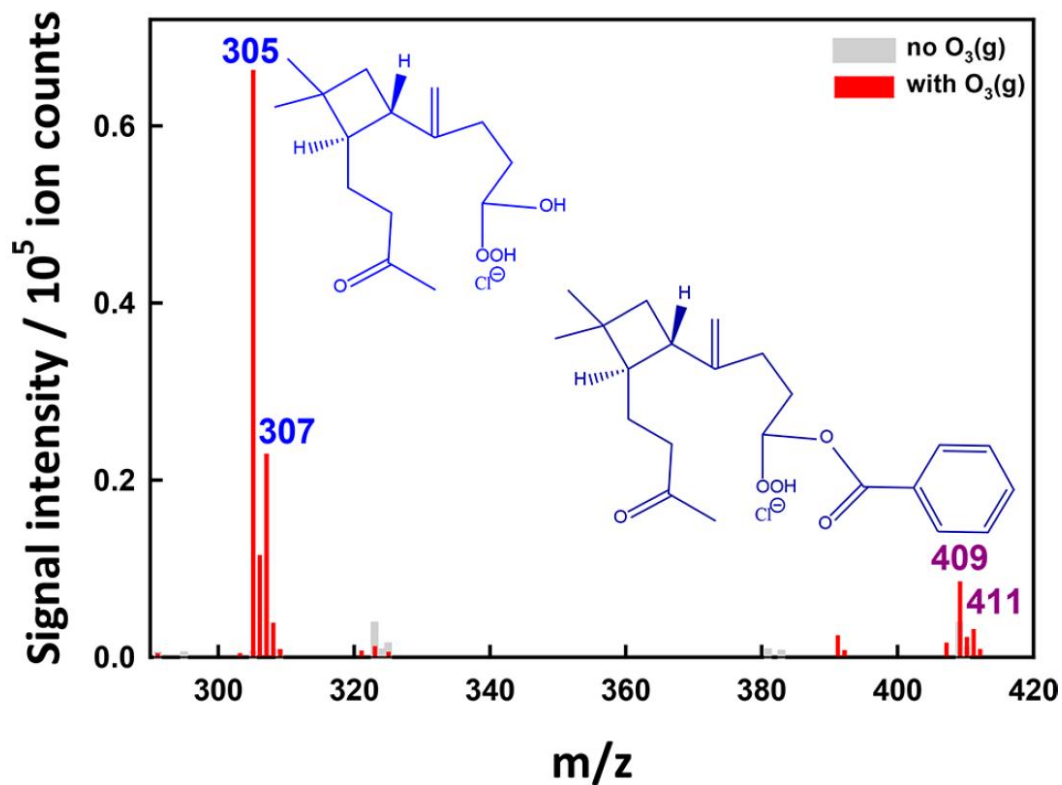
Fig.4-4-2 Negative ion mass spectra of 1 mM β-caryophyllene + 0.2 mM NaCl + 10 mM benzoic acid in W/AN (1:4 = vol:vol) solution microjets (gray), or those exposed to O_3(g) (red, $E = 9.5 \times 10^{10}$ molecules cm^{-3} s) at 1 atm and 298 K. The m/z 305/307 and 409/411 signals correspond to chloride-adducts of a-hydroxy-hydroperoxides and a-acyloxy-hydroperoxides (C_{22} ester species), respectively.
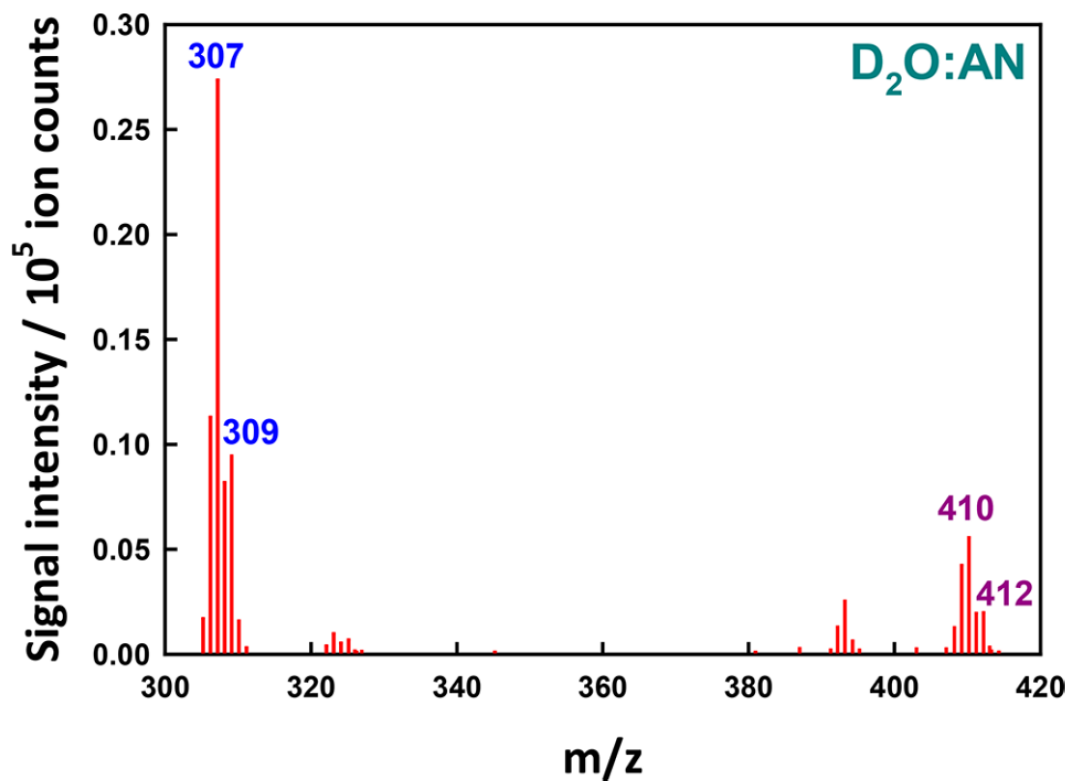
Fig.4-4-3 Negative ion mass spectra of 1 mM β-caryophyllene + 0.2 mM NaCl + 10 mM benzoic acid in D_2O/AN (1:4=vol:vol) solution microjets exposed to O_3(g) (E = 3.2 × 10^{11} molecules cm^{-3} s) at 1 atm and 298 K.
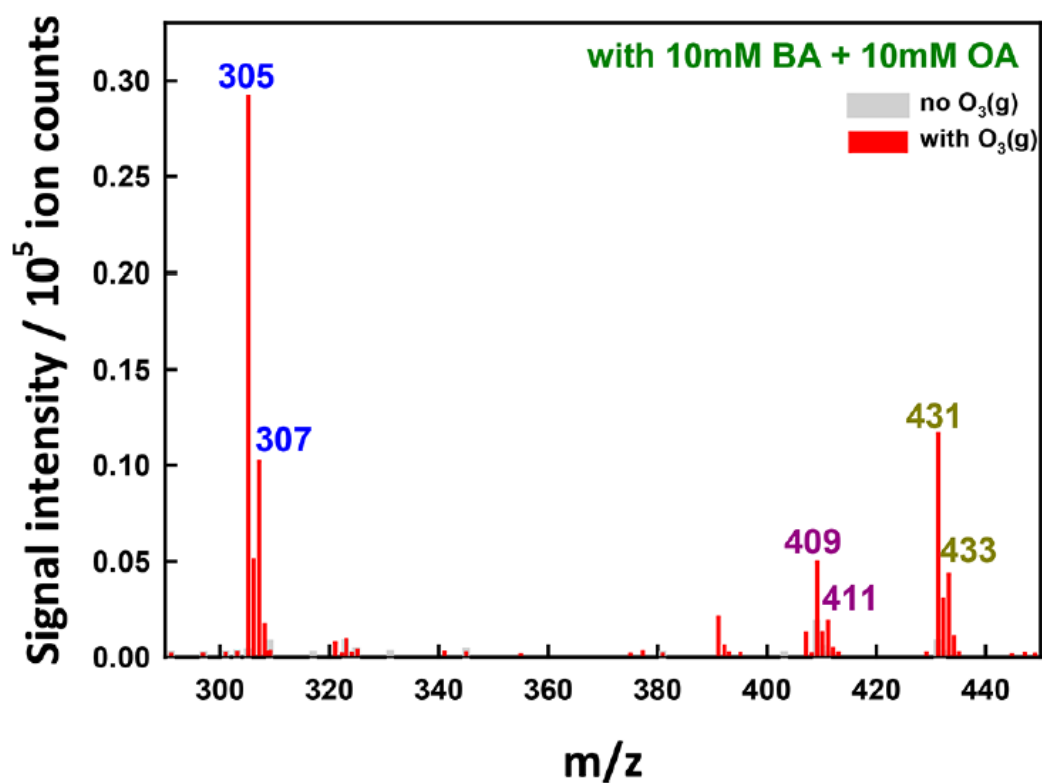
Fig.4-4-4 Negative ion mass spectra of 1 mM β-caryophyllene + 0.2 mM NaCl + 10 mM benzoic acid + 10 mM octanoic acid in W/AN (1:4 = vol:vol) solution microjets (gray), or those exposed to O_3(g) (red, $E = 3.3 \times 10^{11}$ molecules cm^{-3} s) at 1 atm and 298 K.
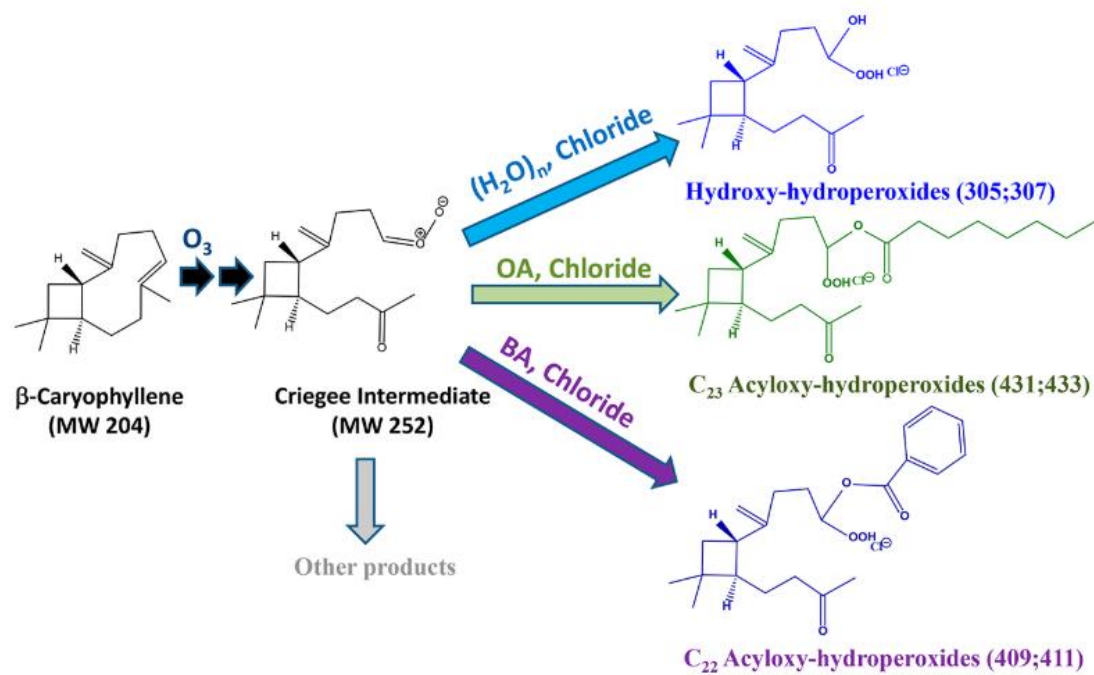
Fig. 4-4-5 Mechanism of ozonolysis of β-caryophyllene and subsequent reactions of CI with water, benzoic acid and octanoic acid on gas-liquid interfaces.
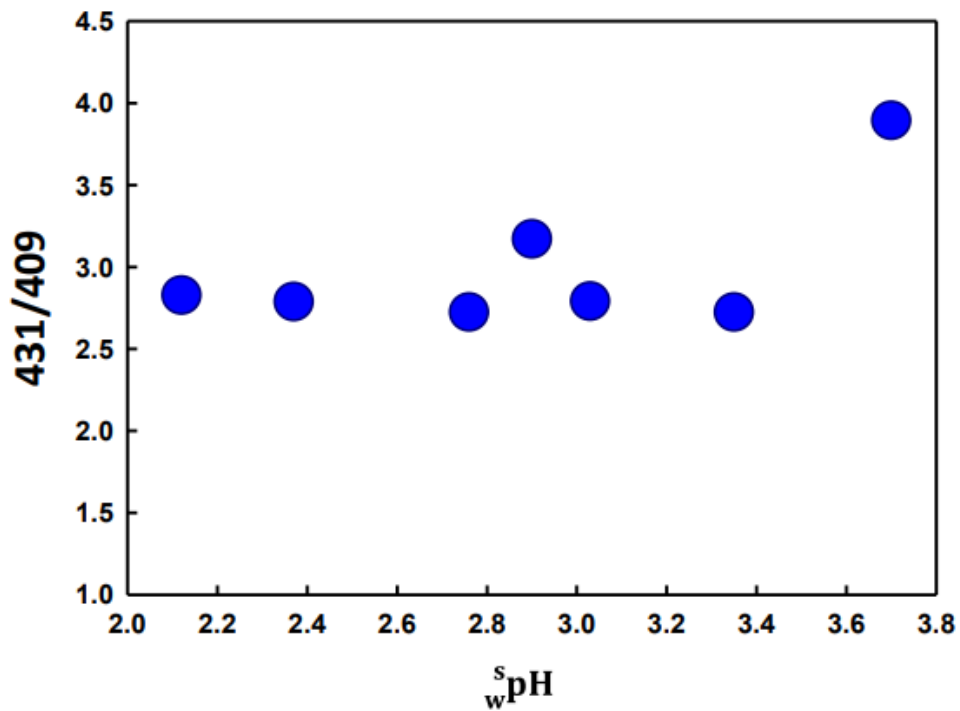
Fig.4-4-6 Ratios of signal intensity of m/z 431 to 409 from 1 mM β-C + 0.2 mM NaCl + 10 mM BA + 10 mM OA in W/AN (1:4 = vol:vol) microjets exposed to $O_3(g)$ ($E = 3.1 \times 10^{11}$ molecules cm^{-3} s) as a function of bulk $_w^s$pH measured by the pH meter before experiments.
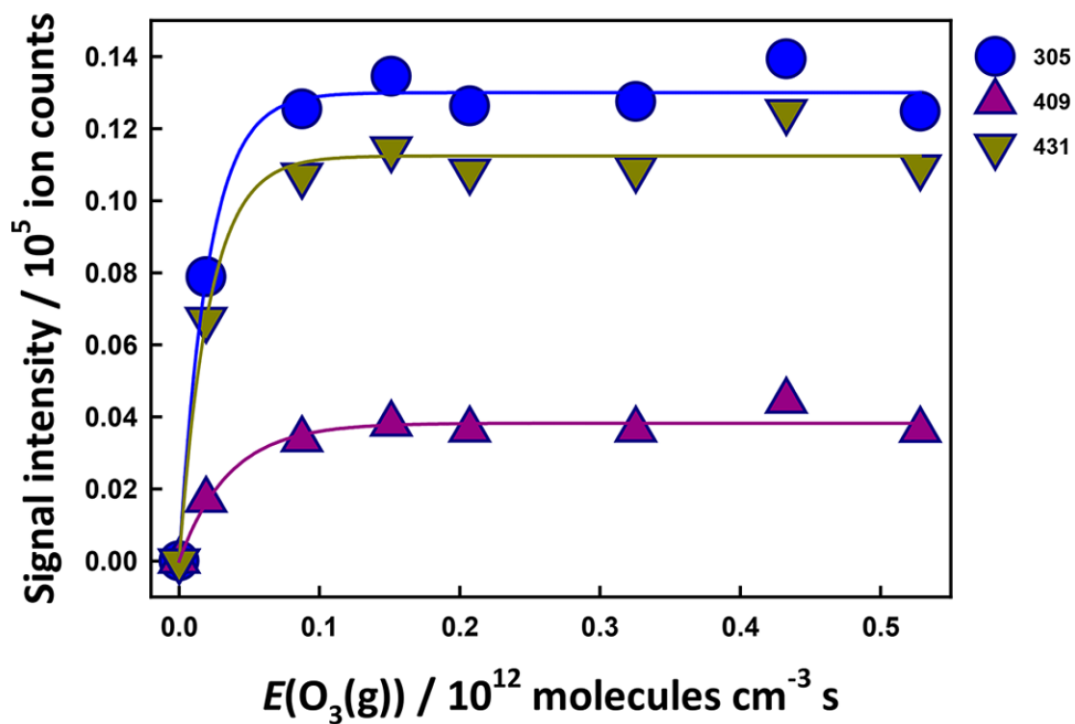
Fig.4-4-7 Products mass spectral signal intensities from 1 mM β-caryophyllene + 0.2 mM NaCl + 20 mM benzoic acid + 20 mM octanoic acid in W/AN (1:4 = vol:vol) solution microjets exposed to $O_3(g)$ as functions of $O_3(g)$ exposure (in 10^{12} molecules cm^{-3} s). The lines are regression curves fitted with single-exponential growth functions.
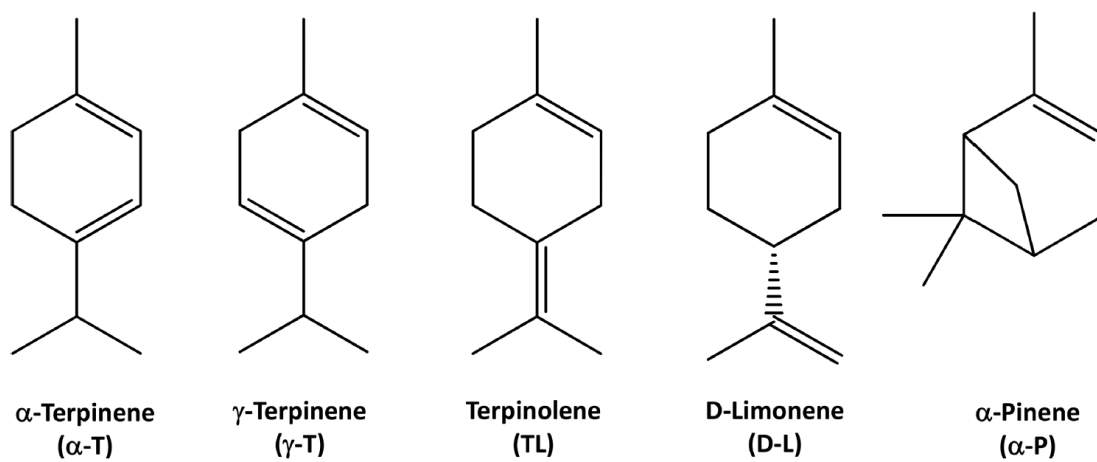
Fig.4-5-1 Chemical structures of monoterpenes ($C_{10}H_{16}$, MW = 136.23) used in this study.
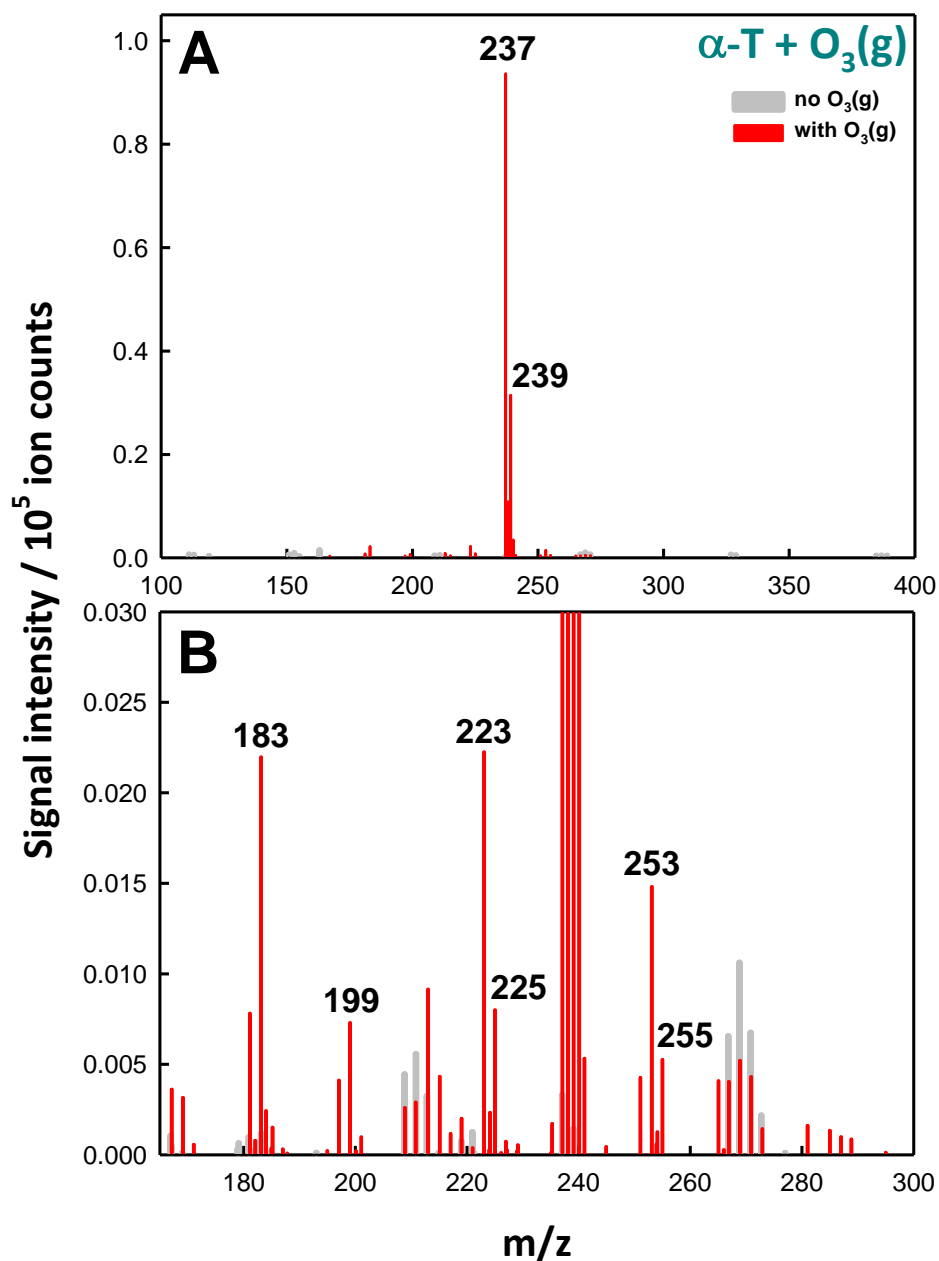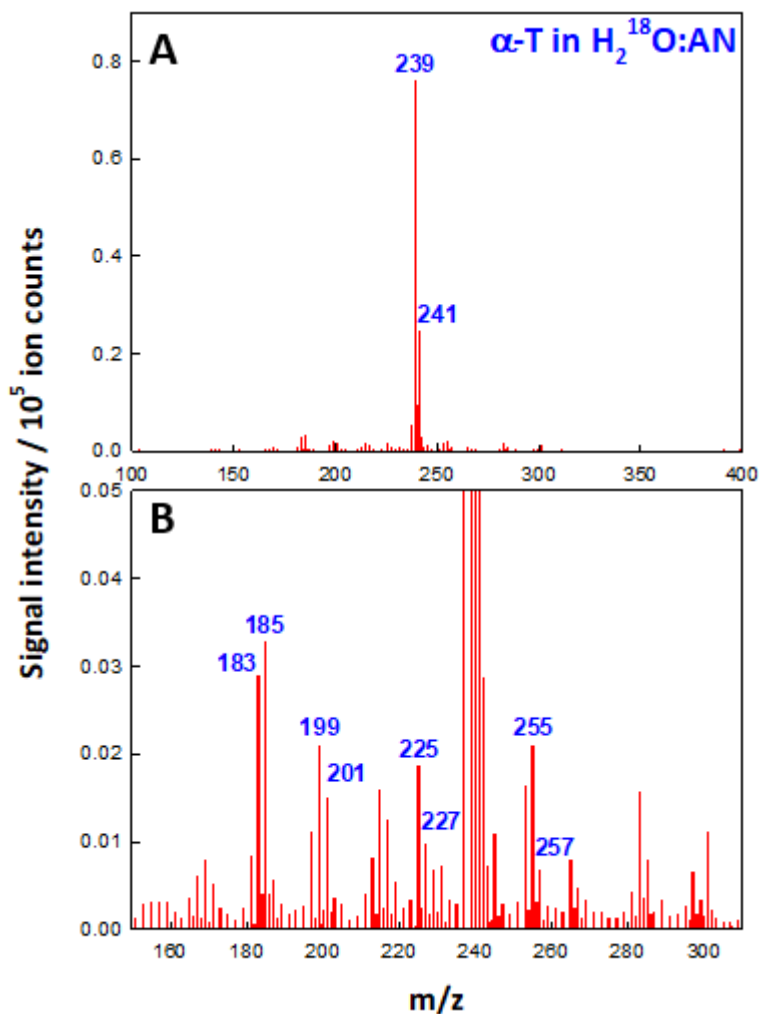
Fig.4-5-2 (A) Negative ion mass spectra of 1 mM α-terpinene + 0.2 mM NaCl in W/AN (1:4 = vol:vol) solution microjets (gray), and during exposure to $O_3(g)$ (red, $E = 4.3 \times 10^{11}$ molecules cm^{-3} s) at 1 atm and 298 K. The m/z 237/239 signals correspond to chloride-adducts of a-hydroxy-hydroperoxides. (B) Zooming-in on minor products.
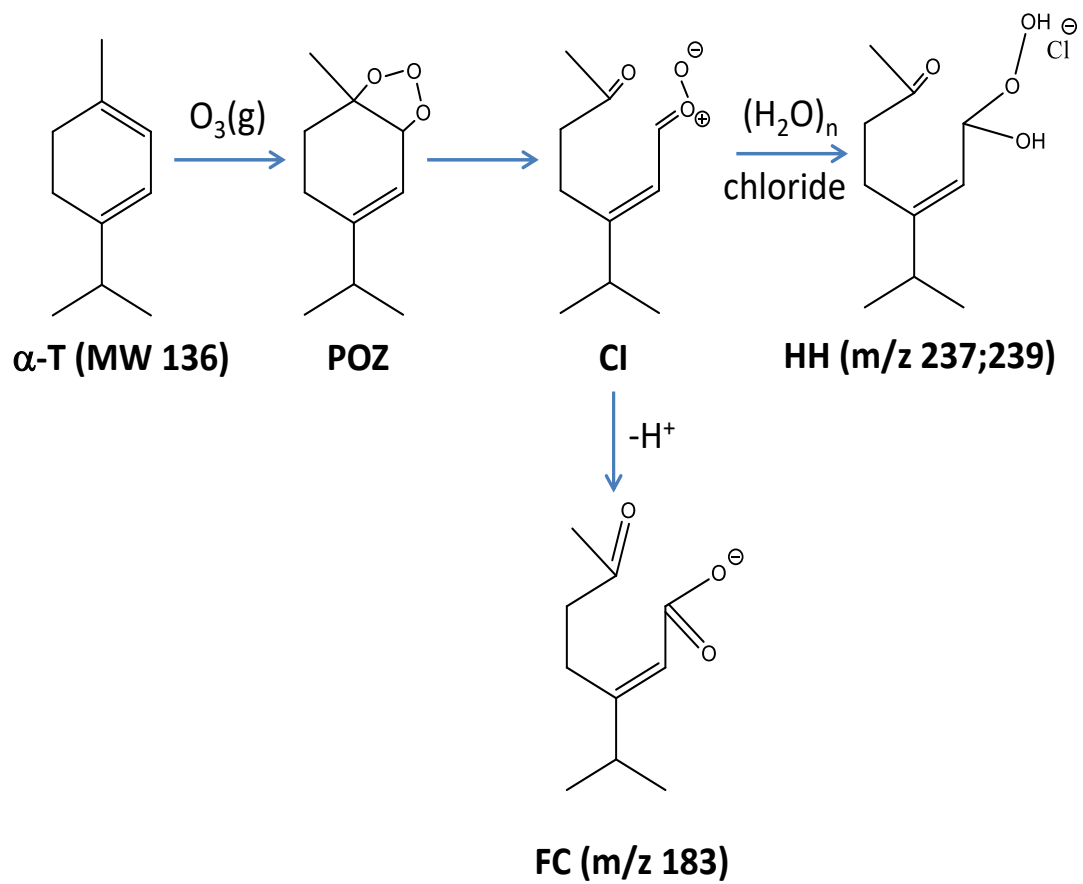
Fig.4-5-3 Reaction Scheme of α-Terpinene CI at the gas-liquid interface (major products).
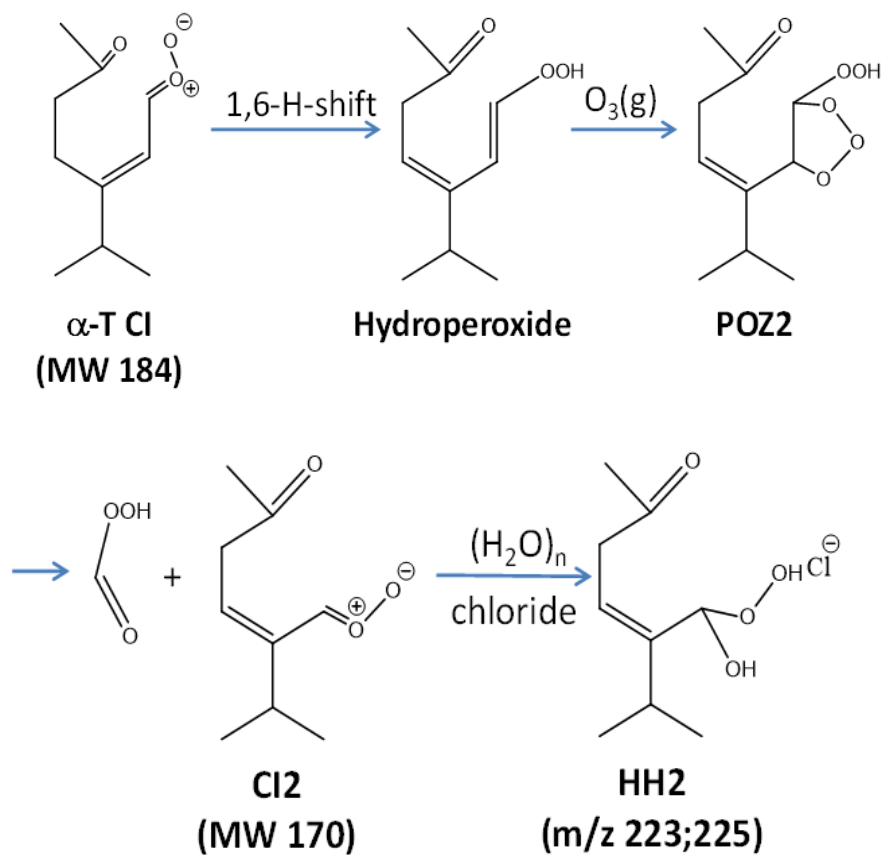
Fig.4-5-4 Scheme for generation of the m/z 223/225 product during ozonolysis of α-terpinene at the gas-liquid interface.
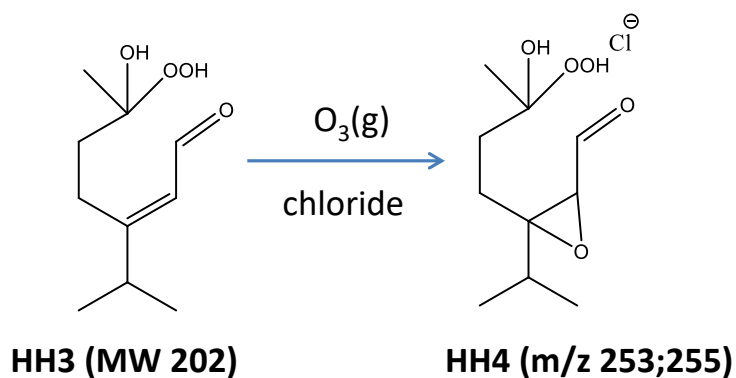
Fig.4-5-5 Scheme for generation of the m/z 253/255 product during ozonolysis of α-terpinene at the gas-liquid interface.
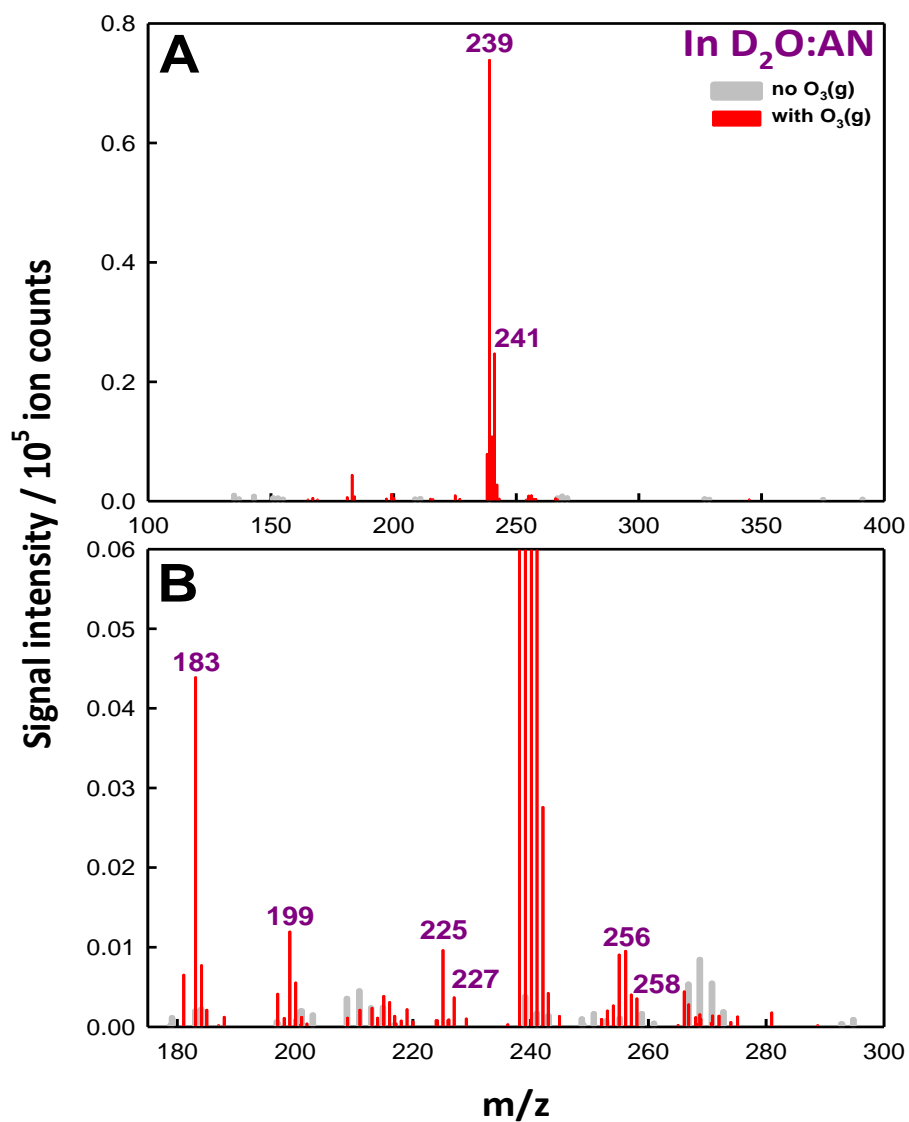
Fig.4-5-6 (A) Negative ion mass spectra of 1 mM α-terpinene + 0.2 mM NaCl in D$_2$O/AN (1:4=vol:vol) solution microjets (gray), or those exposed to O$_3$(g) (red, $E = 3.2 \times 10^{11}$ molecules cm^{-3} s) at 1 atm and 298 K. (B) Zooming-in on the minor products.

Fig.4-5-7 (A) Negative ion mass spectrum of 1 mM α-terpinene + 0.2 mM NaCl in $H_2^{18}O$/AN (1:4 = vol:vol) solution microjets exposed to $O_3(g)$ ($E = 5.1 \times 10^{11}$ molecules cm^{-3} s) at 1 atm and 298 K. The m/z 239/241 signals correspond to chloride-adducts of α-hydroxy-hydroperoxides from the reaction of CIs with $H_2^{18}O$. (B) Zooming-in on the minor products.
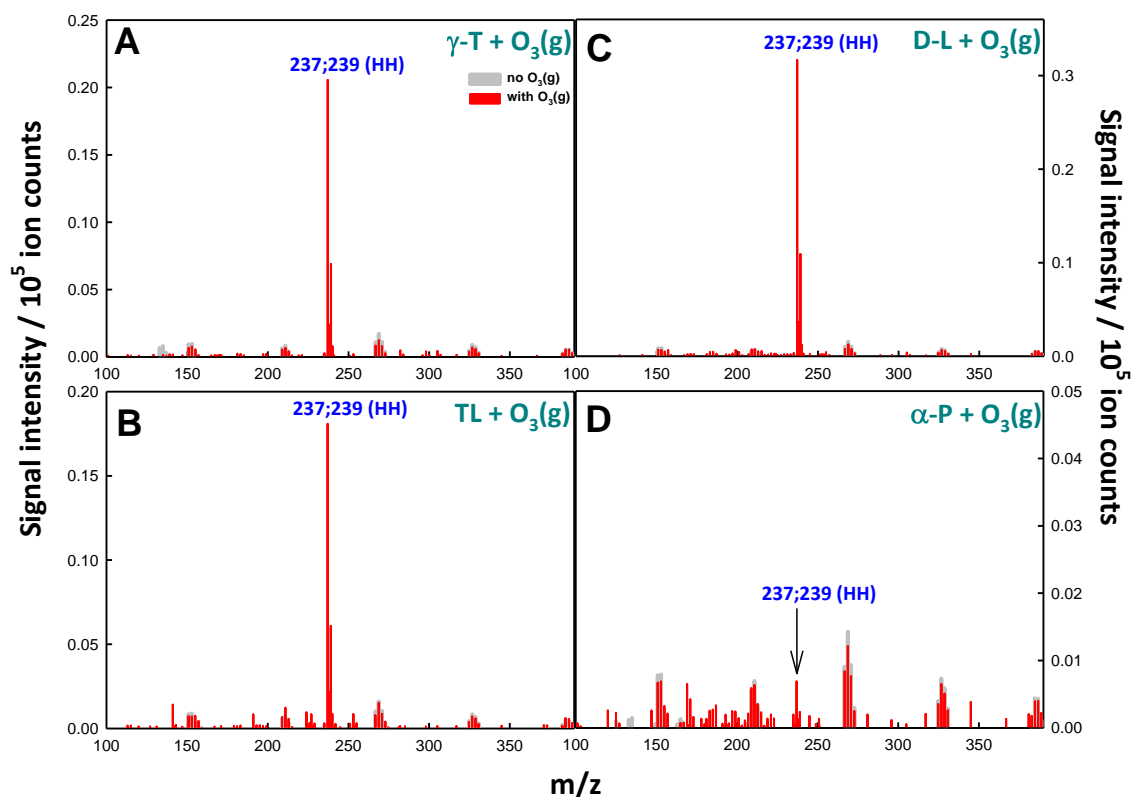
Fig.4-5-8 Negative ion mass spectra of 1 mM γ-terpinene (A), terpinolene (B), D-limonene (C) or α-pinene (D) + 0.2 mM NaCl in W/AN (1:4 = vol:vol) solution microjets (gray), or those exposed to $O_3(g)$ (red, $E \approx 5.2 \times 10^{11}$ molecules cm^{-3} s) at 1 atm and 298 K. The m/z 237/239 signals correspond to chloride-adducts of a-hydroxy-hydroperoxides (HH).
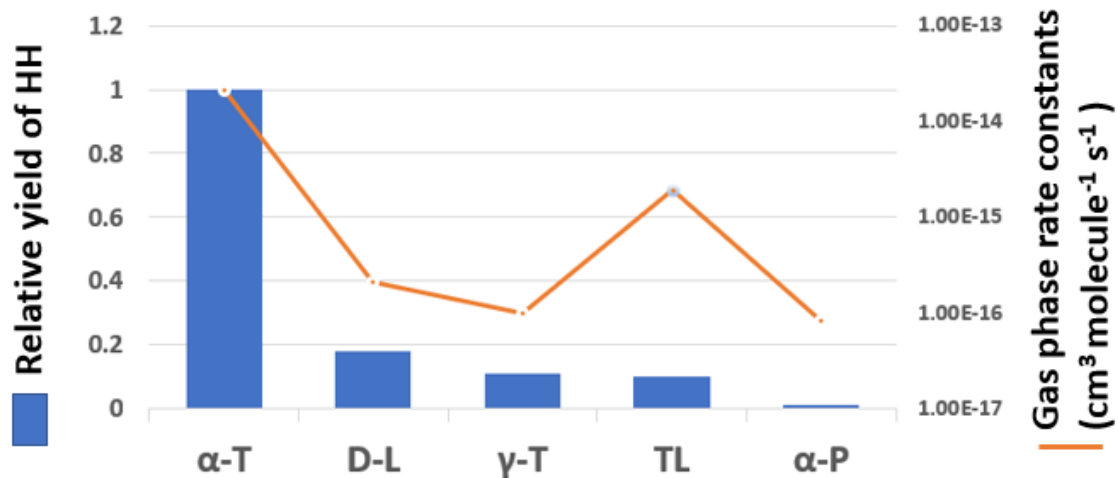
Fig.4-5-9 Relative yields of hydroxy-hydroperoxides (HH, m/z 237/239) from 1 mM α-terpinene, γ-terpinene, terpinolene, D-limonene, or α-pinene + 0.2 mM NaCl in W/AN (1:4 = vol:vol) solution microjets exposed to $O_3(g)$ ($E \approx 5.2 \times 10^{11}$ molecules cm^{-3} s) at 1 atm and 298 K, in contrast with their gas phase rate constants.
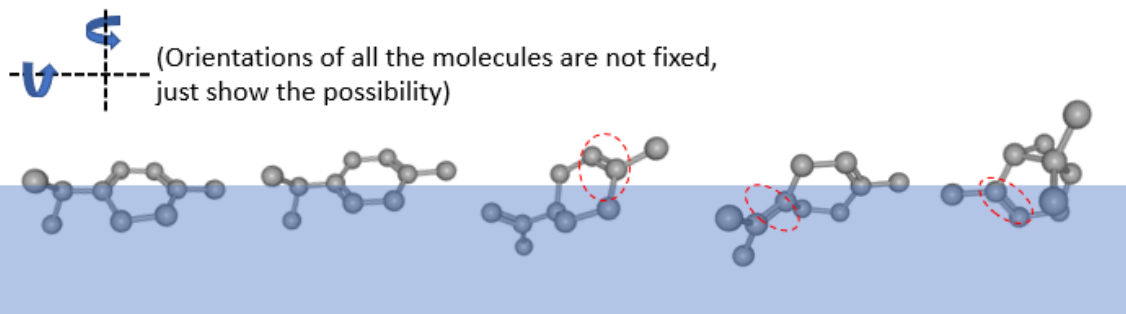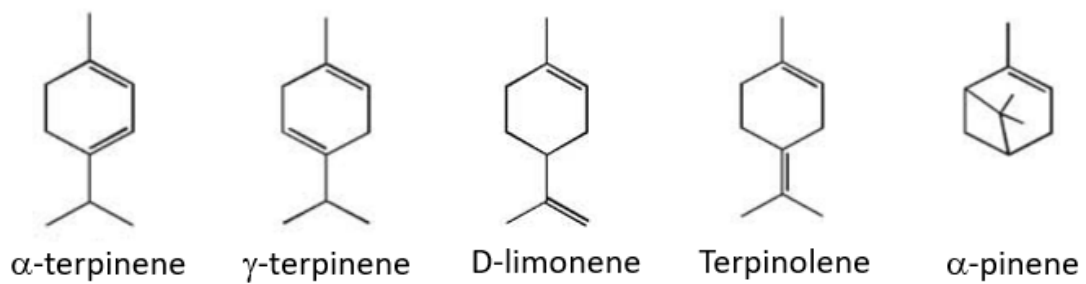
Fig.4-5-10 Schematic representation of possible orientations of selected monoterpenes on gas-liquid interface.
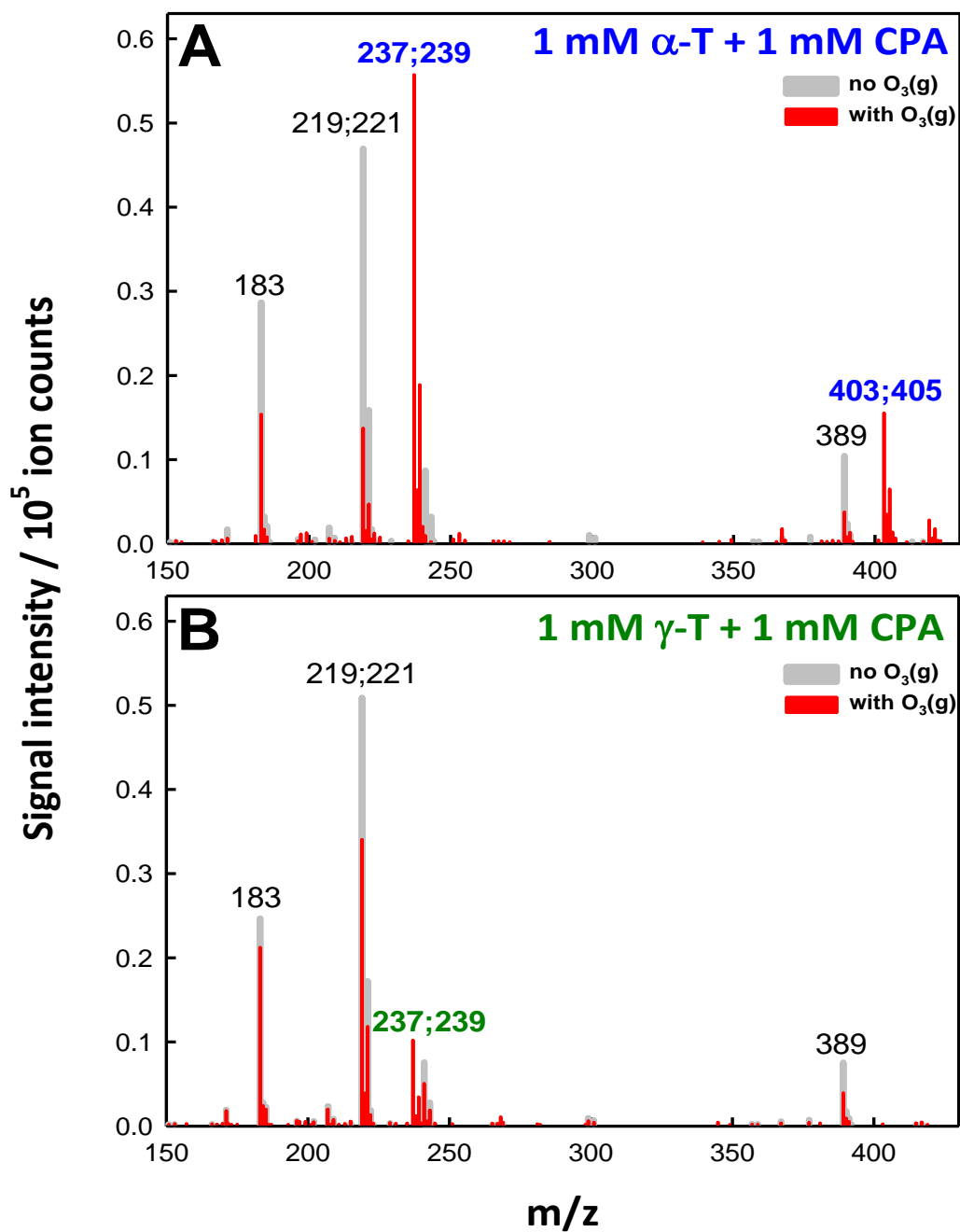
Fig.4-5-11 Negative ion mass spectrum of 1 mM α-terpinene (A) or 1 mM γ-terpinene (B) + 0.2 mM NaCl + 1 mM cis-pinonic acid in W/AN (1:4 = vol:vol) solution microjets (gray), or those exposed to $O_3(g)$ (red, $E \approx 5.3 \times 10^{11}$ molecules cm^{-3} s) at 1 atm and 298 K.
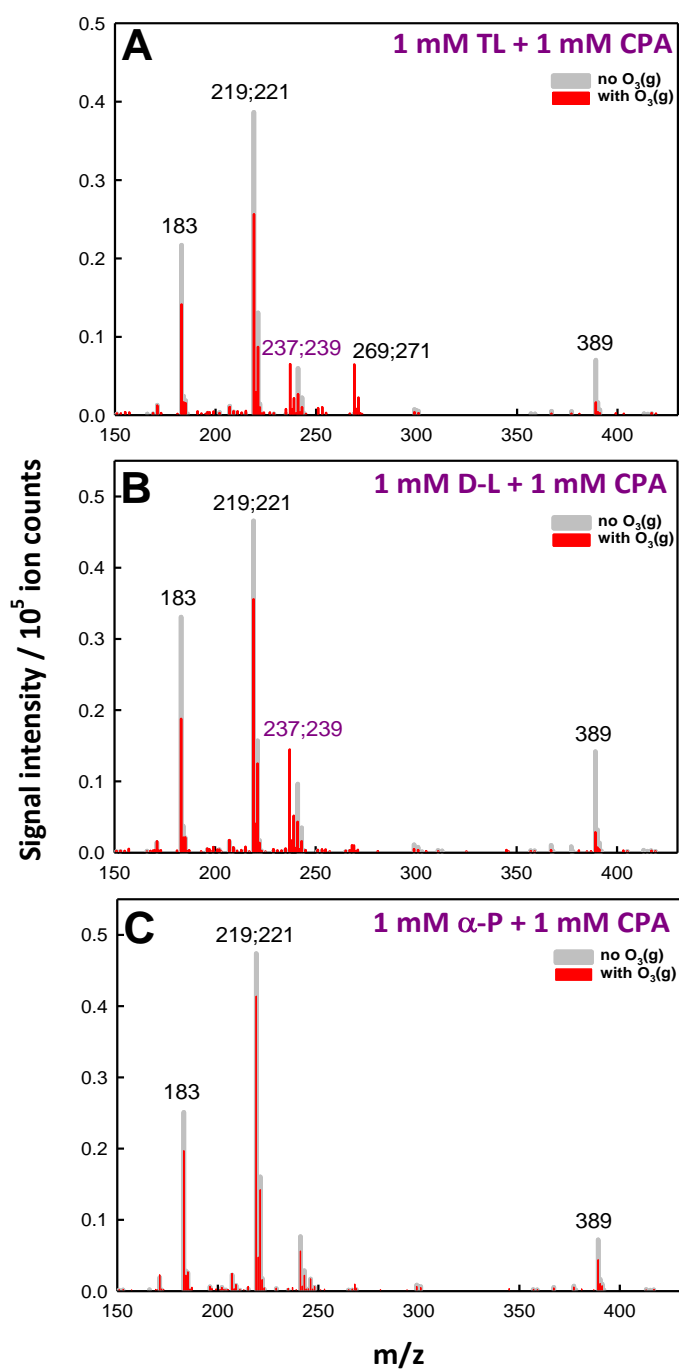
Fig.4-5-12 Negative ion mass spectra of 1 mM terpinolene (A), d-limonene (B) or α-pinene (C) + 0.2 mM NaCl + 1 mM cis-pinonic acid in W/AN (1:4 = vol:vol) solution microjets (gray), or those exposed to $O_3(g)$ (red, $E \approx 5.1 \times 10^{11}$ molecules cm^{-3} s) at 1 atm and 298 K. Note the absence of mass signals at m/z 403;405 (from CIs + CPA) in the presence of $O_3(g)$.
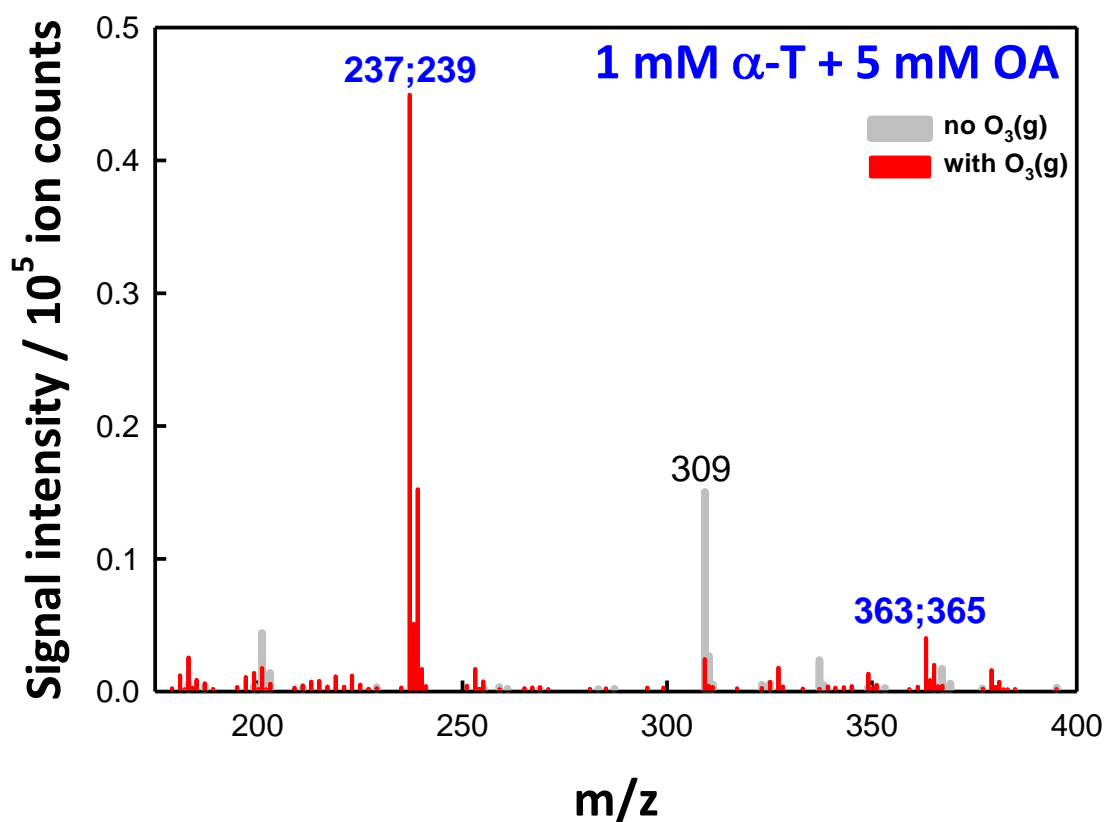
Fig.4-5-13 Negative ion mass spectra of 1 mM α-terpinene + 0.2 mM NaCl + 5 mM octanoic acid (OA) in W/AN (1:4 = vol:vol) solution microjets (gray), or those exposed to $O_3(g)$ (red, $E = 5.4 \times 10^{11}$ molecules cm^{-3} s) at 1 atm and 298 K. The signals at m/z 309 appearing without $O_3(g)$ exposure is assigned to $Na(OA)_2^-$. In the presence of $O_3(g)$, new mass signals at m/z 363/365 (from CIs + OA) in addition to those at m/z 237/239 (from CIs + H_2O) appear.
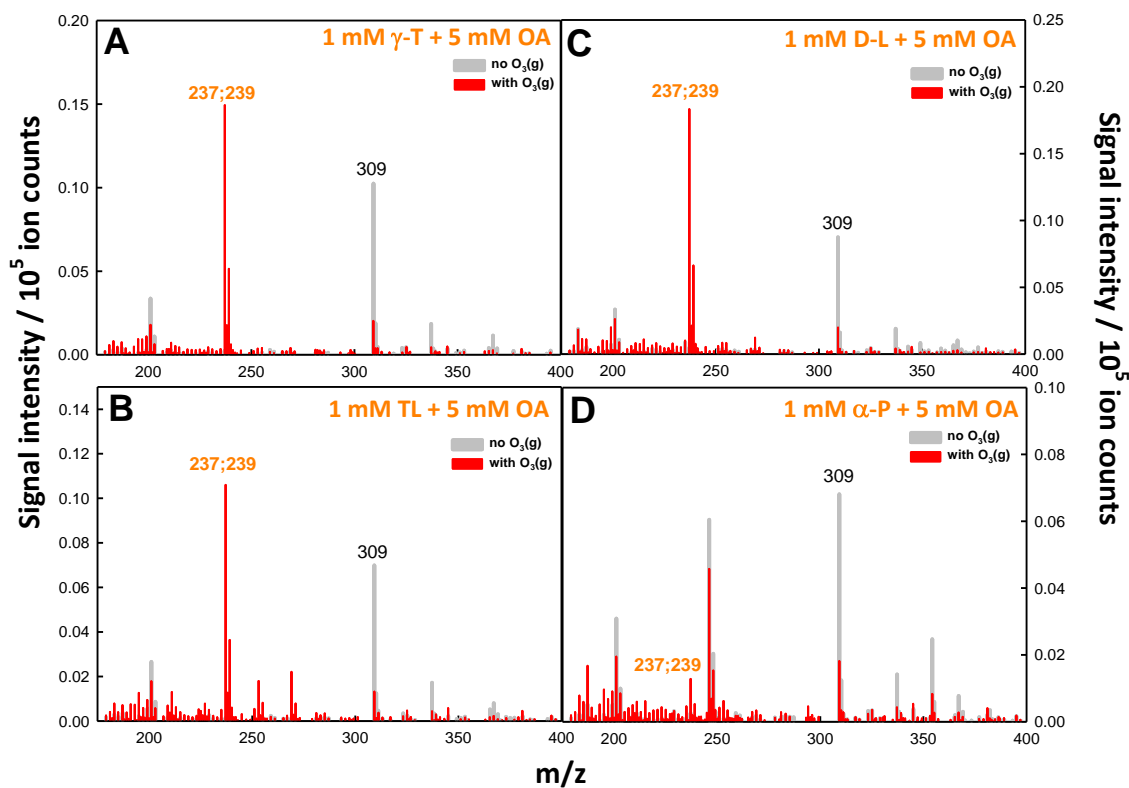
Fig.4-5-14 Negative ion mass spectra of 1 mM α-terpinene (A), terpinolene (B), D-limonene (C) or α-pinene (D) + 0.2 mM NaCl + 5 mM octanoic acid (OA) in W/AN (1:4 = vol:vol) solution microjets (gray), or those exposed to $O_3(g)$ (red, $E \approx 5.3 \times 10^{11}$ molecules cm^{-3} s) at 1 atm and 298 K. Note the absence of mass signals at m/z 363/365 (from CIs + OA) in the presence of $O_3(g)$.
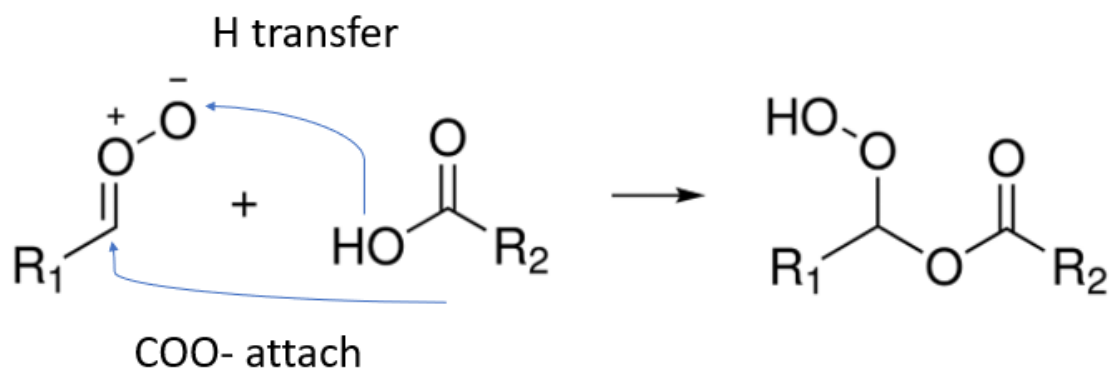
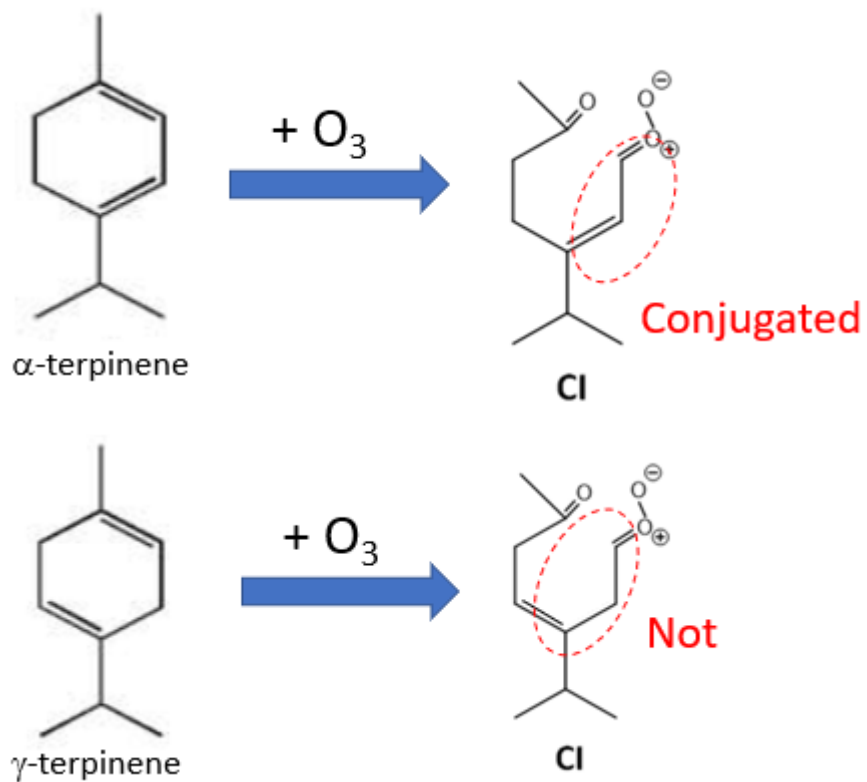Fig. 4-5-15 Schemetic of Criegee intermediate reacting with an organic acid.

Fig. 4-5-16 Reaction mechanism of ozonolysis of α-T and γ-T initiated CIs.

Chapter 5 Conclusion

5.1 Summary of this thesis

In Chapter 1, the background and significance of CI in the atmosphere are introduced, including its reactivity in both gas phase and multiphase, and the breakthrough in the direct observation of CI.

Some previous infrared spectroscopic studies of CI are reviewed in Chapter 2. By using a thermoelectrically cooled continuous wave mid-infrared distributed feedback QCL as the spectroscopic light, we established a new method for the detection of simplest CI, CH_2OO, and a high-resolved infrared spectrum was recorded from 1273.0 cm^{-1} to 1277.2 cm^{-1}, which is in good agreement with the earlier work done with a pulsed QCL.

The application of this new method in the reactivity researches of CH_2OO is described in Chapter 3, the rate coefficient for $CH_2OO + SO_2$ measured in this work was in good agreement with previous studies, which demonstrates the feasibility of this new method to investigate the reactivity of CH_2OO. As well, the rate coefficient for $CH_2OO + NO_2$ was measured to be $(4.4 \pm 0.2) \times 10^{-12}$ cm^3 molecule^{-1} s^{-1}. Two previous experimental studies[16], [19] have provided values of the same order for this rate coefficient, and an exactly same value was reported in another theoretical calculation research[58].

A pneumatic electrospray ionization technique combined with a quadrupole mass analyzer to explore the reactivity of CI on gas-liquid interfaces is introduced in Chapter 4. The sesquiterpenes (α-humulene, β-caryophyllene) and monoterpenes (α-terpene, γ-terpene, terpinolene, D-limonene, α-pinene) initiated CIs are generated on gas-liquid interfaces in the collision of O_3 onto sesquiterpenes or monoterpenes dissolved water-acetonitrile mixed droplets, and their reactivity towards some key chemicals in the atmosphere has been investigated. In contrast with gas phase, the reactivity of CI on gas-liquid interfaces is affected by some other factors. The surface characteristics depends on the components of liquid aerosols. The molecular structures of organic

compounds contained in the aerosols and the functional groups they possess determined their distributions and orientations in outermost layers.

5.2 Atmospheric implications

As discussed in Chapter 3, a modified value of the rate coefficient for CH_2OO reacting with NO_2 was obtained in this work by using a high-resolution mid-infrared spectroscopic method. The oxidation of NO_2 initiated by CI is supposed to be re-evaluated, especially in the boreal area, where sCIs can survive in a relatively low concentration of water vapor. Nevertheless, as mentioned before, the available CI species are relatively smaller ones, which indicates that furthermore researches on CI in gas phase should be focused on the synthesis of long chain CIs and their characterization, kinetics, reactivity, in order to predict the global burden of CI more precisely.

Given the condition that unsaturated organic compounds can be absorbed by airborne droplets and in situ react with O_3, the reactivity of CI on gas-liquid interfaces plays a vital role in determining the components of aerosols. The molecular structures of reactants determine their distributions and orientations on gas-liquid interfaces, finally lead to a completely different chemistry in contrast with gas phase, indicating the generation of distinct products via ozonolysis of alkenes on gas-liquid interfaces, which may evolve to form some toxic chemicals.

5.3 Outlooks

The significance of understanding Criegee chemistry is not limited in atmospheric chemistry. As a recently defined new kind of reactive oxygen species (ROS), CI may play a potentially important role in physiological chemistry. ROS are produced in a wide range of atmospheric and physiological processes. Endogenous ROS mainly come from mitochondria, the endoplasmic reticulum, peroxisomes, microsomes, and NO_X

complexes (seven distinct isoforms) in cell membranes.[103], [104] Free radicals formed in ambient environment are defined as exogenous ROS. Antioxidants such ascorbate inside biosystems are responsible for the neutralization of ROS, however, excessive production of ROS can overwhelm antioxidant defenses and give rise to oxidative stress, cell death, biological aging, chronic inflammation, allergies, and various diseases.[105], [106]

Typical ROS, such as O_3, OH radical, H_2O_2, are connected to Criegee chemistry closely. As introduced in Chapter 1, half of the CI generated upon ozonolysis of alkenes in the atmosphere, cannot be thermally stabilized, and decompose to release OH radical. Stabilized CIs, because of their strong oxidising ability, may trigger oxidative stress on proteins or DNA, like other ROS.[107], [108] Laboratory-generated SOA by α-pinene, β-pinene, contain a substantial amount of H_2O_2, which is likely formed by decomposition or hydrolysis of hydroxyhydroperoxides, peroxy acids, and related species for α- and β-pinene SOA.[109] High- molecular weight dimer esters (peroxides) are also found to be main products in boreal forest aerosols, which are formed upon ozonolysis of α-pinene.[110] The result in this work is consistent with ours, that the CIs generated on gas-liquid interfaces subsequently react with organic compounds (benzoic acid, octanoic acid, cis-pinonic acid), to form such kinds of peroxides, which prefer to decompose and release H_2O_2 under alkaline conditions[90]. Therefore, how the pH affect Criegee chemistry on gas-liquid interface should be another interesting issue. The peroxides generated in Criegee chemistry are water-soluble with additional hydrophilic functional groups. The investigation on the aging processes of these chemicals both in liquid phase and on gas-liquid can be important and challenging, which potentially contribute to an increase in toxicity in the atmosphere.[91], [111], [112]

References and notes

[1]   M. A. H. Khan, C. J. Percival, R. L. Caravan, C. A. Taatjes, and D. E. Shallcross, "Criegee intermediates and their impacts on the troposphere," *Environ. Sci. Process. Impacts*, vol. 20, no. 3, pp. 437–453, 2018.

[2]   R. Criegee and G. Wenner, "Die Ozonisierung des 9,10-Oktalins," *Justus Liebigs Ann. Chem.*, vol. 564, no. 1, pp. 9–15, Jul. 1949.

[3]   R. Criegee, "Mechanism of Ozonolysis," *Angew. Chemie Int. Ed. English*, vol. 14, no. 11, pp. 745–752, Nov. 1975.

[4]   R. L. Mauldin *et al.*, "A new atmospherically relevant oxidant of sulphur dioxide," *Nature*, vol. 488, no. 7410, pp. 193–196, 2012.

[5]   J. H. Kroll, S. R. Sahay, J. G. Anderson, K. L. Demerjian, and N. M. Donahue, "Mechanism of HOx Formation in the Gas-Phase Ozone-Alkene Reaction. 2. Prompt versus Thermal Dissociation of Carbonyl Oxides to Form OH," *J. Phys. Chem. A*, vol. 105, no. 18, pp. 4446–4457, May 2001.

[6]   A. Lee *et al.*, "Gas-phase products and secondary aerosol yields from the ozonolysis of ten different terpenes," *J. Geophys. Res.*, vol. 111, no. D7, p. D07302, 2006.

[7]   M. Karl *et al.*, "Kinetic Study of the OH-isoprene and O_3 -isoprene reaction in the atmosphere simulation chamber, SAPHIR," *Geophys. Res. Lett.*, vol. 31, no. 5, p. n/a-n/a, Mar. 2004.

[8]   V. G. Khamaganov and R. A. Hites, "Rate Constants for the Gas-Phase Reactions of Ozone with Isoprene, α- and β-Pinene, and Limonene as a Function of Temperature," *J. Phys. Chem. A*, vol. 105, no. 5, pp. 815–822, Feb. 2001.

[9]   S. E. Wheeler, D. H. Ess, and K. N. Houk, "Thinking Out of the Black Box: Accurate Barrier Heights of 1,3-Dipolar Cycloadditions of Ozone with Acetylene and Ethylene," *J. Phys. Chem. A*, vol. 112, no. 8, pp. 1798–1807, Feb. 2008.

[10]   Y. Te Su, H. Y. Lin, R. Putikam, H. Matsui, M. C. Lin, and Y. P. Lee, "Extremely rapid self-reaction of the simplest Criegee intermediate CH_2OO and its implications in atmospheric chemistry," *Nat. Chem.*, vol. 6, no. 6, pp. 477–483, 2014.

[11]   W.-L. Ting, C.-H. Chang, Y.-F. Lee, H. Matsui, Y.-P. Lee, and J. J.-M. Lin, "Detailed mechanism of the $CH_2I + O_2$ reaction: Yield and self-reaction of the simplest Criegee intermediate CH_2OO," *J. Chem. Phys.*, vol. 141, no. 10, p. 104308, Sep. 2014.

[12] C. A. Taatjes *et al.*, "Direct Observation of the Gas-Phase Criegee Intermediate (CH$_2$OO)," *J. Am. Chem. Soc.*, vol. 130, no. 36, pp. 11883–11885, Sep. 2008.

[13] R. Asatryan and J. W. Bozzelli, "Formation of a Criegee intermediate in the low-temperature oxidation of dimethyl sulfoxide," *Phys. Chem. Chem. Phys.*, vol. 10, no. 13, p. 1769, 2008.

[14] M. T. Nguyen, T. L. Nguyen, V. T. Ngan, and H. M. T. Nguyen, "Heats of formation of the Criegee formaldehyde oxide and dioxirane," *Chem. Phys. Lett.*, vol. 448, no. 4–6, pp. 183–188, Nov. 2007.

[15] A. J. Eskola, D. Wojcik-Pastuszka, E. Ratajczak, and R. S. Timonen, "Kinetics of the reactions of CH$_2$Br and CH$_2$I radicals with molecular oxygen at atmospheric temperatures," *Phys. Chem. Chem. Phys.*, vol. 8, no. 12, p. 1416, 2006.

[16] O. Welz *et al.*, "Direct Kinetic Measurements of Criegee Intermediate (CH$_2$OO) Formed by Reaction of CH$_2$I with O$_2$," *Science (80-.).*, vol. 335, no. 6065, pp. 204–207, Jan. 2012.

[17] L. Sheps, "Absolute Ultraviolet Absorption Spectrum of a Criegee Intermediate CH$_2$OO," *J. Phys. Chem. Lett.*, vol. 4, no. 24, pp. 4201–4205, Dec. 2013.

[18] R. Chhantyal-Pun, A. Davey, D. E. Shallcross, C. J. Percival, and A. J. Orr-Ewing, "A kinetic study of the CH$_2$OO Criegee intermediate self-reaction, reaction with SO$_2$ and unimolecular reaction using cavity ring-down spectroscopy," *Phys. Chem. Chem. Phys.*, vol. 17, no. 5, pp. 3617–3626, 2015.

[19] D. Stone, M. Blitz, L. Daubney, N. U. M. Howes, and P. Seakins, "Kinetics of CH$_2$OO reactions with SO$_2$, NO$_2$, NO, H$_2$O and CH$_3$CHO as a function of pressure," *Phys. Chem. Chem. Phys.*, vol. 16, no. 3, pp. 1139–1149, 2014.

[20] H.-L. Huang, W. Chao, and J. J.-M. Lin, "Kinetics of a Criegee intermediate that would survive high humidity and may oxidize atmospheric SO$_2$," *Proc. Natl. Acad. Sci.*, vol. 112, no. 35, pp. 10857–10862, Sep. 2015.

[21] R. Crehuet, J. M. Anglada, and J. M. Bofill, "Tropospheric Formation of Hydroxymethyl Hydroperoxide, Formic Acid, H$_2$O$_2$, and OH from Carbonyl Oxide in the Presence of Water Vapor: A Theoretical Study of the Reaction Mechanism," *Chemistry (Easton).*, vol. 7, no. 10, pp. 2227–2235, May 2001.

[22] A. B. Ryzhkov and P. A. Ariya, "A theoretical study of the reactions of parent and substituted Criegee intermediates with water and the water dimer," *Phys. Chem. Chem. Phys.*, vol. 6, no. 21, p. 5042, 2004.

[23] W. Chao, J.-T. Hsieh, C.-H. Chang, and J. J.-M. Lin, "Direct kinetic measurement of the reaction of the simplest Criegee intermediate with water vapor," *Science (80-.).*, vol. 347, no. 6223, pp. 751–754, Feb. 2015.

96

[24] T. R. Lewis, M. A. Blitz, D. E. Heard, and P. W. Seakins, "Direct evidence for a substantive reaction between the Criegee intermediate, CH₂OO, and the water vapour dimer," *Phys. Chem. Chem. Phys.*, vol. 17, no. 7, pp. 4859–4863, 2015.

[25] C. A. Taatjes *et al.*, "Direct Measurements of Conformer-Dependent Reactivity of the Criegee Intermediate CH₃CHOO," *Science (80-.).*, vol. 340, no. 6129, pp. 177–180, Apr. 2013.

[26] L. Sheps, A. M. Scully, and K. Au, "UV absorption probing of the conformer-dependent reactivity of a Criegee intermediate CH₃CHOO," *Phys. Chem. Chem. Phys.*, vol. 16, no. 48, pp. 26701–26706, 2014.

[27] L.-C. Lin, W. Chao, C.-H. Chang, K. Takahashi, and J. J.-M. Lin, "Temperature dependence of the reaction of anti-CH₃CHOO with water vapor," *Phys. Chem. Chem. Phys.*, vol. 18, no. 40, pp. 28189–28197, 2016.

[28] J. M. Anglada, P. Aplincourt, J. M. Bofill, and D. Cremer, "Atmospheric Formation of OH Radicals and H₂O₂ from Alkene Ozonolysis under Humid Conditions," *ChemPhysChem*, vol. 3, no. 2, pp. 215–221, Feb. 2002.

[29] J. M. Anglada, J. González, and M. Torrent-Sucarrat, "Effects of the substituents on the reactivity of carbonyl oxides. A theoretical study on the reaction of substituted carbonyl oxides with water," *Phys. Chem. Chem. Phys.*, vol. 13, no. 28, p. 13034, 2011.

[30] B. Long, J. L. Bao, and D. G. Truhlar, "Atmospheric Chemistry of Criegee Intermediates: Unimolecular Reactions and Reactions with Water," *J. Am. Chem. Soc.*, vol. 138, no. 43, pp. 14409–14422, Nov. 2016.

[31] L.-C. Lin *et al.*, "Competition between H₂O and (H₂O)₂ reactions with CH₂OO/CH₃CHOO," *Phys. Chem. Chem. Phys.*, vol. 18, no. 6, pp. 4557–4568, 2016.

[32] M. J. Newland, A. R. Rickard, L. Vereecken, A. Muñoz, M. Ródenas, and W. J. Bloss, "Atmospheric isoprene ozonolysis: impacts of stabilised Criegee intermediate reactions with SO₂, H₂O and dimethyl sulfide," *Atmos. Chem. Phys.*, vol. 15, no. 16, pp. 9521–9536, Aug. 2015.

[33] J. D. Fenske, A. S. Hasson, A. W. Ho, and S. E. Paulson, "Measurement of Absolute Unimolecular and Bimolecular Rate Constants for CH₃CHOO Generated by the trans -2-Butene Reaction with Ozone in the Gas Phase," *J. Phys. Chem. A*, vol. 104, no. 44, pp. 9921–9932, Nov. 2000.

[34] O. Horie, C. Schfer, and G. K. Moortgat, "High reactivity of hexafluoro acetone toward criegee intermediates in the gas-phase ozonolysis of simple alkenes," *Int. J. Chem. Kinet.*, vol. 31, no. 4, pp. 261–269, 1999.

[35]   C. A. Taatjes *et al.*, "Direct measurement of Criegee intermediate (CH_2OO) reactions with acetone, acetaldehyde, and hexafluoroacetone," *Phys. Chem. Chem. Phys.*, vol. 14, no. 30, p. 10391, 2012.

[36]   Y. Liu, K. D. Bayes, and S. P. Sander, "Measuring Rate Constants for Reactions of the Simplest Criegee Intermediate (CH_2OO) by Monitoring the OH Radical," *J. Phys. Chem. A*, vol. 118, no. 4, pp. 741–747, Jan. 2014.

[37]   O. Welz *et al.*, "Rate Coefficients of C1 and C2 Criegee Intermediate Reactions with Formic and Acetic Acid Near the Collision Limit: Direct Kinetics Measurements and Atmospheric Implications," *Angew. Chemie Int. Ed.*, vol. 53, no. 18, pp. 4547–4550, Apr. 2014.

[38]   J. Zhong, M. Kumar, C. Q. Zhu, J. S. Francisco, and X. C. Zeng, "Surprising Stability of Larger Criegee Intermediates on Aqueous Interfaces," *Angew. Chemie Int. Ed.*, vol. 56, no. 27, pp. 7740–7744, Jun. 2017.

[39]   J. Zhong, C. Zhu, L. Li, G. L. Richmond, J. S. Francisco, and X. C. Zeng, "Interaction of SO_2 with the Surface of a Water Nanodroplet," *J. Am. Chem. Soc.*, vol. 139, no. 47, pp. 17168–17174, Nov. 2017.

[40]   J. Zhong, Y. Zhao, L. Li, H. Li, J. S. Francisco, and X. C. Zeng, "Interaction of the NH_2 Radical with the Surface of a Water Droplet," *J. Am. Chem. Soc.*, vol. 137, no. 37, pp. 12070–12078, Sep. 2015.

[41]   N. Heine, F. A. Houle, and K. R. Wilson, "Connecting the Elementary Reaction Pathways of Criegee Intermediates to the Chemical Erosion of Squalene Interfaces during Ozonolysis," *Environ. Sci. Technol.*, vol. 51, no. 23, pp. 13740–13748, 2017.

[42]   N. Heine, C. Arata, A. H. Goldstein, F. A. Houle, and K. R. Wilson, "Multiphase Mechanism for the Production of Sulfuric Acid from SO_2 by Criegee Intermediates Formed during the Heterogeneous Reaction of Ozone with Squalene," *J. Phys. Chem. Lett.*, vol. 9, no. 12, pp. 3504–3510, 2018.

[43]   S. Enami and A. J. Colussi, "Criegee Chemistry on Aqueous Organic Surfaces," *J. Phys. Chem. Lett.*, vol. 8, no. 7, pp. 1615–1623, Apr. 2017.

[44]   Y.-T. Su, Y.-H. Huang, H. A. Witek, and Y.-P. Lee, "Infrared Absorption Spectrum of the Simplest Criegee Intermediate CH_2OO," *Science (80-.).*, vol. 340, no. 6129, pp. 174–176, Apr. 2013.

[45]   Y.-H. Huang, J. Li, H. Guo, and Y.-P. Lee, "Infrared spectrum of the simplest Criegee intermediate CH_2OO at resolution 0.25 cm^{-1} and new assignments of bands $2\nu9$ and $\nu5$," *J. Chem. Phys.*, vol. 142, no. 21, p. 214301, Jun. 2015.

[46]   Y.-P. Chang, A. J. Merer, H.-H. Chang, L.-J. Jhang, W. Chao, and J. J.-M. Lin,

"High resolution quantum cascade laser spectroscopy of the simplest Criegee intermediate, CH$_2$OO, between 1273 cm^{-1} and 1290 cm^{-1}," *J. Chem. Phys.*, vol. 146, no. 24, p. 244302, Jun. 2017.

[47] S. Miyano and K. Tonokura, "Measurements of nitrogen-broadening coefficients in the ν$_3$ band of the hydroperoxyl radical using a continuous wave quantum cascade laser," *J. Mol. Spectrosc.*, vol. 265, no. 1, pp. 47–51, Jan. 2011.

[48] University of Bristol, "PGOPHER, a program for rotational, vibrational and electronic spectra, version 9.1.100," 2016. .

[49] M. Nakajima and Y. Endo, "Communication: Determination of the molecular structure of the simplest Criegee intermediate CH$_2$OO," *J. Chem. Phys.*, vol. 139, no. 10, p. 101103, Sep. 2013.

[50] M. C. McCarthy *et al.*, "The Simplest Criegee Intermediate (H$_2$C═O–O): Isotopic Spectroscopy, Equilibrium Structure, and Possible Formation from Atmospheric Lightning," *J. Phys. Chem. Lett.*, vol. 4, no. 23, pp. 4133–4139, Dec. 2013.

[51] A. M. Daly, B. J. Drouin, and S. Yu, "Submillimeter measurements of the Criegee intermediate CH$_2$OO, in the gas phase," *J. Mol. Spectrosc.*, vol. 297, pp. 16–20, Mar. 2014.

[52] J. K. G. Watson, "Aspects of quartic and sextic centrifugal effects on rotational energy levels," in *Vibrational spectra and structure, vol.6. A series of advances*, 1977.

[53] J. Qiu and K. Tonokura, "Detection of the simplest Criegee intermediate CH$_2$OO in the ν4 band using a continuous wave quantum cascade laser and its kinetics with SO$_2$ and NO$_2$," *Chem. Phys. Lett. X*, vol. 2, p. 100019, Apr. 2019.

[54] B. Ouyang, M. W. McLeod, R. L. Jones, and W. J. Bloss, "NO$_3$ radical production from the reaction between the Criegee intermediate CH$_2$OO and NO$_2$," *Phys. Chem. Chem. Phys.*, vol. 15, no. 40, p. 17070, 2013.

[55] J. C. Mössinger, D. E. Shallcross, and R. A. Cox, "UV-VIS absorption cross-sections and atmospheric lifetimes of CH$_2$Br$_2$, CH$_2$I$_2$ and CH$_2$BrI," *J. Chem. Soc. - Faraday Trans.*, 1998.

[56] H. Xu, Y. Guo, S. Liu, X. Ma, D. Dai, and G. Sha, "Photodissociation dynamics of CH$_2$I$_2$ molecules in the ultraviolet range studied by ion imaging," *J. Chem. Phys.*, 2002.

[57] R. J. Kee, F. M. Rupley, and J. A. Miller, "Chemkin-II: A Fortran Chemical Kinetics Package for the Analysis of Gas-Phase Chemical Kinetics," 1995.

[58] L. Vereecken and H. M. T. Nguyen, "Theoretical Study of the Reaction of

Carbonyl Oxide with Nitrogen Dioxide: $CH_2OO + NO_2$," *Int. J. Chem. Kinet.*, vol. 49, no. 10, pp. 752–760, Oct. 2017.

[59] K. A. Perrine *et al.*, "Characterization of the Acetonitrile Aqueous Solution/Vapor Interface by Liquid-Jet X-ray Photoelectron Spectroscopy," *J. Phys. Chem. C*, vol. 118, no. 50, pp. 29378–29388, Dec. 2014.

[60] M. J. Makowski, A. C. Stern, J. C. Hemminger, and D. J. Tobias, "Orientation and Structure of Acetonitrile in Water at the Liquid–Vapor Interface: A Molecular Dynamics Simulation Study," *J. Phys. Chem. C*, vol. 120, no. 31, pp. 17555–17563, Aug. 2016.

[61] Y. Rao, N. J. Turro, and K. B. Eisenthal, "Water Structure at Air/Acetonitrile Aqueous Solution Interfaces," *J. Phys. Chem. C*, vol. 113, no. 32, pp. 14384–14389, Aug. 2009.

[62] S. Paul and A. Chandra, "Liquid-vapor interfaces of water-acetonitrile mixtures of varying composition," *J. Chem. Phys.*, vol. 123, no. 18, p. 184706, Nov. 2005.

[63] S. Enami and A. J. Colussi, "Reactions of Criegee Intermediates with Alcohols at Air–Aqueous Interfaces," *J. Phys. Chem. A*, vol. 121, no. 27, pp. 5175–5182, Jul. 2017.

[64] S. Enami, M. R. Hoffmann, and A. J. Colussi, "Criegee Intermediates React with Levoglucosan on Water," *J. Phys. Chem. Lett.*, vol. 8, no. 16, pp. 3888–3894, Aug. 2017.

[65] S. Enami and A. J. Colussi, "Efficient scavenging of Criegee intermediates on water by surface-active: Cis -pinonic acid," *Phys. Chem. Chem. Phys.*, vol. 19, no. 26, pp. 17044–17051, 2017.

[66] J. Qiu, S. Ishizuka, K. Tonokura, and S. Enami, "Reactions of Criegee Intermediates with Benzoic Acid at the Gas/Liquid Interface," *J. Phys. Chem. A*, vol. 122, no. 30, pp. 6303–6310, Aug. 2018.

[67] J. Qiu, S. Ishizuka, K. Tonokura, A. J. Colussi, and S. Enami, "Reactivity of Monoterpene Criegee Intermediates at Gas–Liquid Interfaces," *J. Phys. Chem. A*, vol. 122, no. 39, pp. 7910–7917, Oct. 2018.

[68] X. Li, T. Hede, Y. Tu, C. Leck, and H. Ågren, "Surface-Active cis -Pinonic Acid in Atmospheric Droplets: A Molecular Dynamics Study," *J. Phys. Chem. Lett.*, vol. 1, no. 4, pp. 769–773, Feb. 2010.

[69] S. D. R. Wilson and A. Hulme, "The Effect of Bubbles Attached to an Electrode on Electrical Resistance and Dissolved Gas Concentration," *Proc. R. Soc. A Math. Phys. Eng. Sci.*, vol. 387, no. 1792, pp. 133–146, May 1983.

[70] Lord Rayleigh, "XX. On the equilibrium of liquid conducting masses charged

with electricity," *London, Edinburgh, Dublin Philos. Mag. J. Sci.*, vol. 14, no. 87, pp. 184–186, Sep. 1882.

[71] M. Dole, L. L. Mack, R. L. Hines, R. C. Mobley, L. D. Ferguson, and M. B. Alice, "Molecular Beams of Macroions," *J. Chem. Phys.*, vol. 49, no. 5, pp. 2240–2249, Sep. 1968.

[72] G. Schmelzeisen-Redeker, L. Bütfering, and F. W. Röllgen, "Desolvation of ions and molecules in thermospray mass spectrometry," *Int. J. Mass Spectrom. Ion Process.*, vol. 90, no. 2, pp. 139–150, Jun. 1989.

[73] P. Kebarle and L. Tang, "From ions in solution to ions in the gas phase - the mechanism of electrospray mass spectrometry," *Anal. Chem.*, vol. 65, no. 22, pp. 972A-986A, Nov. 1993.

[74] B. A. Thomson and J. V. Iribarne, "Field induced ion evaporation from liquid surfaces at atmospheric pressure," *J. Chem. Phys.*, vol. 71, no. 11, pp. 4451–4463, Dec. 1979.

[75] J. V. Iribarne, "On the evaporation of small ions from charged droplets," *J. Chem. Phys.*, vol. 64, no. 6, p. 2287, 1976.

[76] K. F. Ho *et al.*, "Dicarboxylic acids, ketocarboxylic acids, α-dicarbonyls, fatty acids and benzoic acid in PM&lt;sub&gt;2.5&lt;/sub&gt; aerosol collected during CAREBeijing-2007: an effect of traffic restriction on air quality," *Atmos. Chem. Phys.*, vol. 15, no. 6, pp. 3111–3123, Mar. 2015.

[77] I. Suh, R. Zhang, L. T. Molina, and M. J. Molina, "Oxidation Mechanism of Aromatic Peroxy and Bicyclic Radicals from OH−Toluene Reactions," *J. Am. Chem. Soc.*, vol. 125, no. 41, pp. 12655–12665, Oct. 2003.

[78] R. TUCKERMANN, "Surface tension of aqueous solutions of water-soluble organic and inorganic compounds," *Atmos. Environ.*, vol. 41, no. 29, pp. 6265–6275, Sep. 2007.

[79] J. Hoigné and H. Bader, "Rate constants of reactions of ozone with organic and inorganic compounds in water—II," *Water Res.*, vol. 17, no. 2, pp. 185–194, Jan. 1983.

[80] S. Enami, M. R. Hoffmann, and A. J. Colussi, "Extensive H-atom abstraction from benzoate by OH-radicals at the air–water interface," *Phys. Chem. Chem. Phys.*, vol. 18, no. 46, pp. 31505–31512, 2016.

[81] B. Minofar, P. Jungwirth, M. R. Das, W. Kunz, and S. Mahiuddin, "Propensity of formate, acetate, benzoate, and phenolate for the aqueous solution/vapor interface: Surface tension measurements and molecular dynamics simulations," *J. Phys. Chem. C*, vol. 111, no. 23, pp. 8242–8247, 2007.

[82] S. Enami, T. Fujii, Y. Sakamoto, T. Hama, and Y. Kajii, "Carboxylate Ion Availability at the Air–Water Interface," *J. Phys. Chem. A*, vol. 120, no. 46, pp. 9224–9234, Nov. 2016.

[83] R.-J. Huang *et al.*, "High secondary aerosol contribution to particulate pollution during haze events in China," *Nature*, vol. 514, no. 7521, pp. 218–222, Oct. 2014.

[84] Z. Chowdhury *et al.*, "Speciation of ambient fine organic carbon particles and source apportionment of PM 2.5 in Indian cities," *J. Geophys. Res.*, vol. 112, no. D15, p. D15303, Aug. 2007.

[85] J. Jr-Min Lin and W. Chao, "Structure-dependent reactivity of Criegee intermediates studied with spectroscopic methods," *Chem. Soc. Rev.*, vol. 46, no. 24, pp. 7483–7497, 2017.

[86] Y. Sakamoto, R. Yajima, S. Inomata, and J. Hirokawa, "Water vapour effects on secondary organic aerosol formation in isoprene ozonolysis," *Phys. Chem. Chem. Phys.*, vol. 19, no. 4, pp. 3165–3175, 2017.

[87] H. Tong *et al.*, "Hydroxyl radicals from secondary organic aerosol decomposition in water," *Atmos. Chem. Phys.*, vol. 16, no. 3, pp. 1761–1771, Feb. 2016.

[88] E. Vidrio, C. H. Phuah, A. M. Dillner, and C. Anastasio, "Generation of Hydroxyl Radicals from Ambient Fine Particles in a Surrogate Lung Fluid Solution," *Environ. Sci. Technol.*, vol. 43, no. 3, pp. 922–927, Feb. 2009.

[89] R. Zhao, C. M. Kenseth, Y. Huang, N. F. Dalleska, and J. H. Seinfeld, "Iodometry-Assisted Liquid Chromatography Electrospray Ionization Mass Spectrometry for Analysis of Organic Peroxides: An Application to Atmospheric Secondary Organic Aerosol," *Environ. Sci. Technol.*, vol. 52, no. 4, pp. 2108–2117, 2018.

[90] R. Zhao *et al.*, "Rapid Aqueous-Phase Hydrolysis of Ester Hydroperoxides Arising from Criegee Intermediates and Organic Acids," *J. Phys. Chem. A*, vol. 122, no. 23, pp. 5190–5201, 2018.

[91] M. Shiraiwa *et al.*, "Aerosol Health Effects from Molecular to Global Scales," *Environ. Sci. Technol.*, vol. 51, no. 23, pp. 13545–13567, Dec. 2017.

[92] S. Enami, M. R. Hoffmann, and A. J. Colussi, "OH-Radical Specific Addition to Glutathione S-Atom at the Air-Water Interface: Relevance to the Redox Balance of the Lung Epithelial Lining Fluid," *J. Phys. Chem. Lett.*, vol. 6, no. 19, pp. 3935–3943, 2015.

[93] G. Caldwell, R. Renneboog, and P. Kebarle, "Gas phase acidities of aliphatic carboxylic acids, based on measurements of proton transfer equilibria," *Can. J.*

Chem., 2006.

[94] Y.-J. Feng *et al.*, "π-Hydrogen Bonding of Aromatics on the Surface of Aerosols: Insights from Ab Initio and Molecular Dynamics Simulation," *J. Phys. Chem. B*, vol. 120, no. 27, pp. 6667–6673, Jul. 2016.

[95] P. Xiao, J.-J. Yang, W.-H. Fang, and G. Cui, "QM/MM studies on ozonolysis of α-humulene and Criegee reactions with acids and water at air–water/acetonitrile interfaces," *Phys. Chem. Chem. Phys.*, vol. 20, no. 23, pp. 16138–16150, 2018.

[96] M.-T. Lee, F. Orlando, L. Artiglia, S. Chen, and M. Ammann, "Chemical Composition and Properties of the Liquid–Vapor Interface of Aqueous C1 to C4 Monofunctional Acid and Alcohol Solutions," *J. Phys. Chem. A*, vol. 120, no. 49, pp. 9749–9758, Dec. 2016.

[97] R. L. Redington, "Kinetics of oxygen-18 exchange between carboxylic acids and water," *J. Phys. Chem.*, vol. 80, no. 3, pp. 229–235, Jan. 1976.

[98] Y. Ma, T. R. Willcox, A. T. Russell, and G. Marston, "Pinic and pinonic acid formation in the reaction of ozone with α-pinene," *Chem. Commun.*, 2007.

[99] L. Vereecken, A. Novelli, and D. Taraborrelli, "Unimolecular decay strongly limits the atmospheric impact of Criegee intermediates," *Phys. Chem. Chem. Phys.*, vol. 19, no. 47, pp. 31599–31612, 2017.

[100] S. Enami, M. R. Hoffmann, and A. J. Colussi, "Ozonolysis of Uric Acid at the Air/Water Interface," *J. Phys. Chem. B*, vol. 112, no. 14, pp. 4153–4156, Apr. 2008.

[101] M. I. Lester and S. J. Klippenstein, "Unimolecular Decay of Criegee Intermediates to OH Radical Products: Prompt and Thermal Decay Processes," *Acc. Chem. Res.*, vol. 51, no. 4, pp. 978–985, Apr. 2018.

[102] N. M. Kidwell, H. Li, X. Wang, J. M. Bowman, and M. I. Lester, "Unimolecular dissociation dynamics of vibrationally activated CH3CHOO Criegee intermediates to OH radical products," *Nat. Chem.*, vol. 8, no. 5, pp. 509–514, May 2016.

[103] D. Trachootham, J. Alexandre, and P. Huang, "Targeting cancer cells by ROS-mediated mechanisms: a radical therapeutic approach?," *Nat. Rev. Drug Discov.*, vol. 8, no. 7, pp. 579–591, Jul. 2009.

[104] J. R. Hoidal, "Reactive Oxygen Species and Cell Signaling," *Am. J. Respir. Cell Mol. Biol.*, vol. 25, no. 6, pp. 661–663, Dec. 2001.

[105] T. Finkel and N. J. Holbrook, "Oxidants, oxidative stress and the biology of ageing," *Nature*, vol. 408, no. 6809, pp. 239–247, Nov. 2000.

[106] C. C. Winterbourn, "Reconciling the chemistry and biology of reactive oxygen

species," *Nat. Chem. Biol.*, vol. 4, no. 5, pp. 278–286, May 2008.

[107] Q. Li, J. Shang, and T. Zhu, "Physicochemical characteristics and toxic effects of ozone-oxidized black carbon particles," *Atmos. Environ.*, vol. 81, pp. 68–75, Dec. 2013.

[108] J. Vieceli, O. L. Ma, and D. J. Tobias, "Uptake and Collision Dynamics of Gas Phase Ozone at Unsaturated Organic Interfaces," *J. Phys. Chem. A*, vol. 108, no. 27, pp. 5806–5814, Jul. 2004.

[109] Y. Wang, H. Kim, and S. E. Paulson, "Hydrogen peroxide generation from α- and β-pinene and toluene secondary organic aerosols," *Atmos. Environ.*, vol. 45, no. 18, pp. 3149–3156, Jun. 2011.

[110] K. Kristensen *et al.*, "High-Molecular Weight Dimer Esters Are Major Products in Aerosols from α-Pinene Ozonolysis and the Boreal Forest," *Environ. Sci. Technol. Lett.*, vol. 3, no. 8, pp. 280–285, 2016.

[111] H. Li, Z. Chen, L. Huang, and D. Huang, "Organic peroxides' gas-particle partitioning and rapid heterogeneous decomposition on secondary organic aerosol," *Atmos. Chem. Phys.*, vol. 16, no. 3, pp. 1837–1848, 2016.

[112] S. Wang *et al.*, "Relationship between chemical composition and oxidative potential of secondary organic aerosol from polycyclic aromatic hydrocarbons," *Atmos. Chem. Phys.*, vol. 18, no. 6, pp. 3987–4003, 2018.

[113] T. L. Nguyen, H. Lee, D. A. Matthews, M. C. McCarthy, and J. F. Stanton, "Stabilization of the simplest Criegee intermediate from the reaction between ozone and ethylene: A high-level quantum chemical and kinetic analysis of ozonolysis," *J. Phys. Chem. A*, vol. 119, no. 22, pp. 5524–5533, 2015.

[114] H.-Y. Lin *et al.*, "Infrared identification of the Criegee intermediates syn- and anti-CH3CHOO, and their distinct conformation-dependent reactivity," *Nat. Commun.*, vol. 6, no. 1, p. 7012, Nov. 2015.

[115] S. Banerjee and S. Mazumdar, "Electrospray Ionization Mass Spectrometry: A Technique to Access the Information beyond the Molecular Weight of the Analyte," *Int. J. Anal. Chem.*, vol. 2012, pp. 1–40, 2012.

[116] T. G. Theofanous, V. V. Mitkin, C. L. Ng, C.-H. Chang, X. Deng, and S. Sushchikh, "The physics of aerobreakup. II. Viscous liquids," *Phys. Fluids*, vol. 24, no. 2, p. 022104, Feb. 2012.

[117] O. A. Mamer, "Medical Applications of Mass Spectrometry," in *Encyclopedia of Spectroscopy and Spectrometry*, Elsevier, 2017, pp. 772–780.

[118] H. Mishra *et al.*, "Bronsted basicity of the air-water interface," *Proc. Natl. Acad. Sci.*, vol. 109, no. 46, pp. 18679–18683, Nov. 2012.
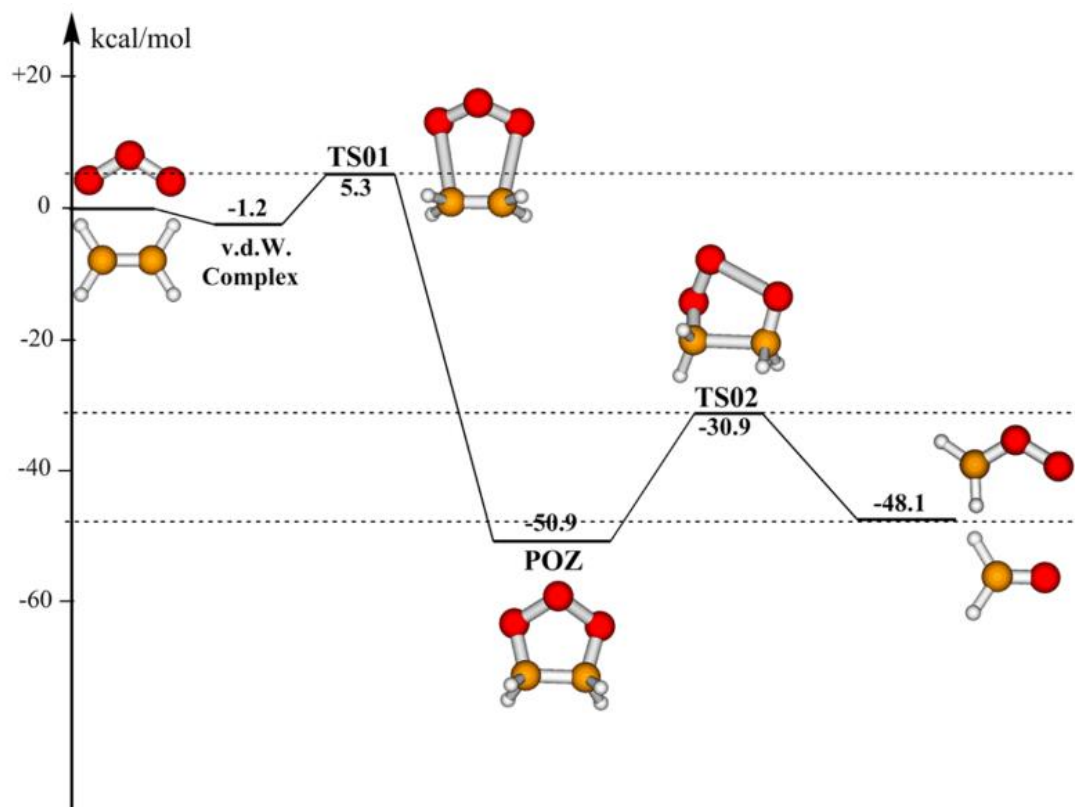
Appendix

Fig.A1-1 Schematic reaction energy diagram of the formation of CH_2OO from the O_3 + C_2H_4 reaction adopted from the work of Nguyen et al.[113], and values of each energy state are reported by Wheeler et al.[9]
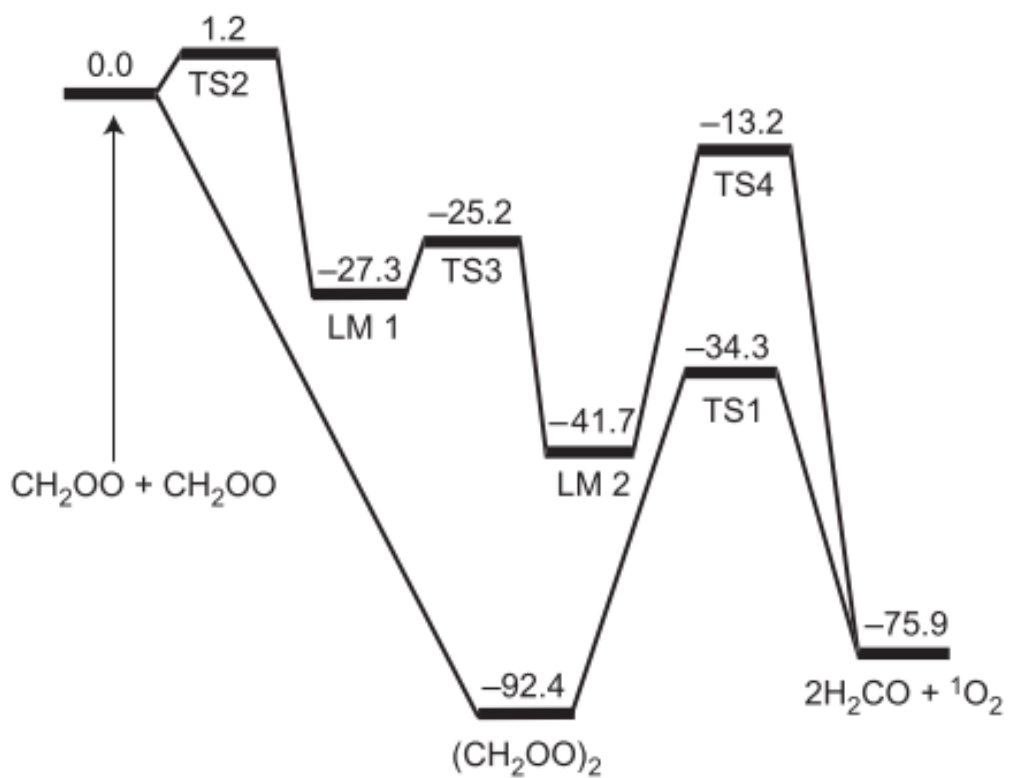
Fig.A1-2 Schematic energy diagram for the $CH_2OO + CH_2OO$ reaction paths calculated at the CCSD(T)//B3LYP/aug-cc-pVTZ-pp level. Energy is given by kcal mol^{-1}.[10]
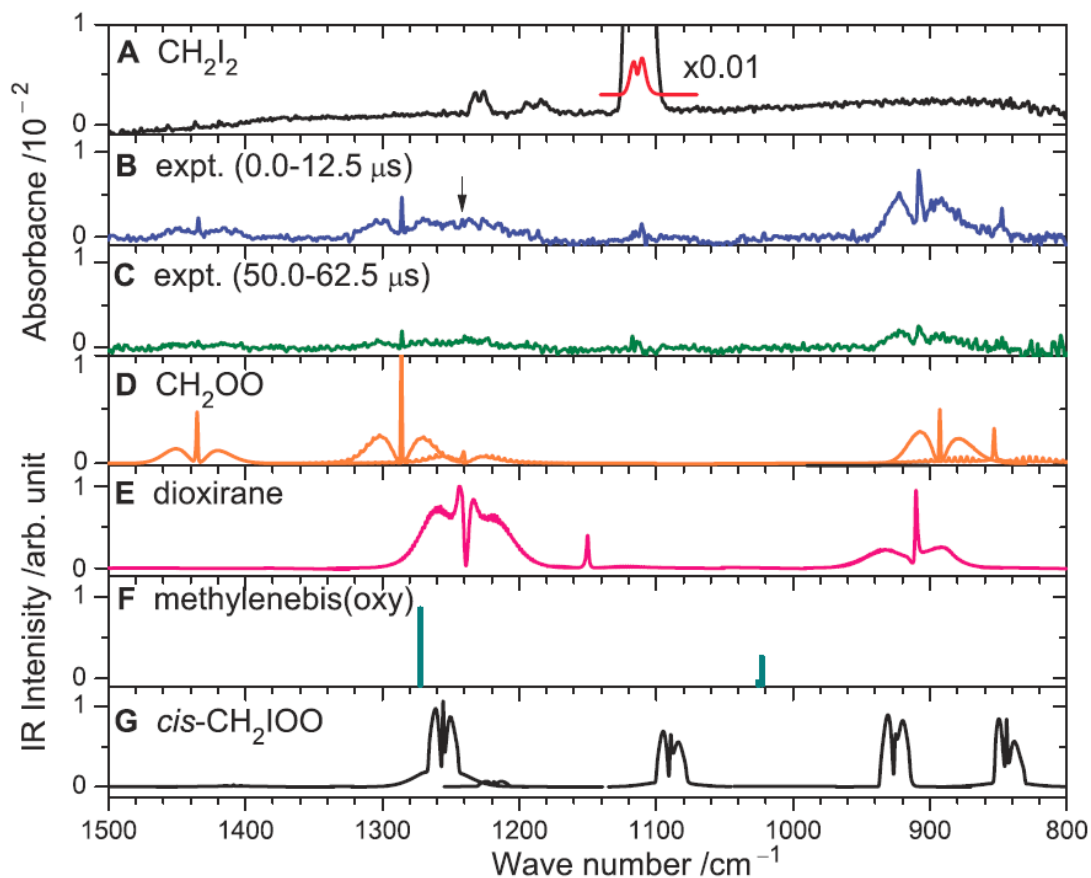
Fig.A2-1 Infrared absorption spectra recorded by Su et al. in the CH_2I_2/O_2 photolysis system. (A) CH_2I_2 precursor, (B) and (C) experimental absorption spectra in different timings, (D–F) simulated spectra of CH_2O_2 isomers based on electronic structure calculations, (G) simulated spectrum of CH_2IOO.[44]
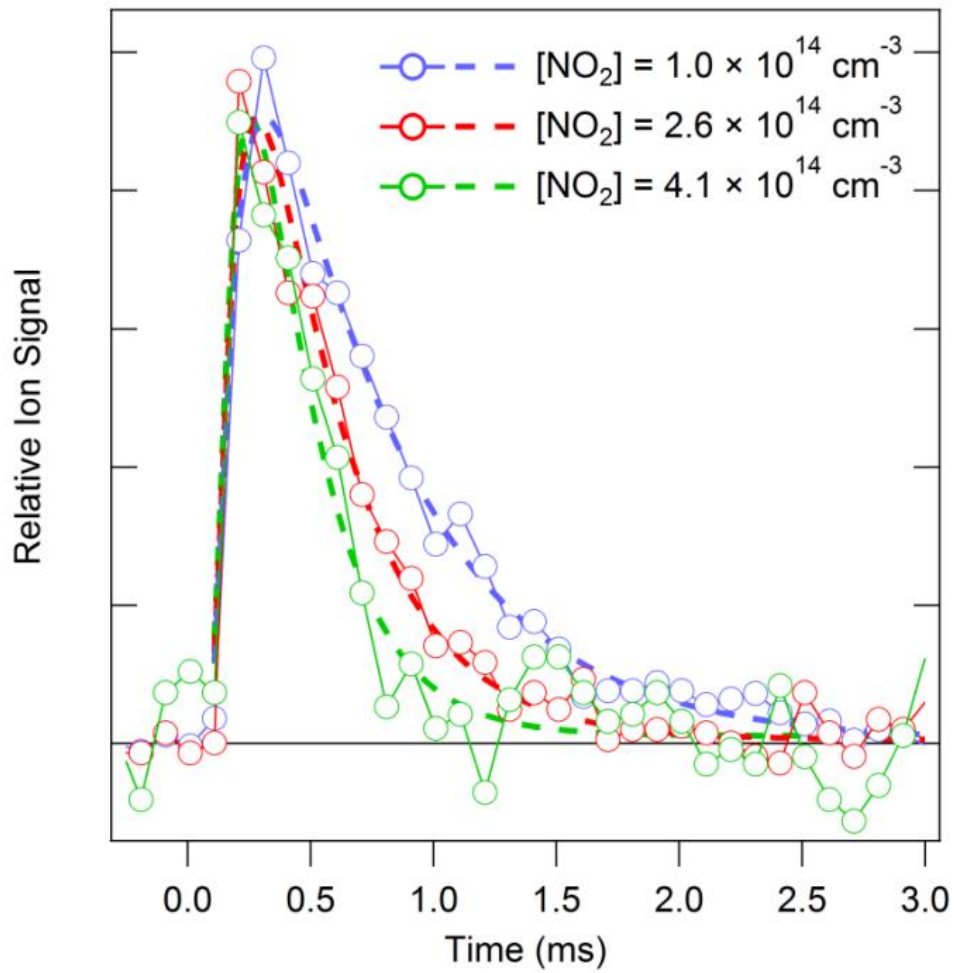
Fig.A3-1 Time profiles of CH_2OO signals reported in the work carried out by Welz et al. Dashed lines represent fits to the data traces, including convolution with a measured instrument response function.[16]
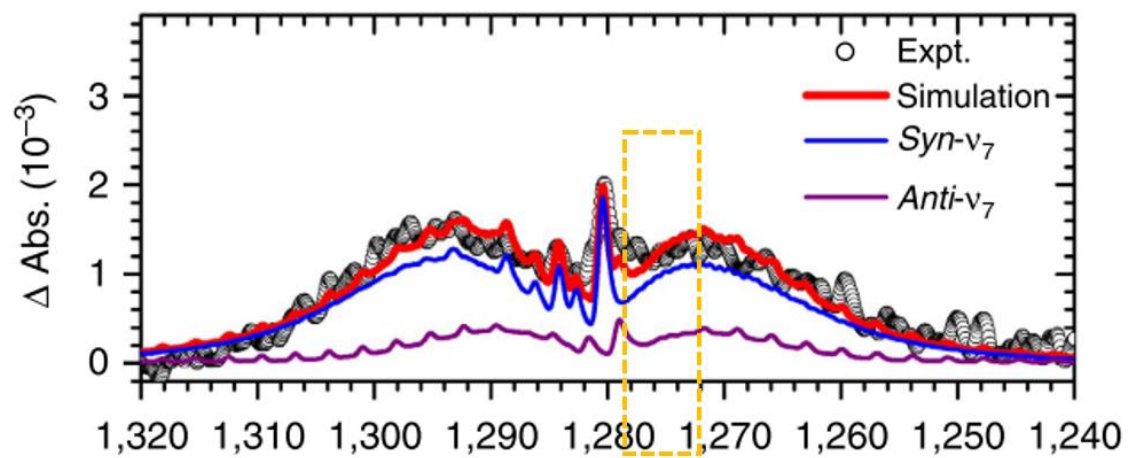
Fig.A3-2 An absorption band of CH_3CHOO with a band origin near 1280 cm-1 reported in the work of Huang et al.[114]. The region enclosed by the yellow dashed line is where our QCL covers.
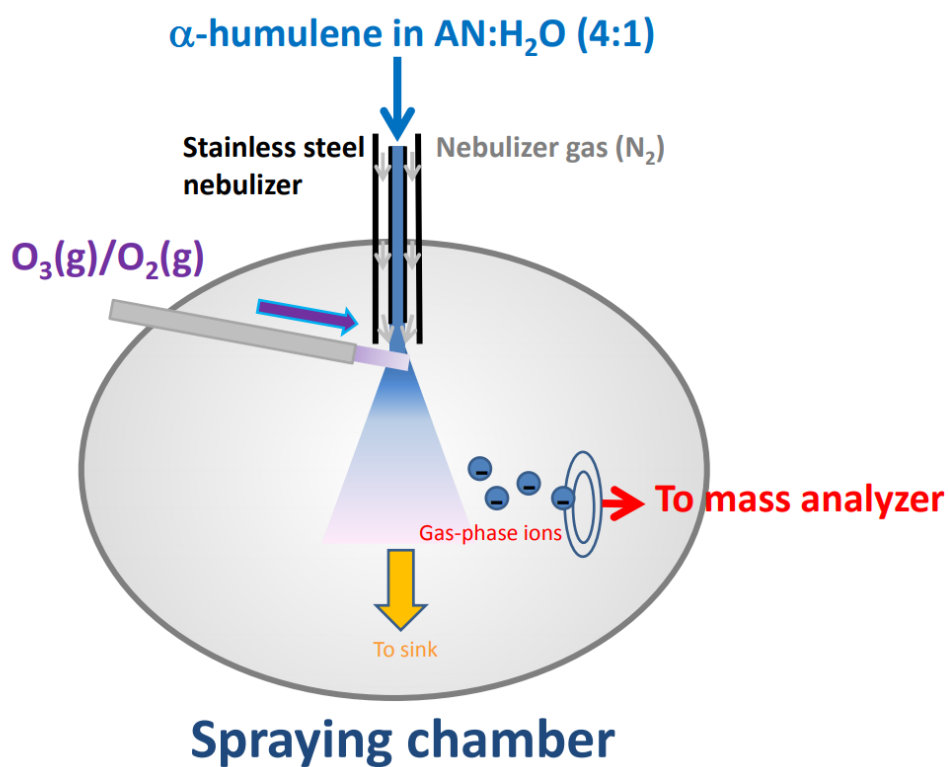
Fig.A4-1 Experimental setup of researches of Criegee intermediates on gas-liquid interfaces.[43]
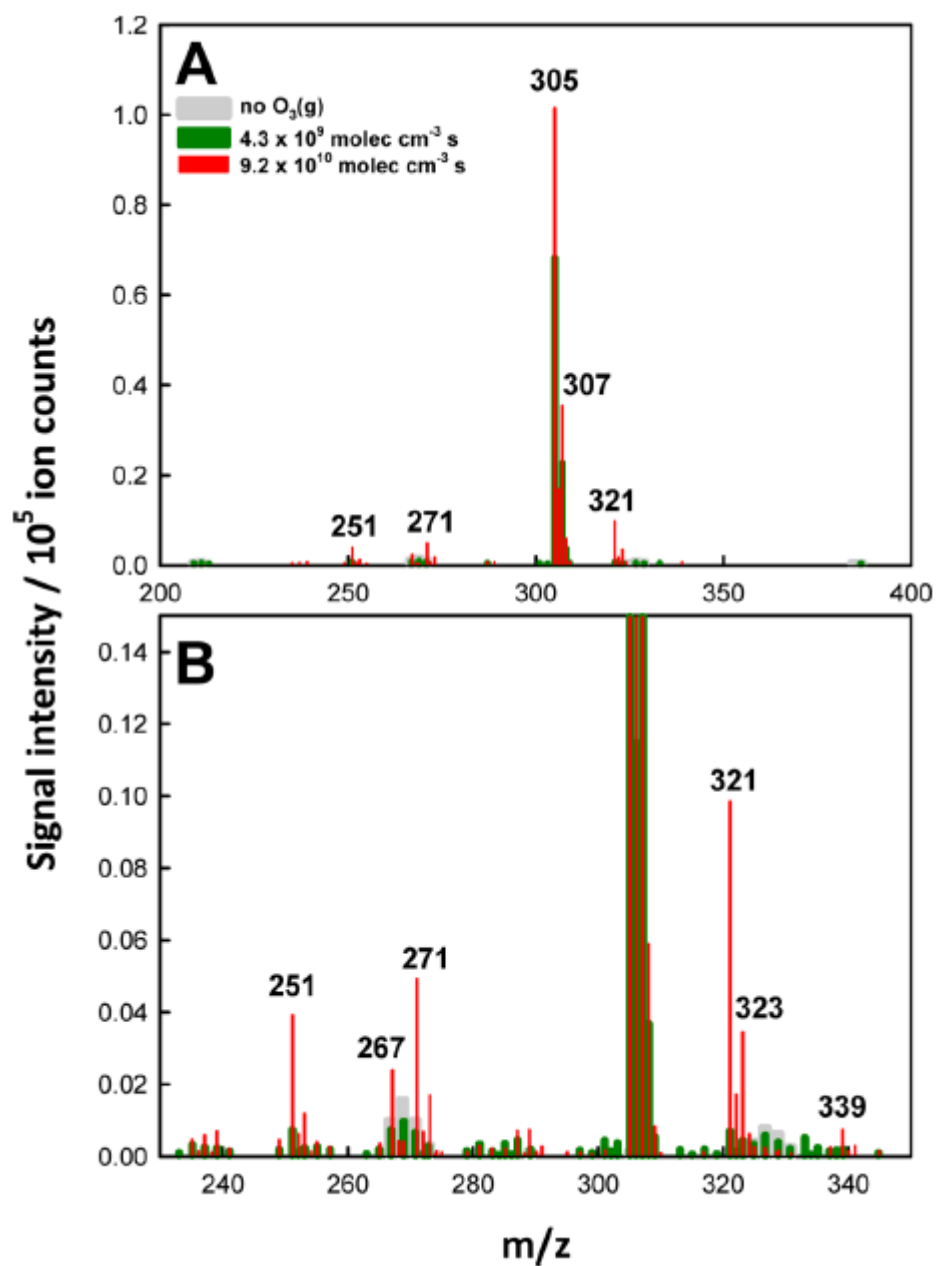
Fig.A4-2 (A) Negative ion mass spectra from 1 mM α-H + 0.2 mM NaCl in W/AN (1:4 = vol:vol) solution microjets in addition of different concentrations of O_3. (B) Zooming in on the ozonation products.[43]
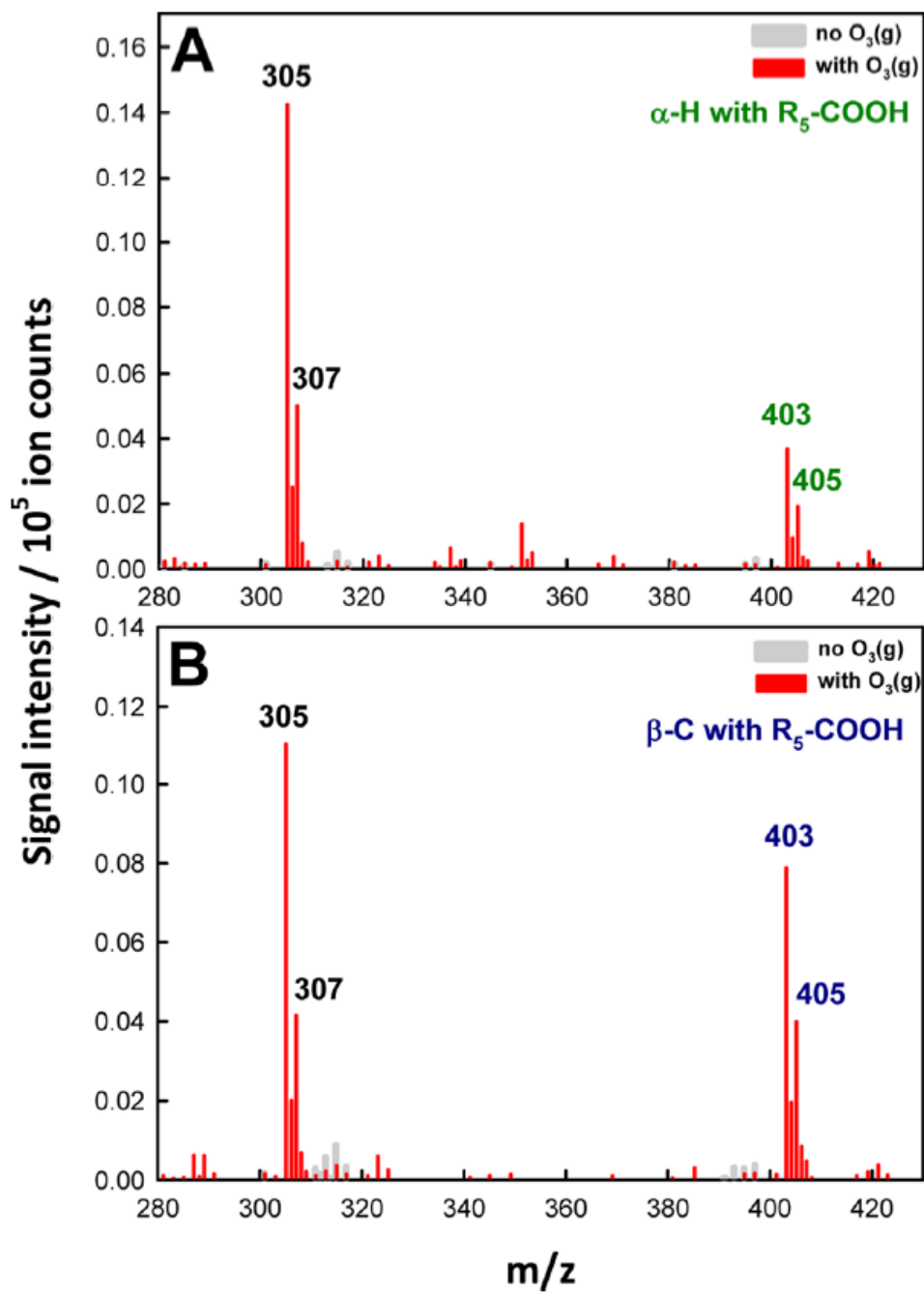
Fig.A4-3 Negative ion mass spectra from 1 mM (A) α-H or (B) β-C + 0.2 mM NaCl + 100 mM hexanoic acid in W/AN (1:4 = vol:vol) solution microjets in the absence (gray) and presence of $O_3(g)$.[43]
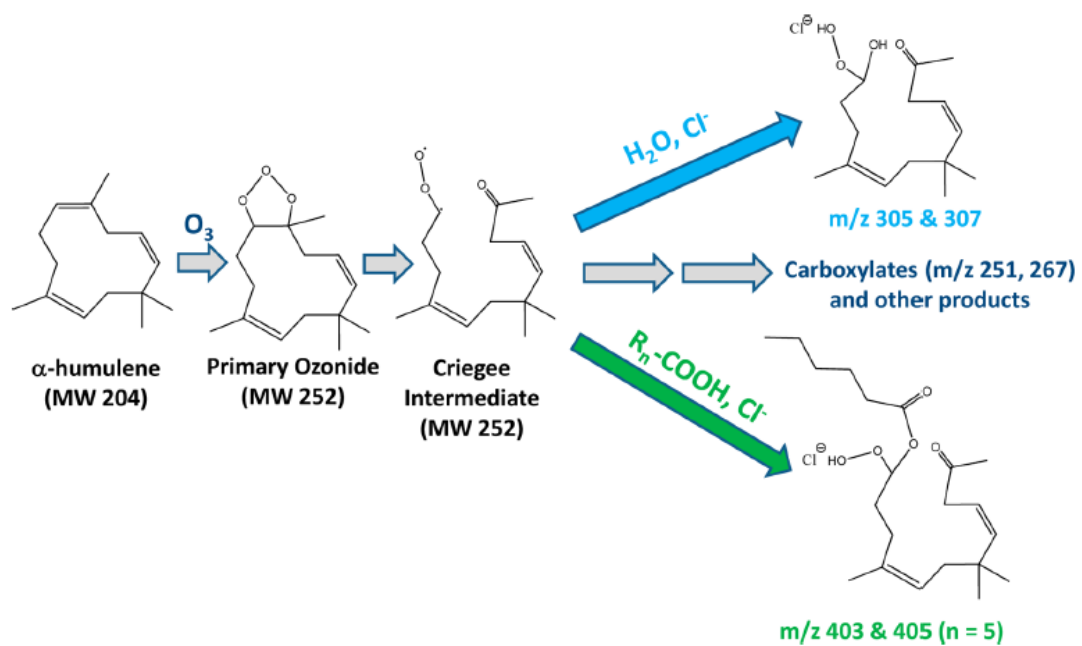
Fig.A4-4 Mechanism of ozonolysis of α-humulene and subsequent reactions at the gas-liquid interface.[43]
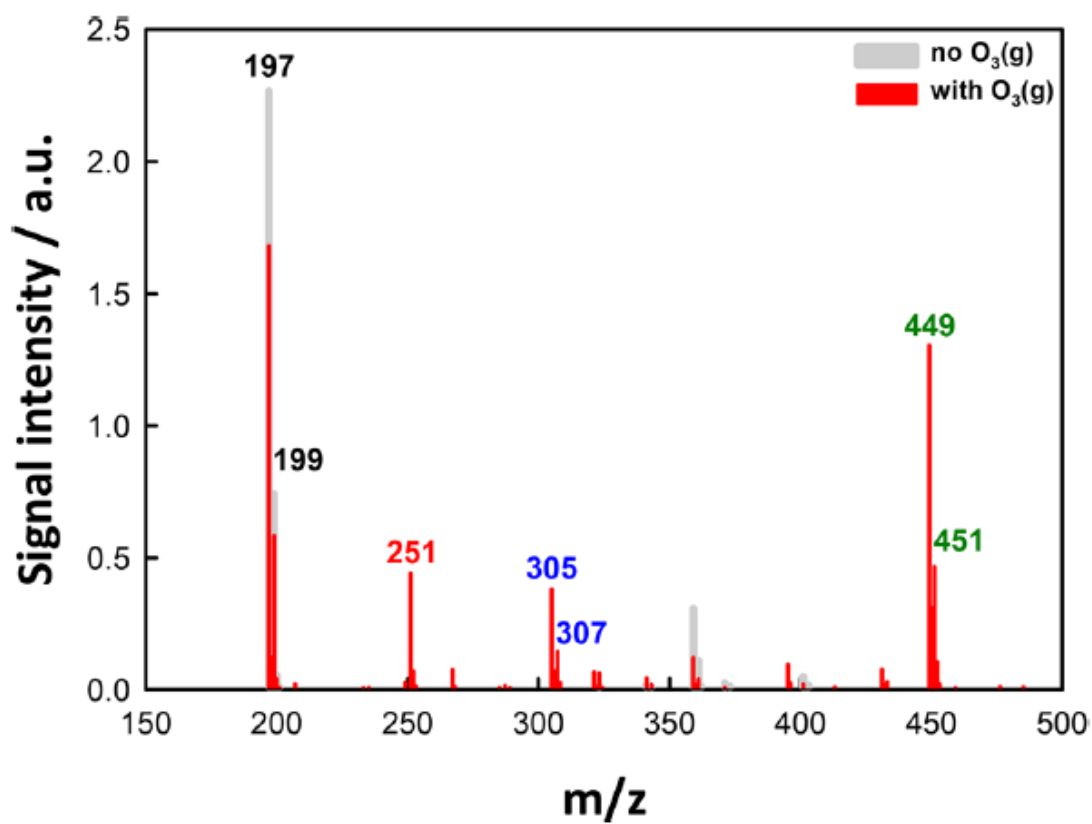
Fig.A4-5 Negative ion electrospray mass spectra of 1 mM β-C + 0.2 mM NaCl + 100 mM levoglucosan in W/AN (1:4 = vol:vol) solution microjets in the absence (gray) and presence of $O_3(g)$ (red) at 1 atm and 298 K.[64]
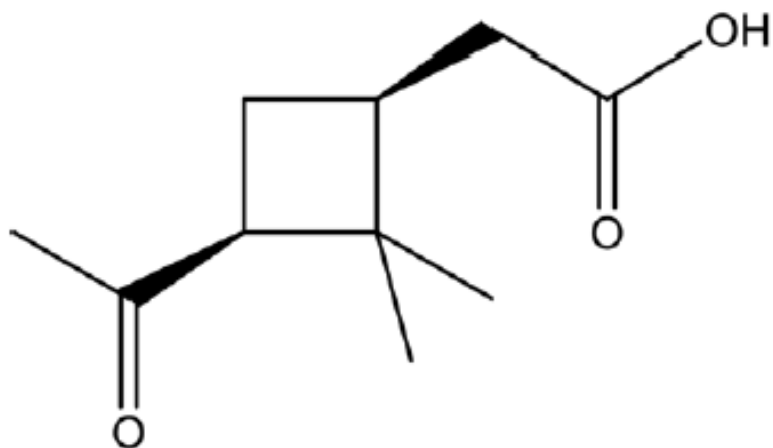
Fig.A4-6 Molecular structure of cis-pinonic acid. (CPA)
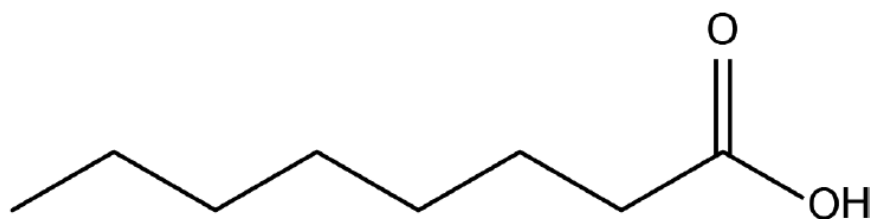
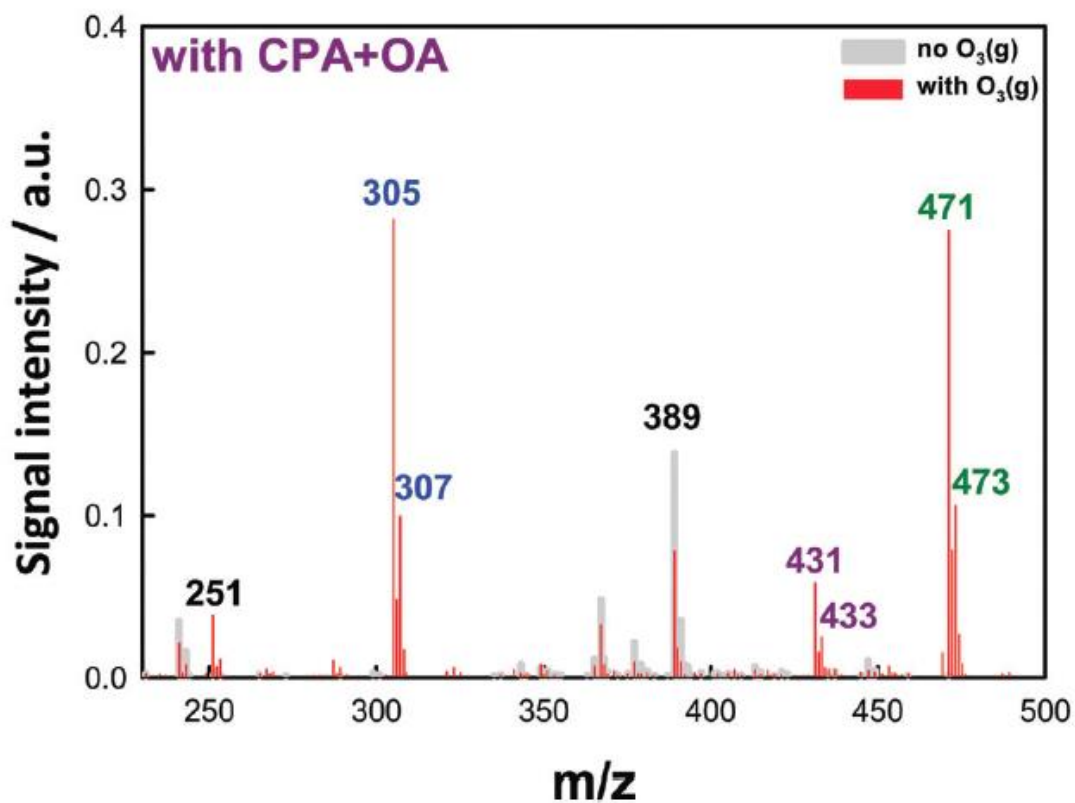Fig.A4-7 Molecular structure of octanoic acid. (OA)

Fig.A4-8 Negative ion electrospray mass spectra of 1 mM β-caryophyllene + 0.2 mM NaCl + 10 mM cis-pinonic acid + 10 mM octanoic acid in W/AN (1 :4 = vol : vol) solution microjets in the absence (gray) and presence of $O_3(g)$ (red) at 1 atm and 298 K. [65]
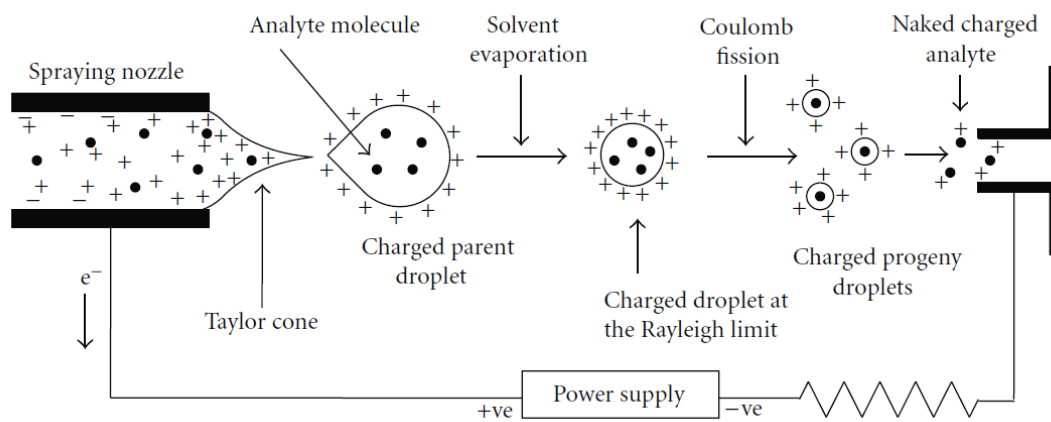
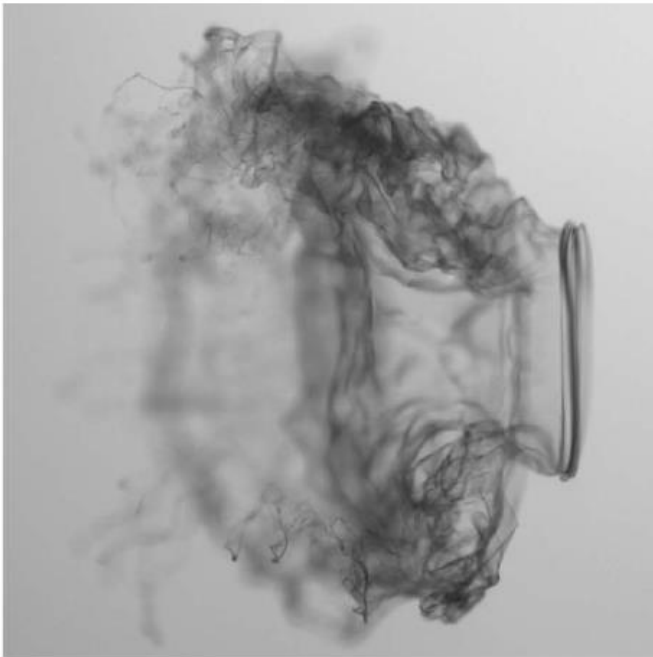Fig.A4-9 Schematic representation of the electrospray ionization process.[115]

Fig.A4-10 Snapshots of aerobreakup of a droplet presented by T. G. Theofanous et al.[116]
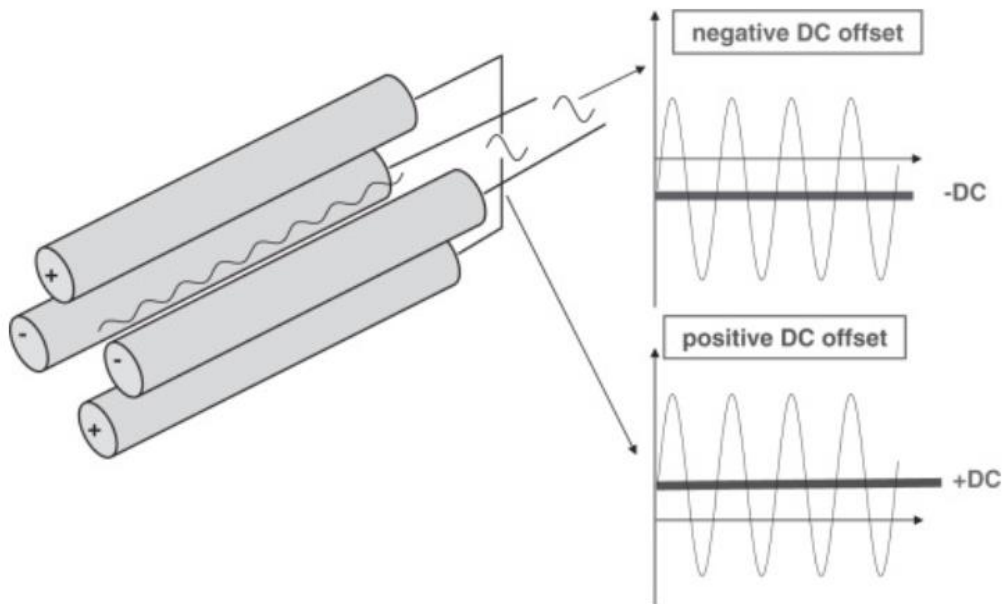
Fig.A4-11 Schematic representation of a quadrupole mass analyzer and a voltage profile on the rods. At a particular AC and DC voltages, only the ion with a given m/z passes through the quadrupole field.[117]
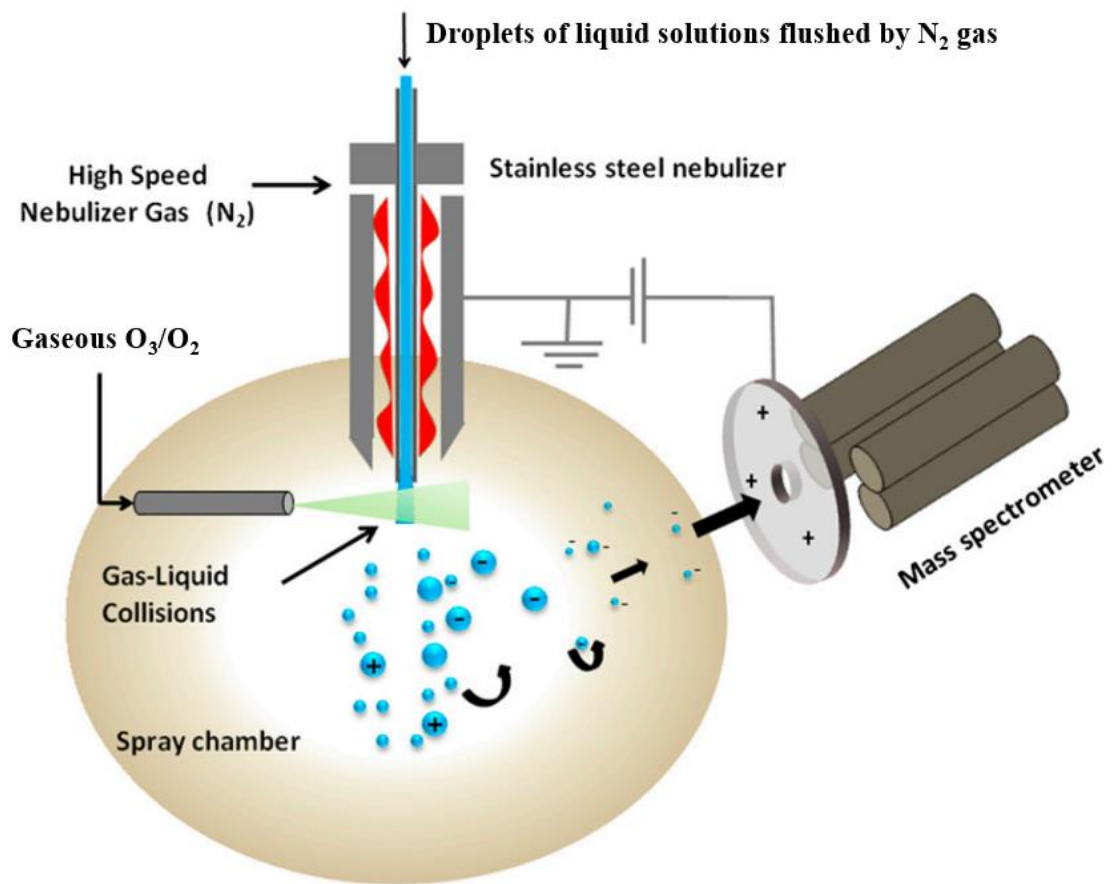
Fig.A4-12 Schematic representation of a costumed ESI mass spectrometer developed by
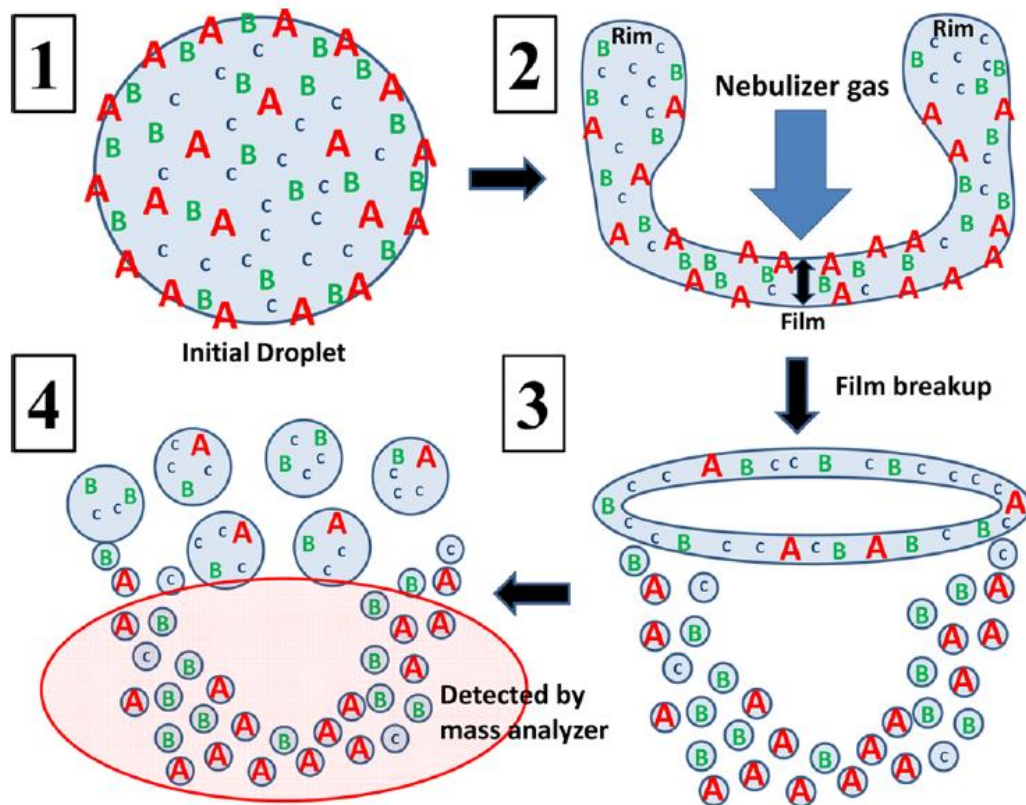Enami et al.[118]

Fig.A4-13 Schematic illustration of a droplet breakup mechanism.[82]

Table A2-1 Device temperature and electronic current selected for the calibration.

Device temperature (°C) for QCL	Values of electronic current (mA) where absorption lines of N_2O appeared	Corresponding wavenumber (cm^{-1})	Fitted function (x for electronic current, y for wavenumber, R^2 > 0.999)
30	446.8	1277.235	$y = 1279.12700 - 9.69867 \times 10^{-4}x - 7.31743 \times 10^{-6}x^2$
	502.8	1276.785	
	551.6	1276.365	
	602.3	1275.895	
	641.0	1275.495	
40	475.6	1275.895	$y = 1277.85387 - 1.69784 \times 10^{-4}x - 8.30972 \times 10^{-6}x^2$
	522.2	1275.495	
	576.4	1275.000	
	613.5	1274.620	
50	491.0	1274.620	$y = 1276.23728 + 0.00184x - 1.04508 \times 10^{-5}x^2$
	548.4	1274.100	
	584.7	1273.74	
	635.8	1273.18	

謝辞

　修士、博士の生活を振り替えてみると、勉強や研究に限らず、様々な面で戸野倉先生に大変お世話になっておりました。先生は知識やテクニックを教えて下さっただけではなく、一人の研究者、一人の人間としての正しい価値観や責任感も強く叩き込んで来ました。ここに深く御礼申し上げます。

　副査の大島先生、布浦先生、秋月先生、中野先生には、博士論文を執筆するうえで有益なご助言をいただきました。ここに深く感謝を申し上げます。

　この一年間、国立環境研究所に通えて、江波先生のご指導の元で実験をさせていただきました。様々な面で大変勉強になったと思いますが、中でも一番印象に残ったのは江波先生が見せてくれた研究に対する熱情です。また、同じ実験室の石塚さんにも助言や相談をしていただきました。ここに二人に厚く御礼申し上げます。

　研究室生活において、留学生である自分は秘書の小山さんやこの研究室に所属している/いた学生の皆様に常に面倒をおかけいたしました。事故が起きた時、皆さんに丁寧にフォローして頂き、大変助かりました。ここに感謝の気持ちを込めてお礼申し上げます。

　修士課程に入ったばかりの何もわからない自分は、南田先輩に実験装置の組み立てや実験手法などについて、丁寧に教えていただきました。誠に感謝申し上げます。

　自然科学はこの世界で起きっている客観的な物理、化学現象を人間の言葉に訳す仕事です。また、文学や芸術と異なって、自然科学の素晴らしさは言葉や文化の違いに関係なく、すべての人に伝わることができます。学問というのは、まさに人と人との繋がりや絆で出来ているものです。人と人との競い合い、助け合いの中で、新たな閃きや思想は生み出されるでしょう。

　35度を超える気温の中で、秋が深けたようないささか寂しい気持ちがします。博士論文を作成している間、特に最近の一か月、現実と夢の境が曖昧になったような生活を送って来ました。

　家族からの支えがいなければ、ここまでの出来事を成し遂げるはずがないです。悲しみに飲まれた母親は一切の弱みも表に出したことなく、一人で淡々と彼女にとって一番理不尽な現実に抗って闘って来ました。母親が見せてくれた勇気はこの一生で忘れることはないでしょう。そして、母親に頂いた感動、感激及び勇気はこれからの人生のかけがえのない宝物になります。